Measurements and Observability Analysis for Biological and Aerospace Applications

Burak Boyacioglu

A dissertation
submitted in partial fulfillment of the
requirements for the degree of

Doctor of Philosophy

University of Washington

2022

Reading Committee:
Kristi Morgansen, Chair
Mehran Mesbahi
Ed Habtour

Program Authorized to Offer Degree:
Aeronautics and Astronautics

University of Washington

Abstract

Measurements and Observability Analysis for Biological and Aerospace Applications

Burak Boyacioglu

Chair of the Supervisory Committee:
Kristi Morgansen
Department of Aeronautics and Astronautics

Improving the observability properties of a system allows us to better estimate the system's states, hence design efficient robust controllers. However, every system is unique with its dynamics and measurement functions, and the existing numerical/analytical observability analysis tools may fail to complete the task because of the sometimes unusual forms of these functions. In this dissertation, we mainly study two questions from an observability point of view: optimal sensor placement on a flapping wing with neural-inspired measurements, and optimal trajectory planning for the estimation of inertial parameters of a rigid body such as spacecraft, airliner, or satellite. The former requires the development of observability analysis tools for systems with output delay and for systems with composite output functions. We pose observability-based optimization problems to achieve the latter task. After studying these problems using deterministic tools, we consider the process noise in the observability analysis, which can reveal observability in systems that would be otherwise regarded as unobservable and use a numerical tool, the stochastic empirical Gramian, to address the problem of sensor placement for systems in the presence of noise.

TABLE OF CONTENTS

LIST OF TABLES

LIST OF FIGURES

Figure Number Page

ACKNOWLEDGMENTS

Our true mentor in life is science.

If one day, my words are against science, choose science.

M. Kemal Atatürk

This dissertation would not possibly be completed without a long list of mentors, collaborators, and friends. First, I would like to thank my advisor, Prof. Morgansen. Throughout the years she has advised me, she has been consistently professional and guiding while being supportive and open to new research ideas.

I would also like to thank my supervisory committee members, Professors Mesbahi, Brunton, Burden and Habtour, for donating their time and giving me valuable feedback.

During my doctoral journey, I have collaborated with scientists and engineers in GNC as well as colleagues in various areas, such as neurobiologists, oceanographers, mathematicians, and material scientists. I would like to extend my thanks to them all, especially to Danylo Sandursky for being an excellent (first) research mentee, to Mahnoush Babaei and Amanuel H. Mamo and their supervisors Professors Bergbreiter and Daniel for working on their FEA model according to the needs of my research, and to Alice C. Schwarze and her supervisor Prof. Bing Brunton for using their combinatorics skills to help me to reach one of the main results in Sec. 4.2. The proof given in Appendix B is solely Alice's contribution to my research.

I have had many lab and office mates: (NCDL) Trevor, Natalie, Kimber, Ena, Sierra, John, Veevee, Nick, Carey, Karine, Riley, (Room 217) Eddie, Bart, Hasan E., Thijs, and Spencer. I would like to heartily thank them for their camaraderie. In particular, I appreciate the walks with Trevor in the first year of the pandemic, the constructive feedback from Natalie on my manuscript drafts, and the support by Bart in the form of baked goods and stimulating conversations during the writing of this very dissertation.

I am grateful for the lifelong affection of my mom (my editor), my dad (my crisis manager), and my sister (my biggest cheerer). Their and my pals' encouragement was one of the pillars of this work.

Finally, I would like to thank the staff of the Department for smoothing my Ph.D. way and acknowledge that my graduate program and this dissertation have been funded in part by the Scientific and Technological Research Council of Turkey (TÜBİTAK) 2213/A scholarship, Air Force Office of Scientific Research (AFOSR) MURI grant FA9550-19-1-0386, and the Joint Center for Aerospace Technology Innovation (JCATI).

Burak Boyacıoğlu

DEDICATION

to my people

Chapter 1

INTRODUCTION

Sensing mechanisms in both biological and engineered dynamic systems are critical as feedback control laws use estimated states based on the measurements from sensors. Observability, a system property, is the ability to determine all system states from the sensor readings. If a system is not observable, a filter cannot fully estimate the system states regardless of how well it is designed. The observability metrics showing the level of observability and their connection to the performance of well-known estimators are studied in the literature. Better estimation of system states allows one to design efficient robust controllers. In this dissertation, our aim is to introduce analytical and numerical observability analysis tools for aerospace systems with neural-inspired measurement functions and to ensure and improve observability for the parameter identification problem. Since the neural encoding mechanism in animal sensing works like an embedded filter, we also present an observability-based sensor placement methodology for systems with process noise.

1.1 Motivations

Our first source of motivation comes from biological systems. Flying insects have the same needs for position and orientation awareness relative to the surrounding environment (pose) as engineered flight vehicles, but they must determine this information with much less computational power and much simpler sensors than the gyroscopes, GPS, accelerometers, and other modern sensors used in air and space vehicles. By studying underlying principles of sensing mechanics and signal processing in biological flight, the potential exists to translate these basic principles to significantly more effective engineered systems. In this dissertation, we consider the use of mechanosensing in insects via strain measurements and neural processing of the resulting strain signals to inform engineered sensing capabilities.

The neural encoding mechanism, which cancels out the stimulus noise, motivated us to study the observability-based sensor placement problem also for stochastic systems. Performance resilience in the presence of sensing noise, environmental disturbances, and modeling imprecision is typically approached from the perspective of robust control theory. However, all feedback-based control techniques, including robust methods, are constrained by the quality of the state estimate as determined both by the accuracy of the estimate (how close the estimate is to the true value) and the precision (how well the estimate is known). Specifically, the precision, as captured by the covariance of the error, directly affects the size of the robustness margin of the controller. Even in linear systems where the separation principle indicates that the design of system control and estimation are independent, the structural properties of sensor location have a direct impact on control performance. As shown in [1], observability in linear systems directly bounds the covariance of the error for estimation filters. Improving the system observability necessarily improves the error covariance, regardless of the particular filter being used. These improvements can be further enhanced by assessing observability in the presence of noise using stochastic tools rather than using the typical deterministic observability framework. Here, we address the use of stochastic observability tools in the task of determining optimal sensor placement and, in particular, optimal sensor placement in the context of sparse sensing.

Finally, we are interested in determining the mass and inertia properties of a mechanical system as it is one of the key elements for studying the motion from the stability and control point of view. In many cases of interest, direct measurement of these properties is not possible, or at least not straightforward, either due to system complexity or to time variations in the values. Aircraft and spacecraft, in particular, demonstrate this level of complexity that requires active identification or estimation of inertial properties [2, 3]. Here, we use nonlinear observability analysis tools and relate observability-based metrics to estimator performance to determine the inertial parameters. In particular, we explore classes of necessary system excitation that enable the determination of the inertial parameters through estimation algorithms.

1.2 Literature Review

1.2.1 Biological Flight: Neural Encoding Mechanism in Sensing

Sensory neurons in an animal's body are responsible for receiving stimulus information and delivering it to the rest of the nervous system [4]. This data transfer relies on action potentials (voltage spikes) [4]. Neural encoding is the mechanism that converts a stimulus into these voltage spikes. This mapping is not fully understood and might be so complex that, for example, a single unit in an animal's retina might be specialized in responding to particular light patterns and to being insensitive to others [5]. Here, the sensing modality on which we will focus is that of mechanosensing. Campaniform sensilla are a type of strain-sensitive mechanoreceptors found in flying insects and use a signal history no longer than 40 ms [6]. Inertial rotations are detectable from this strain information [7, 8] at a rate much faster than the essential but relatively slow visual system [9] thus enabling rapid maneuvers of insects that require sensory feedback. In [10], it is shown that small numbers of sensors inspired by the campaniform sensilla placed in advantageous locations can provide a good classification of strain data from a hawkmoth *Manduca sexta* wing model for the purpose of determining animal rotation rate. Spatial distribution of campaniform sensilla on insect wings in terms of form and function has been further discussed in [11].

A simple model of neural encoding can be obtained by composing a linear filter and a nonlinear decision function. This temporal filter acts like a moving average filter in engineered systems, and the output at any given time is not just a function of the state at that time but is also an explicit function of previous states, that is, neural encoded measurements use the history of the stimulus. The range of filter length is nominally unlimited, however, effective stimulus history for spiking is typically a few hundred milliseconds long in practice [4].

To explore these ideas from an engineering perspective, we here consider neural processing and mechanosensing using systems theoretic tools. In engineering systems, the ability to reconstruct state data from measurements is assessed by the system observability, and the algorithms and devices used to perform the reconstruction are implemented via filters. Since the original introduction of filter design for linear systems such as the Luenberger filter and the Kalman filter [12], the assessment of observability has typically been handled independently from filter design with the idea that any improvements in observability will necessarily benefit any filtering methods used. In nonlinear systems, observability analysis is generally approached using differential geometric methods, and, unlike linear systems where the separation principle guarantees that system actuation has no effect on sensing ability, system actuation in nonlinear systems can affect whether and how well system sensing can be leveraged for state reconstruction [13].

The observability of linear time-invariant systems with output delay was discussed and observer design was given for a class of such systems in [14]. The observability of four common neuron models without output delay and with one measured state was studied in [15]. Recently, a new notion of observability was introduced for systems with commensurate delays in dynamics and measurements [16, 17].

For systems where analytical tools are impractical, the empirical observability Gramian, a numerical tool first introduced by Moore [18] then systematized in [19] for model reduction, can be adopted for local observability analysis. Recently, an empirical Gramian rank condition for weak observability of nonlinear systems and an equivalent sufficient condition based on the minimum singular value of the empirical observability Gramian were developed in [1]. A numerical approximation to obtain a lower bound for the minimum singular value was presented in [20], as the analytical calculations are usually intractable. Finally, a powerful open-source toolbox for the calculation of empirical Gramians, *emgr*, has been introduced for both time-varying and time-invariant systems [21].

The empirical Gramian has also been studied for stochastic systems. In [20], it was shown that if an unobservable system is simulated with the process noise, one may get nonzero observability Gramian eigenvalues, that is, considering uncertainty reveals the observability of the system which is initially determined unobservable using traditional methods. Although a rank condition for the expected value of the empirical observability Gramian for stochastic observability was given for linear systems in the same study using the stochastic observability definition from [22], it was stated that an extension to nonlinear systems was not readily available since the fundamental matrix of linear systems has no analog in the nonlinear context. Finally, it was shown in [1] that the empirical observability Gramian as the perturbation amount goes to zero bounds the Fisher information matrix (FIM), which is elegantly related to the estimator error covariance matrix for linear systems by the Cramér–Rao bound [23].

1.2.2 Engineered Flight: Estimation of Rigid Body Inertial Parameters

Estimation of inertial parameters using input/output behavior is studied in various areas including but not limited to aerospace engineering [24, 3, 25, 26, 27, 2] and robotics [28, 29, 30, 31]. While the focus of most aerospace applications [24, 3, 25, 2] is the identification of the inertia matrix, roboticists [29, 30, 31] and researchers working on the interaction of a spacecraft with another object such as space debris [26, 27] present approaches to estimate the mass and the center of mass in addition to the inertia matrix entries, based on the work by Atkeson *et al* [28]. Finally, the parameter estimation problem specific to unmanned aerial vehicles is widely studied in recent years [32, 33, 34, 35, 36].

The methods used in estimation of inertial parameters include adaptive control laws [24, 26], least squares [3, 27, 28, 29], constrained least squares [25], and the equation-error approach [2]. Better or optimized excitation profiles (inputs) are discussed in some of the studies mentioned above. Single periodic command signals [24], orthogonal multisine excitations [2], finite Fourier series [29, 31], and modified Fourier series [30] are some of these profiles. Underlying the viability of each of these approaches is the requirement that the mathematical relationship between the measurements and the quantities being measured (the states) is invertible. This characteristic is, in fact, observability of the system. While observability is typically applied to systems with dynamics, the methodology is also applicable to parameter identification problems.

1.3 Contributions of this Research

We study the flapping wing dynamics with neural-encoded stimulus (strain) information to be consistent with typical data obtained from biological systems. Since a neural encoder can be modelled as a composite function with delay, existing analytical observability tools are revisited and developed for systems with output delay. To study the observability of systems with composite output functions, we propose an expression of higher-order Lie derivatives of a function composition in the direction of a vector field. The proposition is helpful to relate the observable spaces of systems with and without composite output functions, which does not only allow us to comment on the second function without having analytical results for the first one but also makes it easier to analyze systems with composite output functions by modularizing the task.

We then use the empirical observability Gramian for the observability analysis of an Euler-Lagrange model of hawkmoth *Manduca sexta* flapping wing dynamics with a neural-inspired output function. A convex program with a linear combination of two empirical Gramian-based unobservability metrics as the cost function is posed to optimally place sensors throughout the veins on the wing, and the effect of neural encoding model parameters on observability is explored.

To study the optimal sensor placement problem for the flapping wing dynamics with process noise, we pose a minimization problem where the cost function is the expected value of a linear combination of unobservability metrics based on stochastic empirical observability Gramians calculated for all possible sensor locations. We use a finite element model of a flapping wing instead of an Euler-Lagrange model to be able to include as many modes as possible. The expected values are obtained from Monte Carlo runs, where the number of simulations is chosen based on the convergence of the results.

Finally, we analyze the nonlinear rigid body inertial parameters estimation problem using analytical and numerical observability tools. Since observability is a binary definition, we again implement the empirical observability Gramian to further study the nonlinear system.

We present observability metric distributions throughout the vertical cross-section of the rigid body and depending on the input profile. Unlike Morelli's study [2] in which inputs by devices (aircraft flight control surfaces) were considered, we focus on net force/moment profiles to reach non-system-specific conclusions and test not only multisine signals but also a constant input. Finally, we investigate estimator performances in the cases we studied observability and see necessary Lie brackets are immediately generated when the input is not constant.

1.4 Organization

The remainder of the dissertation has been organized as follows. Next chapter introduces the model of two systems that inspired our work. Chapter 3 gives the background of observability analysis tools and observability metrics. Observability analysis tools for systems with bioinspired measurements are given in Chapter 4. Chapter 5 describes an observability-based optimal sensor placement methodology for stochastic systems. Finally, Chapter 6 discusses approaches to ensure and improve observability via trajectory design. The summary of results and future research directions are given in the last section.

Chapter 2

MODELS OF SYSTEMS OF INTEREST

In this chapter, we introduce two systems of interest: hawkmoth flapping wing dynamics with neural-encoded measurements, and six-degree-of-freedom (6-DoF) rigid body dynamics. Both of these systems are nonlinear, and we will use appropriate tools in the following chapters to study their observability.

2.1 Biological Flight: Hawkmoth Flapping Wing

One of the foci of the work in this dissertation is the study of sensing and state estimation based on neural-encoded strain measurements in flapping wing flight. While the lifting surfaces of the system are assumed to undergo cyclic flapping, the results translate to any lifting surfaces subject to structural loading.

2.1.1 System Dynamics Model

The particular system on which we base our work is the hawkmoth *Manduca sexta*. The hawkmoth wing is modeled as a flexible, thin plate in a rotating, accelerating reference frame as illustrated in Fig. 2.1. Here, we will summarize the results from the Euler-Lagrange modeling in [37]. Details of the dynamic model can be found in the original paper.

The out-of-plane deformation as a function of time and spatial coordinates on the wing is described by

$$w(x_p, y_p, t) = \sum_{i=1}^{n_m} \phi_i(x_p, y_p)\eta_i(t), \tag{2.1}$$

where n_m is the chosen number of modes, and $w \in \mathbb{R}$. The terms $\phi_i(x_p, y_p) \in \mathbb{R}$ and $\eta_i(t) \in \mathbb{R}$ are the free-vibration mode shapes and modal coordinates, respectively. The modes can

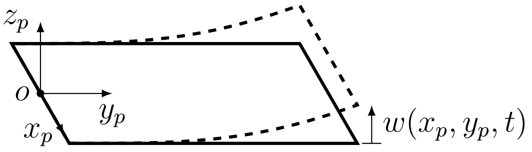

Figure 2.1: Free body diagram of a thin plate with out-of-plane bending in a rotating, accelerating reference frame, simplified from [37].

either be derived analytically such as for the cantilever structure shown in the image or produced numerically through finite element analysis methods. The position, elevation and feathering Euler angles, illustrated in Fig. 2.2, are denoted by ψ, θ and α, respectively. Finally, the axis of feathering rotation relative to the wing coordinate system origin is given as $\begin{bmatrix} 0 & 0 & x_r \end{bmatrix}^\top$.

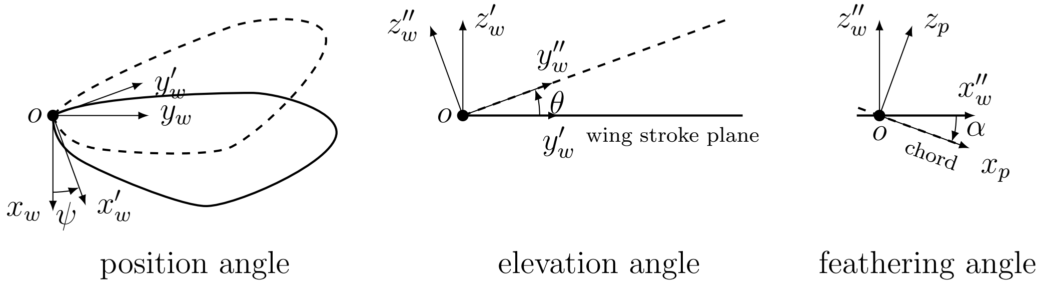

Figure 2.2: The Euler angles, ψ, θ, and α that represent the wing stroke kinematics within the wing frame, $[x_w, y_w, z_w]^\top$ [37].

In the dynamics model here, aerodynamic terms are neglected, which is a reasonable assumption since the aerodynamics are not a significant factor of the motion as shown experimentally in [38] and numerically in [37]. The resultant model of the wing flapping dynamics is

$$\ddot{\boldsymbol{\eta}} + \left(\Omega - (P^2 + Q^2)I_{n_m}\right)\boldsymbol{\eta} = M_a \begin{bmatrix} x_r\left(2PR - \dot{Q}\right) \\ -QR - \dot{P} \\ PR - \dot{Q} \end{bmatrix}, \tag{2.2}$$

where $\Omega \in \mathbb{R}^{n_m \times n_m}$ is the diagonal modal frequency matrix, $M_a \in \mathbb{R}^{n_m \times 3}$ is the applied acceleration mass matrix, and (P, Q, R) and $(\dot{P}, \dot{Q}, \dot{R})$ are wing rotation rates and wing rotational accelerations of the plate coordinate system, respectively. Defining the state vector as $\mathbf{x} = \begin{bmatrix}\boldsymbol{\eta}^\top & \dot{\boldsymbol{\eta}}^\top & P & Q & R\end{bmatrix}^\top$ and the input vector as $\mathbf{u} = \begin{bmatrix}\dot{P} & \dot{Q} & \dot{R}\end{bmatrix}^\top$, the dynamics can be written in control-affine form as:

$$\dot{\mathbf{x}} = \begin{bmatrix} \dot{\boldsymbol{\eta}} \\ -K\boldsymbol{\eta} + (2\mathbf{M_1}x_r + \mathbf{M_3})PR - \mathbf{M_2}QR \\ 0 \\ 0 \\ 0 \end{bmatrix} + \begin{bmatrix} \mathbf{0_{n_m \times 1}} & \mathbf{0_{n_m \times 1}} & \mathbf{0_{n_m \times 1}} \\ -\mathbf{M_2} & -\mathbf{M_1}x_r - \mathbf{M_3} & \mathbf{0_{n_m \times 1}} \\ 1 & 0 & 0 \\ 0 & 1 & 0 \\ 0 & 0 & 1 \end{bmatrix} \mathbf{u}, \tag{2.3}$$

where $K = \Omega - (P^2 + Q^2)\mathbf{I_{n_m}}$ is the stiffness matrix and $\mathbf{M_j}$ denotes the j^{th} column of the matrix M_a. Here, $\top$ denotes the matrix transpose.

2.1.2 Neural Encoding

We review here the relevant neural encoding framework to relate strain due to the out-of-plane deformation, ϵ, to the probability of firing of a neuron, P_{fire}, which we will assume to be the system output. A current, experimentally validated model of the neural response corresponding to strain due to mechanical stimulus, ϵ, on a hawkmoth wing is based on two functions [9]: the spike-triggered average (STA) and a nonlinear activation (NLA) function. The former is, as its name suggests, a functional approximation of the average of the stimuli, which triggered an action potential at time $t = 0$. As given below, it is approximated as an exponentially decaying sinusoidal function with a delay, a [10], its value is zeroed out as t

goes to infinity:

$$\mathrm{STA}(t) = \cos\left(2\pi f_{\mathrm{STA}}(-t+a)\right)\exp\left(\frac{-(-t+a)^2}{b^2}\right). \tag{2.4}$$

The other parameters, b and f_{STA}, are the width and the STA frequency, respectively, and along with the delay, a, they are taken to be constant for the neuron's encoding model. For convenience, an alternative scaled frequency parameter can be defined as:

$$\omega_{\mathrm{STA}} = 2\pi f_{\mathrm{STA}}. \tag{2.5}$$

The convolution of new strain data and the STA can be used to estimate the firing rate of the neuron. However, the rate cannot be negative, and also it requires a saturation value to properly reflect the neuron's nonlinear behaviour [4]. The following nonlinear function of the projected stimulus, ξ, is used to satisfy these requirements:

$$\mathrm{NLA}(\xi) = \frac{1}{1+\exp(-c(\xi-d))}. \tag{2.6}$$

Here, c is the slope and d is the half-maximum position of the NLA function, and again, these parameters are treated as time-invariant variables in the encoding model of a neuron.

Finally, the probability of a neuron firing at the coordinates (x, y) on the wing can be captured by the functional relationship [10]:

$$P_{\mathrm{fire}}(x,y,t) = NLA(\xi(x,y,t)), \tag{2.7}$$

where the projected stimulus, ξ, is assumed to take the form

$$\xi(x,y,t) = \frac{1}{C_\xi}\int_0^N \epsilon(x,y,t-\tau)STA(\tau)d\tau. \tag{2.8}$$

Here, N is the maximum delay, and C_ξ is a normalization constant used to adjust the output scale of the convolution step to match the input scale of the NLA function. Discrete convolution can be used instead of the continuous formulation in Eq. (2.8). In that case, note that C_ξ depends on the step size in the convolution. Determination of C_ξ will be further discussed in Section 4.3. The probability of firing, P_{fire}, will be used as the measurement function in our simulation model.

The full neural encoding model described above is illustrated in Fig. 2.3. Note that mechanisms such as adaptation [39, 40] and spike timing [41, 42] are not included in this model. Note also that a rectified hyperbolic tangent function with another pair of parameters can be used as an alternative to Eq. (2.6) [4].

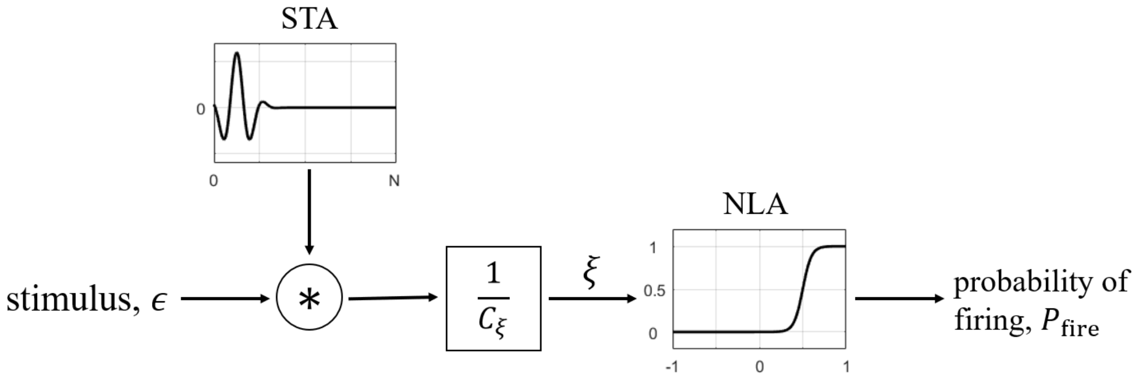

Figure 2.3: The probabilistic firing model of a strain-sensitive neuron takes the strain data as input and calculates the probability of firing, P_{fire}, in two stages. First, the discrete convolution, denoted by $*$, of the strain data with STA(τ) is performed. After the normalization of filtered data by $1/C_\xi$, the probability of firing is given by $NLA(\xi)$.

2.2 *Engineered Flight: 6-DoF Rigid Body*

In this section, we first give a state-space representation of a six-degrees-of-freedom rigid body's dynamics, then simplify it to allow motion only in the vertical plane.

2.2.1 Full Dynamics Model

Consider a rigid body with two fixed reference points: center of mass (CoM) and o_p, the origin of $\mathscr{P}$, a local coordinate system. Let the vectors $\mathbf{q}$ and $\mathbf{p}$ locates them with respect to a reference inertial coordinate system $\mathscr{O}$, and define the location of the center of mass with respect to $\mathscr{P}$ by the vector $\mathbf{c} = \begin{bmatrix} c_x & c_y & c_z \end{bmatrix}^\top$ (Fig. 2.4).

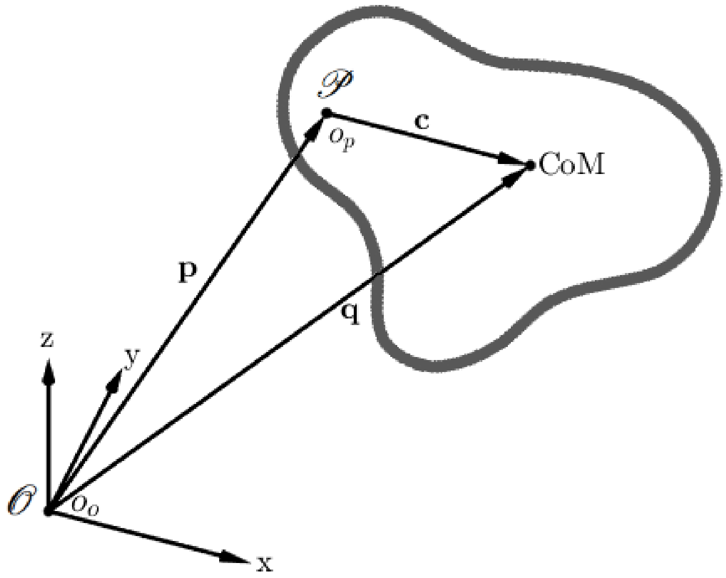

Figure 2.4: The center of mass, the origin of $\mathscr{P}$, and the vectors locating them with respect to each other and with respect to $\mathscr{O}$, a global coordinate system.

Let the force and moment through o_p be $\mathbf{f}_{\mathscr{P}} = \begin{bmatrix} F_x & F_y & F_z \end{bmatrix}^\top$ and $\mathbf{m}_{\mathscr{P}} = \begin{bmatrix} M_x & M_y & M_z \end{bmatrix}^\top$, respectively. Also, let the linear velocity of o_p relative to o_o be $\mathbf{v}_{\mathscr{P}} = \begin{bmatrix} U & V & W \end{bmatrix}^\top$ and the angular velocity of $\mathscr{P}$ relative to $\mathscr{O}$ be $\boldsymbol{\omega}_{\mathscr{P}} = \begin{bmatrix} P & Q & R \end{bmatrix}^\top$. Here, the subscript $\mathscr{P}$ denotes that all the four vectors are expressed in $\mathscr{P}$. Then the matrix form of the equations of motion about o_p is [43]

$$\mathbf{M}\dot{\boldsymbol{\nu}} + \mathbf{C}(\boldsymbol{\nu})\boldsymbol{\nu} = \boldsymbol{\tau}, \tag{2.9}$$

where $\boldsymbol{\nu} = \begin{bmatrix} \mathbf{v}_{\mathscr{P}}^\top & \boldsymbol{\omega}_{\mathscr{P}}^\top \end{bmatrix}^\top$ is a generalized velocity vector expressed in $\mathscr{P}$, $\boldsymbol{\tau} = \begin{bmatrix} \mathbf{f}_{\mathscr{P}}^\top & \mathbf{m}_{\mathscr{P}}^\top \end{bmatrix}^\top$ is a generalized vector of external forces and moments, and the matrices $\mathbf{M}$ and $\mathbf{C}(\boldsymbol{\nu})$ are

$$\mathbf{M} = \begin{bmatrix} m\mathbf{I}_{3\times 3} & -m\mathbf{S}(\mathbf{c}) \\ m\mathbf{S}(\mathbf{c}) & \mathbf{I}_{\mathscr{P}} \end{bmatrix}, \tag{2.10}$$

$$\mathbf{C}(\boldsymbol{\nu}) = \begin{bmatrix} \mathbf{0}_{3\times 3} & -m\mathbf{S}(\mathbf{v}_{\mathscr{P}}) - m\mathbf{S}(\boldsymbol{\omega}_{\mathscr{P}})\mathbf{S}(\mathbf{c}) \\ -m\mathbf{S}(\mathbf{v}_{\mathscr{P}}) + m\mathbf{S}(\mathbf{c})\mathbf{S}(\boldsymbol{\omega}_{\mathscr{P}}) & -\mathbf{S}(\mathbf{I}_{\mathscr{P}}\boldsymbol{\omega}_{\mathscr{P}}) \end{bmatrix}, \tag{2.11}$$

where m is the mass of the body,

$$\mathbf{I}_{\mathscr{P}} = \mathbf{I}_{\mathscr{P}}^{\top} = \begin{bmatrix} I_{xx} & -I_{xy} & -I_{xz} \\ -I_{yx} & I_{yy} & -I_{yz} \\ -I_{zx} & -I_{zy} & I_{zz} \end{bmatrix} \tag{2.12}$$

is the inertia matrix/tensor about o_p, and $\mathbf{S}$ is the cross-product operator such that

$$\mathbf{S}(\boldsymbol{\lambda}) := \begin{bmatrix} 0 & -\lambda_3 & \lambda_2 \\ \lambda_3 & 0 & -\lambda_1 \\ -\lambda_2 & \lambda_1 & 0 \end{bmatrix}. \tag{2.13}$$

The dynamics given in Eq. (2.9) can be written in the state-space form,

$$\dot{\mathbf{x}} = \begin{bmatrix} \boldsymbol{\nu} \\ \mathbf{M}^{-1}(\boldsymbol{\tau} - \mathbf{C}(\boldsymbol{\nu})\boldsymbol{\nu}) \end{bmatrix}, \tag{2.14}$$

where the state vector is defined as $\mathbf{x} = \begin{bmatrix} \mathbf{p}^{\top} & \boldsymbol{\Theta}^{\top} & \mathbf{v}_{\mathscr{P}}^{\top} & \boldsymbol{\omega}_{\mathscr{P}}^{\top} \end{bmatrix}^{\top}$, and $\boldsymbol{\Theta}$ is the vector of Euler angles (ϕ, θ and ψ).

In Subsec. 6.3.1, we will discuss the observability of the ten inertial parameters: the mass, the six unique entries of $\mathbf{I}_{\mathscr{P}}$, and the location of the center of mass, $\mathbf{c}$.

2.2.2 Dynamics Model in 2D

In flight controls engineering, decoupling of the nonlinear equations of motion is possible since the longitudinal and lateral/directional modes of the system are roughly decoupled, given that there is no excitation of the other's modes. In a straight flight condition (no yaw or roll), the motion can be simplified to the vertical plane (longitudinal) dynamics instead of addressing the full flight dynamics [44]. Here, we leverage this decoupling and restrain the rigid body to have three degrees of freedom: translational motion in the xz-plane and rotation in the xz-plane (about the y-axis). By simplifying the generalized velocity vector and the generalized vector of external forces and moments to reflect our assumption, we get $\bar{\mathbf{v}} = \begin{bmatrix} U & W & Q \end{bmatrix}^\top$ and $\bar{\boldsymbol{\tau}} = \begin{bmatrix} F_x & F_z & M_y \end{bmatrix}^\top$, respectively, and the equations of motion (2.9) are reduced to

$$\bar{\mathbf{M}}\dot{\bar{\boldsymbol{\nu}}} + \bar{\mathbf{C}}(\bar{\boldsymbol{\nu}})\bar{\boldsymbol{\nu}} = \bar{\boldsymbol{\tau}}, \tag{2.15}$$

where

$$\bar{\mathbf{M}} = \begin{bmatrix} m & 0 & mc_z \\ 0 & m & -mc_x \\ mc_z & -mc_x & I_{yy} \end{bmatrix} \tag{2.16}$$

is the system inertia matrix, and the Coriolis–centripetal matrix is

$$\bar{\mathbf{C}}(\bar{\boldsymbol{\nu}}) = \begin{bmatrix} 0 & 0 & -m(c_xQ - W) \\ 0 & 0 & -m(c_zQ + U) \\ m(c_xQ - W) & m(c_zQ + U) & 0 \end{bmatrix}. \tag{2.17}$$

Again, we express the dynamics in state-space form while also including the velocities in the derivative where the state vector is defined as $\bar{\mathbf{x}} = \begin{bmatrix} p_x & p_z & \theta & U & W & Q \end{bmatrix}^\top$:

$$\dot{\bar{\mathbf{x}}} = \begin{bmatrix} \bar{\boldsymbol{\nu}} \\ \bar{\mathbf{M}}^{-1}(\bar{\boldsymbol{\tau}} - \bar{\mathbf{C}}(\bar{\boldsymbol{\nu}})\bar{\boldsymbol{\nu}}) \end{bmatrix}, \tag{2.18}$$

and the inverse of the system inertia matrix is

$$\bar{\mathbf{M}}^{-1} = \frac{1}{mc_x^2 + mc_z^2 - I_{yy}} \begin{bmatrix} c_x^2 - \frac{I_{yy}}{m} & c_x c_z & c_z \\ c_x c_z & c_z^2 - \frac{I_{yy}}{m} & -c_x \\ c_z & -c_x & -1 \end{bmatrix}. \tag{2.19}$$

Notice that the reduced dynamics do not have c_y as a parameter, and the only inertia matrix entry appears in Eq. (2.18) is the moment of inertia about the y-axis, I_{yy}. In Subsec. 6.3.1, we will discuss the observability of the four inertial parameters: the mass, c_x, c_z, and I_{yy}.

Chapter 3

OBSERVABILITY BACKGROUND

As a fundamental system property, observability characterizes the existence of an invertible mapping from measurements to state space. In this chapter, analytical and numerical tools for observability analysis of systems in some standard forms will be summarized along with the terminology used in the rest of the dissertation.

3.1 Analytical Observability

Formally, a dynamic system is ***observable*** if there exists a finite time, $T > 0$, such that the knowledge of the input and the output over the time interval $[0, T]$ is sufficient to uniquely determine any unknown initial state [45]. If an unknown initial state can be uniquely determined in an open neighborhood of itself, then the system is ***locally weakly observable.*** If the system is locally weakly observable at any point in the state space, then the system is called *(globally)* ***weakly observable.***

3.1.1 Linear Systems

Consider the continuous-time/discrete-time linear time-invariant control system

$$\Sigma_{\text{CT-LTI}}: \begin{array}{c} \dot{\mathbf{x}}(t) = A\mathbf{x}(t) + B\mathbf{u}(t) \\ \mathbf{y}(t) = C\mathbf{x}(t), \end{array} \quad / \quad \Sigma_{\text{DT-LTI}}: \begin{array}{c} \mathbf{x}_{k+1} = A\mathbf{x}_k + B\mathbf{u}_k \\ \mathbf{y}_k = C\mathbf{x}_k, \end{array} \tag{3.1}$$

where $\mathbf{x} \in \mathbb{R}^n$ is the vector of states, $\mathbf{u} \in \mathbb{R}^{n_i}$ is the vector of inputs, and $\mathbf{y} \in \mathbb{R}^p$ is the vector of outputs. It is a well-known theorem that $\Sigma_{\text{CT-LTI}}/\Sigma_{\text{DT-LTI}}$ is observable if and only if the

T-step observability matrix

$$\mathcal{O}_T = \begin{bmatrix} C \\ CA \\ \vdots \\ CA^{T-1} \end{bmatrix} \tag{3.2}$$

is full column rank for some $T \geq n$ where n is the number of system states [46]. Since the rank of the observability matrix remains the same after the n-th step, which can be shown using the Cayley–Hamilton theorem (see [47, pp.6-7]), it is sufficient to check the observability rank condition for $T = n$. If the kernel of $\mathcal{O}_n$ is not equal to the zero subspace, then the system is called ***unobservable.***

3.1.2 Nonlinear Systems

Consider continuous-time nonlinear time-invariant systems in control-affine form:

$$\Sigma_{\text{NLTI}}: \quad \begin{aligned} \dot{\mathbf{x}}(t) &= \mathbf{f_0}(\mathbf{x}(t)) + \sum_{i=1}^{n_i} \mathbf{f_i}(\mathbf{x}(t))u_i(t) \\ \mathbf{y}(t) &= \mathbf{h}(\mathbf{x}(t)). \end{aligned} \tag{3.3}$$

The observability of such systems can be studied using differential geometry methods [13, 48]. To begin, one constructs the observability Lie algebra, $\mathcal{G}$, also termed the *observation space*, for Σ_{NLTI} [48]:

$$\mathcal{G} = \text{span}\{L_{\mathbf{X}_1} \cdots L_{\mathbf{X}_k}\mathbf{h},\ k = 0, 1, \dots n-1,\ \mathbf{X}_k \in \{\mathbf{f_0}, \dots, \mathbf{f_{n_i}}\}\}, \tag{3.4}$$

where the Lie derivative, $L_{\mathbf{f_i}}\mathbf{h}$, denotes the derivative of the vector-valued function $\mathbf{h}$ with respect to $\mathbf{x}$ on the vector field $\mathbf{f_i}$, i.e.,

$$L_{\mathbf{f_i}}\mathbf{h} = \frac{\partial \mathbf{h}}{\partial \mathbf{x}}\mathbf{f_i}, \tag{3.5}$$

and repeated Lie derivatives are calculated as $L_{\mathbf{f}}^{k}\mathbf{h} = L_{\mathbf{f_i}} L_{\mathbf{f_i}}^{k-1}\mathbf{h}$. A rank condition for weak observability is then

$$\operatorname{rank}(\mathrm{d}\mathcal{G}) = n, \tag{3.6}$$

where $\mathrm{d}\mathcal{G}$ is the set of all gradients of the vector fields in $\mathcal{G}$ [13], i.e.,

$$\mathrm{d}\mathcal{G} = \{\mathrm{d}\phi : \phi \in \mathcal{G}\}. \tag{3.7}$$

Notice the control vector fields, $\mathbf{f_1}, \ldots, \mathbf{f_{n_i}}$, appear in the observability Lie algebra, that is, unlike linear systems where the separation principle guarantees that system actuation has no effect on sensing ability, the coupling of actuation with measurements can affect whether and how well system sensing can be leveraged for state reconstruction [13], e.g., as illustrated in [37, 49], having a control term can make an unobservable control-free nonlinear system observable.

3.2 Observability Gramians and Output Sensitivity

The observability rank conditions presented in the previous section provide a binary measure of observability and require the system to be expressed in certain forms. On the other hand, as shown below, quantitative measures of observability can be obtained via the analytical observability Gramian or the empirical observability Gramian matrix [50] which, at the cost of some accuracy, has the benefit of not requiring analytical calculations such as the derivative of the measurement function, $\mathbf{h}(\mathbf{x})$, with respect to $\mathbf{x}$.

In continuous-time linear systems on the form of Eq. (3.1), observability can also be determined from the nonnegative-definite symmetric matrix, $W_o(t_0, t_1)$, termed the *observability Gramian* [51] where

$$W_o(t_0, t_1) = \int_{t_0}^{t_1} e^{A^\top t} C^\top C e^{At} dt \in \mathbb{R}^{n \times n}. \tag{3.8}$$

If this matrix is full (column/row) rank, then the system is observable at time $t = t_0$. In addition, the observability Gramian has the benefit of being a convex function to which a norm can be applied and a more refined measure of observability can be determined than the binary results above. Of further interest is the relationship between $W_o(t_0, t_1)$ and the sensitivity of the output to the state being estimated, $\mathbf{x}(t_0) = \mathbf{x}_0$. Specifically, for linear time-invariant systems, one has the relation $\partial_{\mathbf{x}_0}\mathbf{y}(t) = Ce^{At}$ which allows us to write

$$W_o(t_0, t_1) = \int_{t_0}^{t_1} \partial_{\mathbf{x}_0}\mathbf{y}^\top(t)\partial_{\mathbf{x}_0}\mathbf{y}(t)dt \in \mathbb{R}^{n\times n}. \tag{3.9}$$

In this last form, the observability Gramian does not require the structure of a linear system, simply that the partial derivatives of the output with respect to the initial state can be computed [51].

To implement the empirical approach, one simulates the system dynamics with perturbed initial conditions and an input sequence, $\mathbf{u} \in \mathcal{U}$, where $\mathcal{U}$ is the set of permissible controls. Specifically, let $\mathbf{y}^{+i}$ and $\mathbf{y}^{-i}$ be the simulation outputs resulting from simulating the system dynamics with the nominal initial condition of state $\mathbf{x}_{0,i}$ perturbed respectively in the positive and negative directions by amount ε. Then the empirical observability Gramian is computed as

$$W_o^\varepsilon(t_1, \mathbf{x}_0, \mathbf{u}) = \frac{1}{4\varepsilon^2}\int_0^{t_1} \Phi^\varepsilon(t, \mathbf{x}_0, \mathbf{u})^\top \Phi^\varepsilon(t, \mathbf{x}_0, \mathbf{u})dt \in \mathbb{R}^{n\times n}, \tag{3.10}$$

where $\mathbf{x}_0$ is the initial state and

$$\Phi^\varepsilon(t, \mathbf{x}_0, \mathbf{u}) = \begin{bmatrix}\mathbf{y}^{+1} - \mathbf{y}^{-1} & \cdots & \mathbf{y}^{+n} - \mathbf{y}^{-n}\end{bmatrix}. \tag{3.11}$$

In linear system observability analysis, the observability Gramian (3.8) must be full rank for the system to be observable. The following theorem suggests a similar rank condition for W_o^ε.

Theorem 1 *[1] Given Σ_{NLTI}, if there exists $\mathbf{u} \in \mathcal{U}$ such that*

$$\operatorname{rank}\left(\lim_{\varepsilon \to 0} W_o^{\varepsilon}(t_1, \mathbf{x}_0, \mathbf{u})\right) = n \tag{3.12}$$

for some $t_1 > 0$, then the system is weakly observable at $\mathbf{x}_0$.

Another sufficient condition can be stated based on the minimum singular value of the empirical observability Gramian, $\underline{\sigma}(W_o^{\varepsilon})$. This theorem is useful as W_o^{ε} is full rank by construction and positive definite, so the singular values are at the same time the eigenvalues.

Theorem 2 *[1] If there exists $\mathbf{u} \in \mathcal{U}$ such that*

$$\underline{\sigma}(W_o^{\varepsilon}) > \sup_{t \in [0, t_1]} \left(\frac{\sqrt{n}\varepsilon^2 t_1}{3} \left\| \frac{\partial \mathbf{y}}{\partial \mathbf{x}_0} \right\|_2 \Gamma + \frac{n \varepsilon^4 t_1}{36} \Gamma^2 \right), \tag{3.13}$$

for some $t_1 > 0$ where

$$\Gamma(t, \mathbf{x}_0, \mathbf{u}) = \max_i \sup_{\boldsymbol{\eta} \in \mathcal{I}_i^{\varepsilon}} \left\| D^3 y(\boldsymbol{\eta})(\mathbf{e}_i, \mathbf{e}_i, \mathbf{e}_i) \right\|_1, \tag{3.14}$$

the elements of the standard basis in $\mathbb{R}^n$ are denoted by $\mathbf{e}_i$, and $\mathcal{I}_i^{\varepsilon} = [\mathbf{x}_0 - \varepsilon \mathbf{e}_i, \mathbf{x}_0 + \varepsilon \mathbf{e}_i]$ is the closed line segment from $\mathbf{x}_0 - \varepsilon \mathbf{e}_i$ to $\mathbf{x}_0 + \varepsilon \mathbf{e}_i$, then the system is weakly observable at $\mathbf{x}_0$.

Although these results are important as they are equivalent to the observability Lie algebra approach in determining nonlinear system observability, the analytical calculations in Theorem 2 are usually intractable. A subsequent study [20] proposes to use second-order central difference methods to approximate $\partial \mathbf{y} / \partial \mathbf{x}_0$ and $D^3 y(\eta)(\mathbf{e}_i, \mathbf{e}_i, \mathbf{e}_i)$. The approximation for the former is

$$\frac{\partial \mathbf{y}}{\partial \mathbf{x}_0}(t_k) \approx \frac{\Phi^{\varepsilon}(t_k)}{2\varepsilon}. \tag{3.15}$$

To approximate the third Fréchet derivative, $\mathcal{I}_i^{\varepsilon}$ is discretized into P points, $\mathbf{x}_{i,j}$, for $j \in \{1, \ldots, P\}$, then the trajectory is simulated four times per point, and the following calculation is executed:

$$D^3 y\left(\mathbf{x}_{i,j}\right)\left(\mathbf{e}_i, \mathbf{e}_i, \mathbf{e}_i\right) \approx \frac{1}{dx^3}\left(\frac{1}{2}\mathbf{y}^{++i}\left(t_k, \mathbf{x}_{i,j}\right) - \mathbf{y}^{+i}\left(t_k, \mathbf{x}_{i,j}\right) + \mathbf{y}^{-i}\left(t_k, \mathbf{x}_{i,j}\right) - \frac{1}{2}\mathbf{y}^{--i}\left(t_k, \mathbf{x}_{i,j}\right)\right). \tag{3.16}$$

Here,

$$\mathbf{y}^{++i}\left(t, \mathbf{x}_{i,j}, \mathbf{u}\right) = \mathbf{h}\left(x\left(t, \mathbf{x}_{i,j} + 2dx\mathbf{e}_i, \mathbf{u}\right)\right) \tag{3.17}$$

and

$$\mathbf{y}^{--i}\left(t, \mathbf{x}_{i,j}, \mathbf{u}\right) = \mathbf{h}\left(x\left(t, \mathbf{x}_{i,j} - 2dx\mathbf{e}_i, \mathbf{u}\right)\right) \tag{3.18}$$

for some small $dx \in \mathbb{R}$. Using these approximations to obtain a lower bound for $\underline{\sigma}(W_o^\varepsilon)$ does not provide a sufficient condition for weak observability. However, they give a general idea of the lower bounds, and we will be leveraging these approximations in the following chapters.

3.3 Observability Metrics

In this subsection, we summarize observability metrics based on the (empirical) observability Gramian. But first, let us mention the four axioms introduced by Müller and Weber [52] to define a quality of measure: A scalar value $\mu(P)$ is called a measure of quality if and only if

- $\mu(P) = 0$ for P with $\det(P) = 0$,
- $\mu(P) > 0$ for P with $\det(P) > 0$,
- $\mu(kP) = k\mu(P)$ for $k \geq 0$,
- $\mu\left(P_1\right) \geq \mu\left(P_2\right) + \mu\left(P_3\right)$ for $P_1 = P_2 + P_3$,

where P denotes a positive (semi-)definite matrix associated with the system. If P is the observability Gramian, then these axioms say: a) if a system is unobservable, then the metric should be zero, b) if a system is observable, then its metric should be positive, c) if all the outputs of a system are scaled by a number, then the metric should be scaled by the same number, and d) two outputs should have more or equal energy together than the case they acquire data separately.

Krener and Ide [50] introduced two unobservability metrics based on the empirical Gramian: the reciprocal of the minimum eigenvalue of the observability Gramian, $1/\underline{\lambda}(W_o)$, which is also called the unobservability index, $\nu(W_o)$, and the condition number of the same matrix, $\kappa(W_o) = \bar{\lambda}(W_o)/\underline{\lambda}(W_o)$. The former determines the weakness of the chain by its least strong link. The latter shows the balanced contribution of states to the output, and its value is desired to be one assuming that the output coordinates are already scaled. Notice that for $\mu = 1/\kappa(W_o)$, the third axiom does not hold since the scaling of the Gramian would not change the condition number. Also, as pointed out in [50], the last axiom is also not always true for this metric. Still, the condition number of the observability Gramian is a significant measure as it shows how well-conditioned the estimation problem is.

In [53], the optimal phasor measurement unit (PMU) placement problem was formulated to maximize the determinant of the observability Gramian, $\det(W_o)$, which is equal to the product of all the eigenvalues of W_o, but it was advised that one should check the minimum eigenvalue to be at an acceptable level. Since the maximization of $\det(W_o)$ is not a convex problem, $\log\det(W_o)$ is sometimes preferred instead, e.g., in [54]. However, an alternative, the n-th root of the determinant, $[\det(W_o)]^{1/n}$, is not only concave but, as stated in [55], also follows all the other axioms above.

Although the trace and the spectral radius might be useful for applications like model reduction, they are not usually the first choice for observability analysis as they are not able to catch the case when W_o is singular and violate the first axiom.

Chapter 4

NEURAL-INSPIRED MEASUREMENT OBSERVABILITY

In this chapter, we discuss systems with output delay and systems with a composite output function. As mentioned in Chapter 2, the neural encoding mechanism in animal sensing can be modeled as a combination of these two output types.

4.1 Observability Analysis of Systems with Output Delay

In this section, we first present our approach to the observability analysis of linear systems with output delay and by relating the observability matrices of the cases of delay-free and delayed measurements show that having a filter can make an observable system unobservable, but not vice versa. Second, we use the existing geometrical methods to study the related observability of nonlinear autonomous systems.

In real systems, all measurements are delayed as compared to the standard non-delayed model. When the output is an explicit function of a state vector at a previous time, it is said the system has an ideal delay. Whereas here we consider systems with an output function explicitly depending on more than one previous state vectors.

4.1.1 Linear Systems with Output Delay

Consider the following discrete-time time-invariant system with linear dynamics and delay:

$$\Sigma_{\text{LTIw/D}}: \quad \begin{aligned} \mathbf{x}_{k+1} &= A\mathbf{x}_k + B\mathbf{u}_k \\ \mathbf{y}_k &= \sum_{\tau=0}^{N} C_\tau \mathbf{x}_{k-\tau}. \end{aligned} \tag{4.1}$$

Here, $\mathbf{x}_{k-N}$ is the oldest state upon which $\mathbf{y}_k$ explicitly depends.

Theorem 3 *The system with delay (4.1) is observable if and only if the $pn \times n$ observability matrix*

$$\bar{\mathcal{O}} = \begin{bmatrix} \bar{C} \\ \bar{C}A \\ \vdots \\ \bar{C}A^{n-1} \end{bmatrix}, \tag{4.2}$$

is full column rank where the $p \times n$ matrix, $\bar{C}$, is defined as:

$$\bar{C} = \sum_{\tau=0}^{N} C_\tau A^{N-\tau}. \tag{4.3}$$

Proof First consider the measurement at time $k = 0$, $\mathbf{y}_0$, and use the system dynamics to relate it to only the state vector, $\mathbf{x}_{-N}$:

$$\begin{aligned}
\mathbf{y}_0 &= C_0\mathbf{x}_0 + C_1\mathbf{x}_{-1} + \cdots + C_N\mathbf{x}_{-N} \\
&= C_0(A\mathbf{x}_{-1} + B\mathbf{u}_{-1}) + C_1\mathbf{x}_{-1} + C_2\mathbf{x}_{-2} + \cdots + C_N\mathbf{x}_{-N} \\
&= C_0B\mathbf{u}_{-1} + (C_0A + C_1)\mathbf{x}_{-1} + C_2\mathbf{x}_{-2} + \cdots + C_N\mathbf{x}_{-N} \\
&\vdots \\
&= \sum_{\tau=1}^{N}\left(\sum_{i=1}^{\tau} C_{i-1}A^{\tau-i}\right)B\mathbf{u}_{-\tau} + \sum_{\tau=0}^{N} C_\tau A^{N-\tau}\mathbf{x}_{-N}
\end{aligned}$$

Hence, by defining

$$\underline{\mathbf{y}}_k = \mathbf{y}_k - \sum_{\tau=1}^{N}\left(\sum_{i=1}^{\tau} C_{i-1}A^{\tau-i}\right)B\mathbf{u}_{k-\tau}, \tag{4.4}$$

a set of n consecutive measurements can be stated as the following as is usually done for delay-free systems:

$$\begin{aligned}
\underline{\mathbf{y}}_k &= \bar{C}\mathbf{x}_{k-N} \\
\underline{\mathbf{y}}_{k+1} &= \bar{C}\mathbf{x}_{k-N+1} = \bar{C}A\mathbf{x}_{k-N} + CB\mathbf{u}_{k-N} \\
&\vdots \\
\underline{\mathbf{y}}_{k+n-1} &= \bar{C}\mathbf{x}_{k-N+n-1} = \bar{C}A^{n-1}\mathbf{x}_{k-N} + \sum_{j=0}^{n-2} \bar{C}A^{n-2-j}B\mathbf{u}_{k-N+j}.
\end{aligned}$$

Finally, we can write

$$\underline{\underline{\mathbf{y}}} = \bar{\mathcal{O}}\mathbf{x}_{k-N}, \tag{4.5}$$

where the $pn \times 1$ vector $\underline{\underline{\mathbf{y}}}$ is defined as:

$$\underline{\underline{\mathbf{y}}} = \begin{bmatrix} \underline{\mathbf{y}}_k \\ \underline{\mathbf{y}}_{k+1} \\ \vdots \\ \vdots \\ \underline{\mathbf{y}}_{k+n-1} \end{bmatrix} - \begin{bmatrix} \mathbf{0_{p\times n_i}} & \mathbf{0_{p\times n_i}} & \cdots & \mathbf{0_{p\times n_i}} \\ \bar{C}B & \mathbf{0_{p\times n_i}} & \ddots & \mathbf{0_{p\times n_i}} \\ \vdots & \ddots & \vdots & \vdots \\ \vdots & \vdots & \ddots & \vdots \\ \bar{C}A^{n-2}B & \bar{C}A^{n-3}B & \cdots & \bar{C}B \end{bmatrix} \begin{bmatrix} \mathbf{u}_{k-N} \\ \mathbf{u}_{k-N+1} \\ \vdots \\ \mathbf{u}_{k-N+n-2} \end{bmatrix}. \tag{4.6}$$

Here, $\underline{\underline{\mathbf{y}}}$ is known, and $\mathbf{x}_{k-N}$ can be uniquely determined if and only if the null space of the observability matrix is zero, $\mathcal{N}(\bar{\mathcal{O}}) = \{\mathbf{0}\}$. ■

Theorem 3 also implies that the observability of linear systems with delay does not depend on the input, just as in the delay-free case.

In the rest of this section, two special cases will be considered. In the first case, the same filter coefficients are used for each output, $(\mathbf{y}_k)_i$, and the coefficient matrices are assumed to be a scaled version of the measurement matrix, C, of Eq. (3.1). In the case of heterogeneous sensing, the coefficient matrices are obtained by scaling each row of C separately. It will be shown that in both of these noteworthy cases, having an output delay does not make an unobservable delay-free linear system observable. This result is an expected one because the methods we use here are just an application of well-known types of filtering.

Uniform Sensing

If $C_\tau = \gamma_\tau C$ in Eq. (4.1) where $\gamma_\tau \in \mathbb{R}$ is a scalar, then the observability matrix (4.2) becomes

$$\bar{\mathcal{O}} = \begin{bmatrix} \gamma_N C + \gamma_{N-1} CA + \cdots + \gamma_0 CA^N \\ \gamma_N CA + \gamma_{N-1} CA^2 + \cdots + \gamma_0 CA^{N+1} \\ \vdots \\ \gamma_N CA^{n-1} + \gamma_{N-1} CA^n + \cdots + \gamma_0 CA^{N+n-1} \end{bmatrix}. \tag{4.7}$$

Corollary 1 *If the delay-free system, $\Sigma_{DT\text{-}LTI}$, is unobservable, then $\Sigma_{LTIw/D}$ with uniform sensing is also unobservable. Also, if the matrix polynomial $(I\gamma_N + A\gamma_{N-1} + \cdots + A^N\gamma_0)$ is nonsingular, then* $\mathrm{rank}(\bar{\mathcal{O}}) = \mathrm{rank}(\mathcal{O}_n)$.

Proof The observability matrix $\bar{\mathcal{O}}$ can be written as:

$$\begin{aligned} \bar{\mathcal{O}} &= \gamma_N \begin{bmatrix} C \\ CA \\ \vdots \\ CA^{n-1} \end{bmatrix} + \gamma_{N-1} \begin{bmatrix} CA \\ CA^2 \\ \vdots \\ CA^n \end{bmatrix} + \cdots + \gamma_0 \begin{bmatrix} CA^N \\ CA^{N+1} \\ \vdots \\ CA^{N+n-1} \end{bmatrix} \\ &= \mathcal{O}_n (I_n \gamma_N + A\gamma_{N-1} + \cdots + A^N \gamma_0), \end{aligned} \tag{4.8}$$

and the result follows directly. ■

The exceptional case of the singularity of the matrix polynomial is illustrated in the last subsection.

Heterogeneous Sensing

If $C_\tau = \operatorname{diag}(\gamma_{1\tau}, \gamma_{2\tau}, \dots, \gamma_{p\tau})C = G_\tau C$ in Eq. (4.1), then the observability matrix (4.2) becomes

$$\bar{\mathcal{O}} = \begin{bmatrix} G_N C + G_{N-1}CA + \cdots + G_0 CA^N \\ G_N CA + G_{N-1}CA^2 + \cdots + G_0 CA^{N+1} \\ \vdots \\ G_N CA^{n-1} + G_{N-1}CA^n + \cdots + G_0 CA^{N+n-1} \end{bmatrix} \tag{4.9}$$

$$= \begin{bmatrix} G_N & G_{N-1} & \cdots & G_0 & 0 & \cdots & 0 \\ 0 & G_N & G_{N-1} & \cdots & G_0 & \cdots & 0 \\ \vdots & \ddots & \ddots & \ddots & \ddots & \ddots & \vdots \\ 0 & \cdots & 0 & G_N & G_{N-1} & \cdots & G_0 \end{bmatrix} \begin{bmatrix} C \\ CA \\ \vdots \\ CA^{N+n-1} \end{bmatrix}. \tag{4.10}$$

Corollary 1 *If the delay-free system, $\Sigma_{DT\text{-}LTI}$, is unobservable, then $\Sigma_{LTIw/D}$ with heterogeneous sensing is also unobservable.*

Proof Since $\operatorname{rank}(\mathcal{O}_{N+n}) = \operatorname{rank}(\mathcal{O}_n)$, and the rank of a matrix product is no larger than the minimum of the ranks of the factors, it can be stated that $\operatorname{rank}(\bar{\mathcal{O}}) \leq \operatorname{rank}(\mathcal{O}_n)$. ■

Note that this analysis is also valid where G_τ is not a diagonal matrix.

Systems where each output has a different window size are not within the scope of this study. However, an approach for the analysis of such systems is outlined as follows. Consider the case where $(\mathbf{y}_k)_i = \sum_{\tau=0}^{N_i} \gamma_{i\tau} C\mathbf{x}_{k-\tau}$. Then define $N = \max(N_1, N_2, \dots, N_p)$, and construct output matrices as $C_\tau = \operatorname{diag}(\gamma_{1\tau}, \gamma_{2\tau}, \dots, \gamma_{p\tau})C$ by letting $\gamma_{i\tau} = 0$ if it is not already defined. Finally, a sufficient observability condition can be obtained by following similar steps to the constant-history-length heterogeneous sensing case.

4.1.2 Nonlinear Systems with Delay

In this section, we describe how the existing geometrical methods presented in Chapter 3 can be implemented for nonlinear systems with delay. Our analytical approach is restricted to autonomous systems where $\mathbf{u} = \mathbf{0}$ because of the constraints below. The non-autonomous system can be studied using the empirical observability Gramian.

Consider the following class of autonomous systems with output delay:

$$\Sigma_{\text{NLTIw/D}} : \quad \begin{aligned} \dot{\mathbf{x}}(t) &= \mathbf{f_0}(\mathbf{x}(t)), \\ y_i(t) &= \int_0^N C(\tau) x_j(t-\tau) d\tau, \quad i = 1, \ldots, p, \; j \in \{1, \ldots, n\} \end{aligned} \tag{4.11}$$

Here, each of the p outputs is the convolution of one of the states with the same coefficient function, C. Assume that all states appearing in the output vector can be obtained as a function of $\mathbf{x}(t-N)$ and τ, that is, assume that there exists a vector function, $\bar{\mathbf{h}}_{\text{aux}}$, such that

$$x_j(t-\tau) = \bar{h}_{\text{aux}_i}(\mathbf{x}(t-N), \tau). \tag{4.12}$$

Since it is possible to write the output as a function of only $\mathbf{x}(t-N)$, the Lie algebraic approach can be used for the observability analysis as is done for delay-free nonlinear systems. The observation space, $\bar{\mathcal{G}}$, for $\Sigma_{\text{NLTIw/D}}$ is obtained by

$$\bar{\mathcal{G}} = \text{span}\{L_{\mathbf{f}_0}^{n-1}\bar{\mathbf{h}}, \ldots, L_{\mathbf{f}_0}\bar{\mathbf{h}}, \bar{\mathbf{h}}\}, \tag{4.13}$$

where the Lie derivative is defined by

$$L_{\mathbf{f}_0}\bar{\mathbf{h}} = \frac{\partial \bar{\mathbf{h}}(\mathbf{x}(t-N))}{\partial \mathbf{x}(t-N)} \mathbf{f}_0, \tag{4.14}$$

and $\bar{\mathbf{h}}$ is defined in

$$\mathbf{y}(t) = \bar{\mathbf{h}}(\mathbf{x}(t-N)) = \int_0^N C(\tau) \bar{\mathbf{h}}_{\text{aux}}(\mathbf{x}(t-N), \tau) d\tau. \tag{4.15}$$

Here, obtaining the set of all gradients of the vector fields in $\bar{\mathcal{G}}$, $\mathrm{d}\bar{\mathcal{G}} = \{\mathrm{d}\phi : \phi \in \bar{\mathcal{G}}\}$, requires solving the integral in Eq. (4.15) which is usually a cumbersome process. The following proposition is offered to sometimes bypass this process.

Theorem 4 *Define* $\bar{\mathcal{G}}_{aux} = \mathrm{span}\{L_{\mathbf{f}_0}^{n-1}\bar{\mathbf{h}}_{aux}, \ldots, L_{\mathbf{f}_0}\bar{\mathbf{h}}_{aux}, \bar{\mathbf{h}}_{aux}\}$ *and* $\mathrm{d}\bar{\mathcal{G}}_{aux} = \{\mathrm{d}\phi : \phi \in \bar{\mathcal{G}}_{aux}\}$. *If the rows/columns of* $d\bar{\mathcal{G}}_{aux}$ *are linearly dependent, then* $\mathrm{d}\bar{\mathcal{G}}$ *is rank-deficient.*

Proof Let $\mathrm{rank}\,(d\bar{\mathcal{G}}_{\mathrm{aux}}) < n$. Then the Leibniz integral rule allows us to write

$$d\bar{\mathcal{G}} = \int_0^N C(\tau) d\bar{\mathcal{G}}_{\mathrm{aux}} d\tau. \tag{4.16}$$

If the columns/rows of $d\bar{\mathcal{G}}_{\mathrm{aux}}$ are linearly dependent, then $\mathrm{rank}\,(d\bar{\mathcal{G}}) < n$. ■

4.1.3 Example Systems

We first give an example to illustrate the observability analysis of a linear system with output delay. Then we investigate the observability of flapping wing dynamics with filtered measurements.

Double Integrator Dynamics with Differencing Output

Consider the discretized dynamics of a double integrator with the sampling period, T_s, and differencing output:

$$\mathbf{x}_{k+1} = \begin{bmatrix} 1 & T_s \\ 0 & 1 \end{bmatrix} \mathbf{x}_k, \qquad y_k = \begin{bmatrix} 1 & 0 \end{bmatrix} \mathbf{x}_k - \begin{bmatrix} 1 & 0 \end{bmatrix} \mathbf{x}_{k-1}. \tag{4.17}$$

Here, we obtain $\bar{C}$ as

$$\bar{C} = \begin{bmatrix} 1 & 0 \end{bmatrix} \begin{bmatrix} 1 & T_s \\ 0 & 1 \end{bmatrix} - \begin{bmatrix} 1 & 0 \end{bmatrix} = \begin{bmatrix} 0 & T_s \end{bmatrix},$$

and the observability matrix becomes

$$\bar{O} = \begin{bmatrix} 0 & T_s \\ 0 & T_s \end{bmatrix}$$

which is rank-deficient for any T_s. As Cor. 1 suggests, this result could also be obtained by showing that

$$I_n\gamma_1 + A\gamma_0 = I_2 - \begin{bmatrix} 1 & T_s \\ 0 & 1 \end{bmatrix}$$

is singular for any T_s. That is to say, the double integrator dynamics with differencing output (4.17) is unobservable, although the same system with the output $y_k = \begin{bmatrix} 1 & 0 \end{bmatrix} \mathbf{x}_k$ is observable.

Flexible Wing Flapping Dynamics with Output Delay

Using the Lie algebraic approach to observability, it has previously been shown that the delay-free system (2.3) with the output, $y = \eta$, is observable if and only if $\mathbf{u} \neq \mathbf{0}$, i.e., the rotation rates are observable from wing strain measurements if there exists angular acceleration in at least one axis [37]. Here, to study the observability of the system with delay, the output is taken as:

$$y(t) = \int_0^N C(\tau)\eta(t-\tau)d\tau, \tag{4.18}$$

where C is now a scalar-valued function, and it will be demonstrated that the control-free system remains unobservable when the linear filter (4.18) is applied. First, the solution of the system of differential equations (2.3) is utilized to construct $d\bar{\mathcal{G}}_{\text{aux}}$ as defined in Eq. (4.16). Since the case when $\mathbf{u} = \mathbf{0}$ is considered, it can be assumed that the angular rates are constant although their values are unknown. This fact leads to the reduction of the dynamics (2.2) to a second-order ordinary differential equation of the following form:

$$\begin{aligned}\eta(t-\tau) =&\bar{\mathbf{h}}_{\text{aux}}(\mathbf{x}(t-N),\tau) = \cos(\sqrt{K}\bar{\tau})\eta(t-N) + K^{-1/2}\sin(\sqrt{K}\bar{\tau})\dot{\eta}(t-N) \\ &+ K^{-1}(I_{n_m} - \cos(\sqrt{K}\bar{\tau}))Rq,\end{aligned} \tag{4.19}$$

where $\bar{\tau} = N - \tau$, $q = P\hat{\mathbf{M}} - Q\mathbf{M_2}$, and $\hat{\mathbf{M}} = 2\mathbf{M_1}x_r + \mathbf{M_3}$. As a result,

$$\begin{aligned} d\bar{\mathcal{G}}_{\text{aux}} &= \begin{bmatrix} \mathbf{h}_{\text{aux}} \\ L_{\mathbf{f}_0}\mathbf{h}_{\text{aux}} \\ L_{\mathbf{f}_0}^2\mathbf{h}_{\text{aux}} \\ L_{\mathbf{f}_0}^3\mathbf{h}_{\text{aux}} \\ L_{\mathbf{f}_0}^4\mathbf{h}_{\text{aux}} \end{bmatrix} \\ &= \begin{bmatrix} \cos(\sqrt{K}\bar{\tau}) & K^{-1/2}\sin(\sqrt{K}\bar{\tau}) & G_{(1,3)} & G_{(1,4)} & -K^{-1}(\cos(\sqrt{K}\bar{\tau}) - I_{n_m})q \\ -K^{1/2}\sin(\sqrt{K}\bar{\tau}) & \cos(\sqrt{K}\bar{\tau}) & G_{(2,3)} & G_{(2,4)} & K^{-1/2}\sin(\sqrt{K}\bar{\tau})q \\ -K\cos(\sqrt{K}\bar{\tau}) & -K^{1/2}\sin(\sqrt{K}\bar{\tau}) & G_{(3,3)} & G_{(3,4)} & \cos(\sqrt{K}\bar{\tau})q \\ K^{3/2}\sin(\sqrt{K}\bar{\tau}) & -K\cos(\sqrt{K}\bar{\tau}) & G_{(4,3)} & G_{(4,4)} & -K^{1/2}\sin(\sqrt{K}\bar{\tau})q \\ K^2\cos(\sqrt{K}\bar{\tau}) & K^{3/2}\sin(\sqrt{K}\bar{\tau}) & G_{(5,3)} & G_{(5,4)} & -K\cos(\sqrt{K}\bar{\tau})q \end{bmatrix}, \end{aligned} \tag{4.20}$$

where the third and fourth columns are given in Appendix A due to space considerations. The third, fourth and fifth columns are linearly dependent, and $d\bar{\mathcal{G}}_{\text{aux}}$ is rank-deficient by one. Hence, $d\bar{\mathcal{G}}$ is also rank-deficient by at least one, and the system with delay (2.3) is unobservable when $\mathbf{u} = \mathbf{0}$.

4.2 Observability Analysis of Systems with a Composite Output Function

In this section, we present theoretical results on the observability of systems with an output having the structure of function composition of the form, $g \circ h$. Our first main results is that if a system

$$\Sigma_h : \quad \begin{aligned} \dot{\mathbf{x}}(t) &= \mathbf{f_0}(\mathbf{x}(t)) \\ y(t) &= h(\mathbf{x}(t)), \end{aligned} \tag{4.21}$$

is unobservable, then the system

$$\Sigma_{g\circ h} : \quad \begin{aligned} \dot{\mathbf{x}}(t) &= \mathbf{f_0}(\mathbf{x}(t)) \\ y(t) &= (g \circ h)(\mathbf{x}(t)), \end{aligned} \tag{4.22}$$

is also unobservable for any function g. Applying a function g to the output of an unobservable system thus cannot make the unobservable system observable. Our second main result is that $\Sigma_{g\circ h}$ can be unobservable, even if Σ_h is observable. When applying a function g to the output of Σ_h leads to an unobservable system $\Sigma_{g\circ h}$, we term the combination of Σ_h and g a singular case. One should avoid singular cases whenever possible. For the remainder of this section, we consider cases in which g and h have the same output-space dimension.

4.2.1 Observability Space for Systems with a Composite Output Function

We first consider a control-free nonlinear system Σ_h with a single output, i.e., $\mathbf{f_0} : \mathbb{R}^n \to \mathbb{R}^n$ and $h : \mathbb{R}^n \to \mathbb{R}$. We also consider another system $\Sigma_{g\circ h}$, which has the same internal dynamics as the first system but uses a function composition $g\circ h$ as output, where $g : \mathbb{R} \to \mathbb{R}$.

The two systems have the respective observation spaces

$$\mathcal{G}_h = \operatorname{span}\{L_{\mathbf{f_0}}^{n-1} h, \ldots, L_{\mathbf{f_0}} h, h\} \tag{4.23}$$

$$\mathcal{G}_{g\circ h} = \operatorname{span}\{L_{\mathbf{f_0}}^{n-1}(g \circ h), \ldots, L_{\mathbf{f_0}}(g \circ h), g \circ h\}. \tag{4.24}$$

Using the gradient operator, ∇, where

$$\nabla\phi := \begin{pmatrix} \frac{\partial \phi}{\partial x_1} & \frac{\partial \phi}{\partial x_2} & \cdots & \frac{\partial \phi}{\partial x_n} \end{pmatrix}^\top, \tag{4.25}$$

one can obtain the Jacobian matrices

$$d\mathcal{G}_h = \begin{bmatrix} \nabla h & \nabla L_{\mathbf{f_0}} h & \cdots & \nabla L_{\mathbf{f_0}}^{n-1} h \end{bmatrix}^\top, \tag{4.26}$$

$$d\mathcal{G}_{g\circ h} = \begin{bmatrix} \nabla (g\circ h) & \nabla L_{\mathbf{f_0}} (g\circ h) & \cdots & \nabla L_{\mathbf{f_0}}^{n-1} (g\circ h) \end{bmatrix}^\top, \tag{4.27}$$

of the observation spaces. Each of the Jacobian matrices has full rank if and only if the corresponding system is observable. We thus call $d\mathcal{G}_h$ and $d\mathcal{G}_{g\circ h}$ the *observability matrices* of Σ_h and $\Sigma_{g\circ h}$, respectively.

4.2.2 Higher-order Lie Derivatives of Composite Functions

To be able to relate the observability of $\Sigma_{g\circ h}$ to Σ_h, we are interested in the determinant of the two observability matrices $d\mathcal{G}_{g\circ h}$ and $d\mathcal{G}_h$. We start with deriving an expression for $L_{\mathbf{f_0}}^k (g\circ h)$ which appears in Eq. (4.24), and its gradient appears in Eq. (4.27) where k is a positive integer.

Theorem 5 *The k-th Lie derivative of a composition $g\circ h$ with respect to $\mathbf{x}$ on a vector field $\mathbf{f}$ is*

$$L_{\mathbf{f}}^k (g\circ h) = \sum_{j=1}^{k} \left[(g^{(j)} \circ h) \sum_{s\in M_{k,j}} \left(\prod_{s_i \in s} L_{\mathbf{f}}^{s_i} h \right) \right], \tag{4.28}$$

where $g^{(j)} \circ h$ denotes the j-th derivative of g with respect to h and $M_{k,j}$ is a multiset of ordered multisets of integers with the recursive construction rule

$$M_{k,j} := \begin{cases} \{s\backslash\{s_i\} \cup \{s_{i+1}\} \mid s_i \in s,\ s\in M_{k-1,j}\} \cup \{s \cup \{1\} \mid s \in M_{k-1,j-1}\} & \textit{if } k > j > 0, \\ \emptyset & \textit{otherwise.} \end{cases} \tag{4.29}$$

Proof See Appendix B. ■

Corollary 2 *The gradient of the k-th Lie derivative of a composition $g \circ h$ is*

$$\begin{aligned}\nabla L_{\mathbf{f}}^{k}(g \circ h) = \sum_{j=1}^{k} \Bigg\{ &(g^{(j+1)} \circ h)\nabla h \sum_{s \in M_{k,j}} \left[\prod_{s_i \in s} L_{\mathbf{f}}^{s_i} h \right] \\ &+ (g^{(j)} \circ h) \sum_{s \in M_{k,j}} \sum_{s_\ell \in s} \left[\nabla \left(L_{\mathbf{f}}^{s_\ell} h \right) \prod_{\substack{s_i \in s, \\ i \neq \ell}} L_{\mathbf{f}}^{s_i} h \right] \Bigg\} .\end{aligned} \tag{4.30}$$

Proof We apply the product rule for derivatives to Eq. (4.28) and obtain

$$\nabla L_{\mathbf{f}}^{k}(g \circ h) = \sum_{j=1}^{k} \left\{ (g^{(j+1)} \circ h)\nabla h \sum_{s \in M_{k,j}} \left[\prod_{s_i \in s} L_{\mathbf{f}}^{s_i} h \right] + (g^{(j)} \circ h) \sum_{s \in M_{k,j}} \left[\nabla \prod_{s_i \in s} L_{\mathbf{f}}^{s_i} h \right] \right\} . \tag{4.31}$$

Applying the product rule again to the second term in Eq. (4.31) yields Eq. (4.30). ■

Also, see Appendix C for our conjecture on another expression of $\nabla L_{\mathbf{f}}^{k}(g \circ h)$.

4.2.3 Observability of Systems with a Composite Output Function

We are now ready to present the main result of this section by relating $d\mathcal{G}_h$ and $d\mathcal{G}_{g\circ h}$ using Cor. 2.

Theorem 6 *Given systems Σ_h in (32) and $\Sigma_{g\circ h}$ in (33), define the observation spaces $\mathcal{G}_h = \operatorname{span}\{L_{\mathbf{f}_0}^{n-1} h, \ldots, L_{\mathbf{f}_0} h, h\}$ and $\mathcal{G}_{g\circ h} = \operatorname{span}\{L_{\mathbf{f}_0}^{n-1}(g \circ h), \ldots, L_{\mathbf{f}_0}(g \circ h), g \circ h\}$ where $\mathbf{f}_0 : \mathbb{R}^n \to \mathbb{R}^n$, $h : \mathbb{R}^n \to \mathbb{R}$, and $g : \mathbb{R} \to \mathbb{R}$. Then, the Jacobian matrices of $\mathcal{G}_1$ and $\mathcal{G}_2$ are related with the expression*

$$\det d\mathcal{G}_{g\circ h} = \left(\frac{dg}{dh} \right)^{n} \det d\mathcal{G}_h . \tag{4.32}$$

Proof Using (4.30), it can be written that

$$\mathcal{G}_{g\circ h} = \begin{bmatrix} (g^{(1)}\circ h)\nabla^\top h \\ \left\{(g^{(2)}\circ h)\nabla h \displaystyle\sum_{s\in M_{1,1}} \left[\prod_{s_i\in s} L_{\mathbf{f_0}}^{s_i} h\right] + (g^{(1)}\circ h)\sum_{s\in M_{1,1}}\sum_{s_\ell\in s}\left[\nabla\left(L_{\mathbf{f_0}}^{s_\ell}h\right)\prod_{\substack{s_i\in s\\ i\neq \ell}} L_{\mathbf{f_0}}^{s_i}h\right]\right\}^\top \\ \vdots \\ \sum_{j=1}^{n-1}\left\{(g^{(j+1)}\circ h)\nabla h \displaystyle\sum_{s\in M_{n-1,j}} \left[\prod_{s_i\in s} L_{\mathbf{f_0}}^{s_i} h\right] + (g^{(j)}\circ h)\sum_{s\in M_{n-1,j}}\sum_{s_\ell\in s}\left[\nabla L_{\mathbf{f_0}}^{s_\ell}h\prod_{\substack{s_i\in s\\ i\neq \ell}} L_{\mathbf{f_0}}^{s_i}h\right]\right\}^\top \end{bmatrix}.$$

Since we are interested in the determinant of the Jacobian matrix, $\mathcal{G}_{g\circ h}$, we are able to use the Gaussian elimination algorithm and obtain

$$\begin{aligned} \det\mathcal{G}_{g\circ h} &= \left|(g'\circ h)\nabla h \quad (g'\circ h)\nabla L_{\mathbf{f_0}}h \quad \cdots \quad (g'\circ h)\nabla L_{\mathbf{f_0}}^{n-1}h\right| \\ &= (g'\circ h)^n\left|\nabla h \quad \nabla L_{\mathbf{f_0}}h \quad \cdots \quad \nabla L_{\mathbf{f_0}}^{n-1}h\right| \\ &= \left(\frac{dg}{dh}\right)^n \det\mathcal{G}_h, \end{aligned}$$

which completes the proof. ■

We draw two implications from Theorem 6:

1. If the nonlinear system Σ_h is unobservable, then the system $\Sigma_{g\circ h}$ with the same internal dynamics and composite output function $g\circ h$ is also unobservable.

2. Observable systems Σ_h lead to observable systems $\Sigma_{g\circ h}$ if and only if dg/dh is non-zero.

The function g serves the role of a spatial notch filter when $dg/dh = 0$. This result also allows us to comment on the effect of g on observability even if it is not possible to analytically study expressions like ∇h. The examples given in the subsection below illustrate these aspects.

The observability analysis of controlled nonlinear systems requires calculating Lie derivatives with respect to x on the control fields since the separation principle does not hold as shown in Sec. 3.1. The extension of the result presented for control-free systems to single- or multi-input systems requires an expression for $\nabla L_{\mathbf{f_0}}^{n-1} L_{\mathbf{f_i}}^{n-1}(g \circ h)$ similar to the one we obtained in Corollary 2. We anticipate that the requirements for the observability of a system with a composite output function are the same for control-free systems and for single- or multiple-input systems with one difference: The observability matrix will not be square. Similarly, we would not have a square observability matrix for a system with multiple outputs. Finally, one can construct the observability matrix for a multiple-input-single-output system using directly the Lie derivatives on the vector field $\mathbf{f}$ [56], i.e.,

$$d\mathcal{G}_{g\circ h} = \begin{bmatrix} \nabla(g \circ h) & \nabla L_{\mathbf{f}}(g \circ h) & \cdots & \nabla L_{\mathbf{f}}^{n-1}(g \circ h) \end{bmatrix}^{\top} . \tag{4.33}$$

In that case, the current results would be sufficient to comment on the observability of $\Sigma_{g\circ h}$

4.2.4 Example Systems

In this section, we present two examples to illustrate the results from above for systems with an output function in the form of function composition.

Double Integrator Dynamics with a Saturated Output

First, consider the dynamics of a double integrator with an unsaturated output:

$$\Sigma_h : \quad \begin{aligned} \dot{\mathbf{x}}(t) &= \begin{bmatrix} 0 & 1 \\ 0 & 0 \end{bmatrix} \mathbf{x}(t) \\ y(t) &= \begin{bmatrix} 1 & 0 \end{bmatrix} \mathbf{x}(t). \end{aligned} \tag{4.34}$$

Since the system is linear, the observability matrix can be easily written as $d\mathcal{G}_h = \mathrm{diag}\,(1, 1)$ which is full rank, that is, the system (4.34) observable.

Now consider the same system dynamics with a saturated output:

$$\Sigma_{g\circ h}: \quad \begin{aligned} \dot{\mathbf{x}}(t) &= \begin{bmatrix} 0 & 1 \\ 0 & 0 \end{bmatrix} \mathbf{x}(t) \\ y(t) &= \tanh\left(\begin{bmatrix} 1 & 0 \end{bmatrix} \mathbf{x}(t)\right), \end{aligned} \tag{4.35}$$

where the hyperbolic tangent function, which is infinitely differentiable, creates the saturation effect (Fig. 4.1a). Since $d\mathcal{G}_h$ is full rank, by the help of Theorem 6, one can state that the system is observable for $[d(\tanh x_1)/dx_1]^2 = \operatorname{sech}^4 x_1 \neq 0$. Indeed, the observation space of the system (4.35) is $\mathcal{G}_{g\circ h} = \operatorname{span}\{L_{\mathbf{f}_0}(\tanh x_1), \tanh x_1\}$, where $\mathbf{f_0} = \begin{bmatrix} x_2 & 0 \end{bmatrix}^\top$, and the nonlinear observability matrix can be written as:

$$d\mathcal{G}_{g\circ h} = \begin{bmatrix} \frac{\partial \tanh x_1}{\partial x_1} & \frac{\partial \tanh x_1}{\partial x_2} \\ \frac{\partial (x_2 \operatorname{sech}^2 x_1)}{\partial x_1} & \frac{\partial (x_2 \operatorname{sech}^2 x_1)}{\partial x_2} \end{bmatrix} = \begin{bmatrix} \operatorname{sech}^2 x_1 & 0 \\ -2x_2 \operatorname{sech}^2(x_1)\tanh(x_2) & \operatorname{sech}^2 x_1 \end{bmatrix},$$

which is full rank for $\det d\mathcal{G}_{g\circ h} = \operatorname{sech}^4 x_1 \neq 0$.

When the derivative of $\tanh x_1$ is practically zero, the initial state becomes indistinguishable in its neighborhood. Similarly, when the slope is steep, it is easier to distinguish neighboring initial states, that is, when the derivative is large, we get higher output sensitivity as well as higher observability metrics such as the n-th root of the determinant of the observability Gramian. Finally, note that using a rectified hyperbolic tangent function is an alternative way to express the activation function in the neural encoding process [4].

NLA Parameters Selection

Recall the nonlinear activation function on the projected stimulus, ξ, in the neural encoding process which gives the probability of firing of a neuron and is considered as the output of the system:

$$\mathrm{NLA}(\xi) = \frac{1}{1 + \exp(-c(\xi - d))}.$$

We are interested in the parameters of NLA, c and d, and desire them not to make the system unobservable assuming that it is observable when the output is $y(t) = \xi(t)$. Here, the role of the NLA function on ξ is the same as g on h in (4.22), and its derivative with respect to ξ is

$$\frac{\mathrm{d}\,\mathrm{NLA}(\xi)}{\mathrm{d}\,\xi} = \frac{c\exp(-c(\xi - d))}{(\exp(-c(\xi - d)) + 1)^2}. \tag{4.36}$$

If there is no slope ($c = 0$), the NLA function makes the system unobservable. Also, the derivative, and hence the output sensitivity, is expected to be higher about the axis $\xi = d$. In Fig. 4.1b, two NLA functions and derivatives are plotted. One can imply that the first set of NLA parameters would serve better to observe the system when $\xi < 0$ and the second is good to use when ξ is positive. Finally, note that due to the relation (4.32), we are able to assess the observability, even though the functional structure does not allow us to study it analytically.

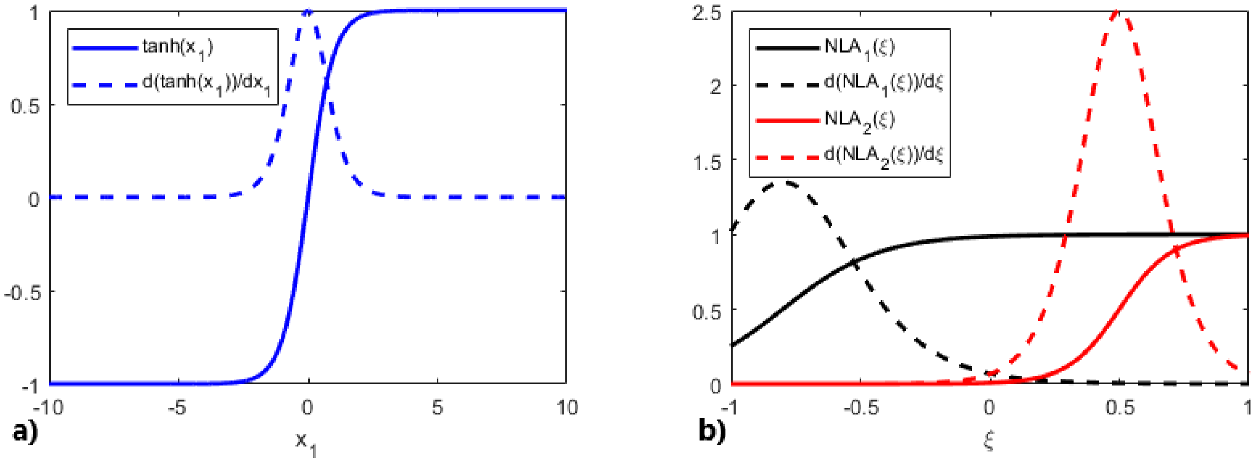

Figure 4.1: The outer functions and their derivatives appeared in a) the first and b) second examples. Here, $\mathrm{NLA}(\xi) = 1/1 + \exp(-5.4(\xi + 0.8))$ **and** $\mathrm{NLA}(\xi) = 1/1 + \exp(-10(\xi - 0.5))$**.**

4.3 Numerical Application: Hawkmoth Flapping Wing

In this section, we address some applications of interest with respect to biological sensing in the hawkmoth. Due to the complexity of the wing model dynamics and unavailable function derivatives, the empirical Gramian is used instead of the analytical Gramian. After the numerical observability analysis, we optimally solve the problem of neural-inspired sensor placement for the hawkmoth flapping wing model using two sensor types. Second, we present the effect of STA and NLA parameters on the observability of flapping wing dynamics using a metric based on the empirical Gramian and compare the results with the ones that come from the derivative analysis in the previous section.

4.3.1 System Simulations

In order to implement the empirical Gramian, system simulations must be set up. The simulation of the full dynamics of a *Manduca sexta* wing requires several components. First, the wing stroke kinematics, the effective inputs to the system, $\mathbf{u}$, are controlled by three Euler angles which provide the nominal input sequence. The planform geometry of the wing is based on photographs of a hawkmoth forewing from [7] and is scaled for a 50 mm wingspan. Finally, the wing structural mode shapes and frequencies and the wing mass density and thickness are taken from [37].

The following stroke kinematics were used to define a nominal flapping cycle:

$$\theta(t) = 0 \tag{4.37}$$

$$\psi(t) = -A_\psi \cos(2\pi t/T_{\text{beat}}) \tag{4.38}$$

$$\alpha(t) = \frac{\pi}{2} - A_\alpha \tanh\left(\frac{\pi}{2}\sin(2\pi t/T_{\text{beat}})\right). \tag{4.39}$$

Here, the stroke position amplitude, A_ψ, and the feathering angle amplitude, A_α, are taken as 45° and 60, respectively, and the wing-beat period, T_{beat}, is 40 ms. The simulation time is $2T_{\text{beat}}$, where the first period is used to provide the stimulus history required for the filter. The trajectory is perturbed at the beginning of the second period, and the empirical observability Gramian is calculated for that second period, that is, t_1 in Eq. (3.10) is chosen to be T_{beat}.

The STA and NLA parameters were selected based on values derived in [10] using electrophysiological recordings of mechanoreceptors in *Manduca sexta* [9]. The values are taken to be $a = 5\,\text{ms}$, $b = 4\,\text{ms}$, $\omega_{\text{STA}} = 1000\,\text{rad}\,\text{s}^{-1}$, $c = 10$, $d = 0.5$, and $N = 40\,\text{ms}$. Finally, to obtain C_ξ, the trajectory was simulated for two periods. The maximum absolute value of non-normalized ξ over all sensors and the complete second period, 0.1174, was picked as C_ξ.

In order to account for variations in observability due to sensor location, the surface of the wing was discretized into a 51 × 21-station grid, and the empirical observability Gramian was computed for each sensor location on the grid. Sensor measurements were taken to encode the bending strain, ϵ_{yy}, and the shear strain, ϵ_{xy}. The perturbation value for the initial conditions was selected as $\varepsilon = 0.001$.

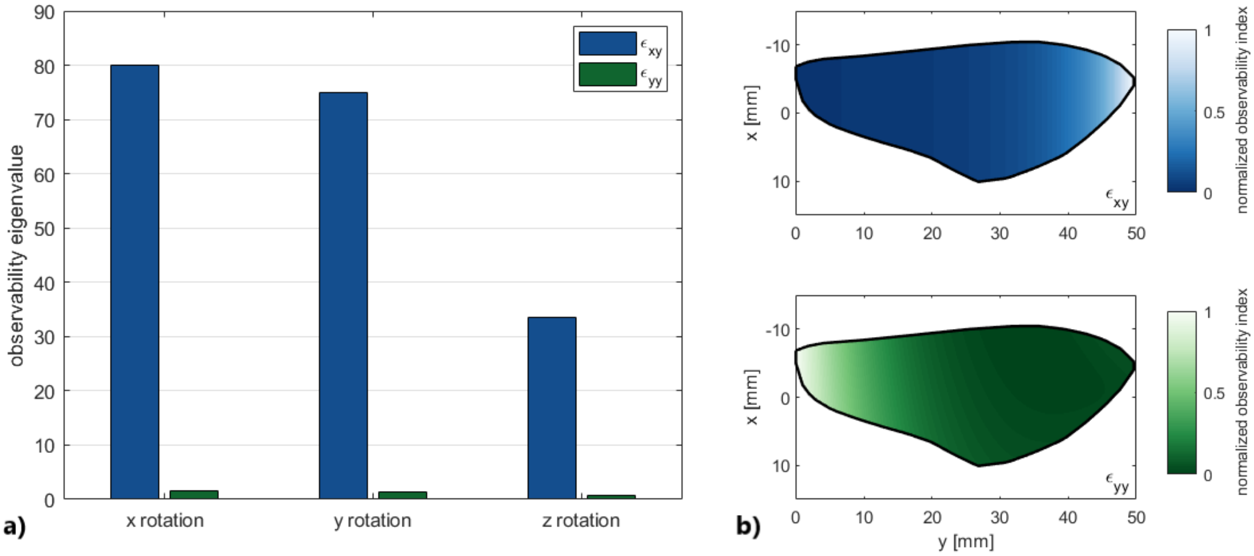

Figure 4.2: a) Spatially averaged empirical observability Gramian eigenvalues for rotation about the three body axes using either neural-encoded shear strain, ϵ_{xy}, or bending strain, ϵ_{yy}. b) Observability index throughout the wing for shear (*top*) and bending (*bottom*) strain encoding, normalized individually for each sensor type.

The spatially averaged observability eigenvalues for independent rotations about body-fixed axes are given in Fig. 4.2a. For both shear and bending sensing, the most observable mode was the rotation about the x-axis while the rotation about the z-axis was the least observable mode. Although the shear strain measurements resulted in relatively large eigenvalues of the empirical observability Gramian, the eigenvalues from bending strain measurements were more balanced with an average condition number of 1.9 for bending while it was 3.0 for shear. The empirical observability Gramian was also utilized to study the observability of the hawkmoth using just the raw strain information, and the condition numbers of the matrix were reported in [37] to be 1.2 for bending and 1.3 for shear. Neural encoding negatively affected the balance of eigenvalues in strain measurements but kept them within acceptable levels.

The observability index values, or simply the minimum observability eigenvalues, for bending and shear stress measurements were obtained and normalized separately. The results given in Fig. 4.2b are consistent with the delay-free case as reported in [37]. In other words, the dynamics with shear strain measurements were more observable at the wing tip while the observability index was the highest at the wing root for span-wise bending. It should also be noted that the minimum observability indices after the normalization by the maximum index of each sensor type were 2.98×10^{-2} and 3.99×10^{-5} for shear and bending strains, respectively, whereas they were 2.50×10^{-1} and 5.36×10^{-5} in the delay-free case [37] showing that neural encoding adds some balance to the ϵ_{xy}-based observability index distribution across the wing while its contribution is in the negative for the distribution of ϵ_{yy}-based observability index.

Finally, the approximate lower bounds for the minimum singular values of the empirical Gramian were calculated for all sensor locations following the numerical methodology described in Sec. 3.2, and it was confirmed that all the minimum eigenvalues were above the approximated lower bounds. It was also observed that the lower bounds were greatest where the rotation rates were most observable and were smallest where the rates were least observable.

4.3.2 Optimal Sensor Placement

A key point about the observability of the body rotation rates is that the results are not uniform across the wing of the hawkmoth; the location of the sensors has a large effect on the observability result. Two fundamental questions can then be addressed relative to neural encoding in sensing: (1) optimal sensor placement from an engineering perspective to determine system design, and (2) assessment of sensor functionality in biological systems. To address the first point, a sensor placement problem can be designed to obtain an optimal configuration in terms of the sensor type (shear or bending via neural encoding) and location. With respect to the second question, possible sensor locations can be restricted to being on one of the wing veins in the hawkmoth to correspond to viable physical locations on the actual animal [7]. In either case, a set of possible sensor locations on the veins was formed by spacing them 2 mm apart along each vein, and the empirical Gramian was computed at those locations using the same parameters in the observability analysis above.

To set up the sensor selection framework, note that the sum of the Gramians corresponding to each sensor in a set being used individually gives the observability Gramian for all sensors in the set being used simultaneously, i.e.,

$$W_o^\varepsilon(\boldsymbol{\gamma}) = \sum_{i=1}^{p} \gamma_i (W_o^\varepsilon)_i, \tag{4.40}$$

where $\boldsymbol{\gamma}_i \in \{0, 1\}$ is a sensor activation function indicating whether a given sensor is in use, and p is the number of sensors in the set. By relaxing the sensor activation constraint to a linear inequality constraint, an observability-based optimal sensor placement problem can be posed as

$$\begin{aligned} \min_{\gamma} \quad & \kappa(W_o^\varepsilon(\gamma)) + w_\nu \nu(W_o^\varepsilon(\gamma)) \\ \text{subject to} \quad & 0 \leq \boldsymbol{\gamma} \leq 1 \\ & \sum \boldsymbol{\gamma} = r, \end{aligned} \tag{4.41}$$

where $r \leq p$ is the desired number of sensors to place on the wing, and $w_\nu \geq 0$ is the weight. (A formulation to minimize the condition number of a positive-definite matrix is given in [57].) Such a relaxation would perform better than the mixed integer programming approach for large problems (with high number of possible sensor locations, p) [58]. To solve this convex optimization problem, we used CVX, a package for specifying and solving convex programs [59, 60]. The resultant sensor location and types for $r = 20$ and $w_\nu = 20$ are given in Fig. 4.3 along with physical campaniform sensilla locations.

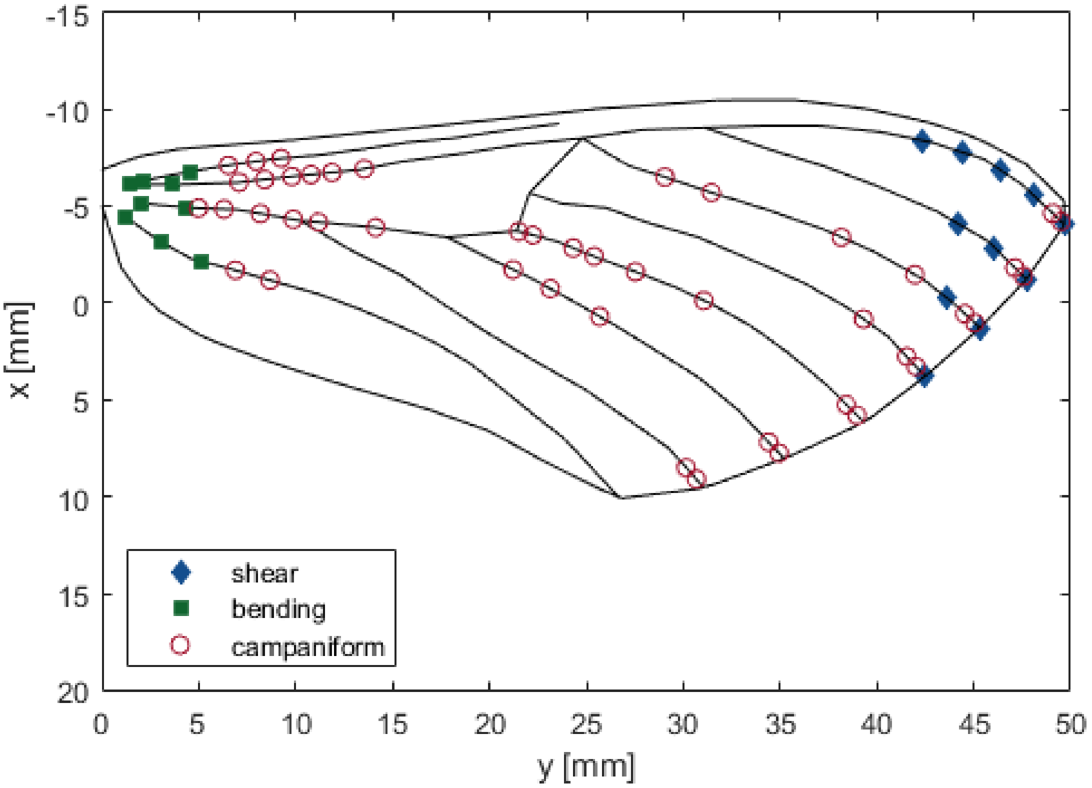

Figure 4.3: Optimal sensor set compared to locations of campaniform sensilla found on a hawkmoth forewing in [7]. The clusters of campaniform sensilla located at the wing root near the wing hinge are not shown.

Two clusters of sensors are obtained from the numerical optimization while there are three clusters of campaniform sensilla on the actual insects. The sensors are gathered where the ϵ_{xy}- and ϵ_{yy}-based observability indices are maximum. The results here have a similar pattern to the sensor locations found for the raw measurements in [37] which is to be expected as their observability index behaviors across the wing are parallel.

4.3.3 Varying STA and NLA Functions

In order to further explore the effects of neural-inspired sensing with delay, we tested different STA and NLA functions from [10]. To be consistent with that work, we only studied the observability via neural encoding of the bending strain, ϵ_{yy}. This application was based on the fact that there is no evidence that campaniform sensilla are able to detect shear strain.

STA Functions

The values of the tested STA parameters, b in milliseconds and ω_{STA} in radians per second, ranged from 0.1 to 20 and from zero to 2×10^3, respectively. The delay, a, was kept constant at 5 ms. Since different STA functions require different normalization constants, C_ξ, the process described above was followed for 121 combinations. Note that the values of C_ξ are highly correlated ($\rho = 0.9491$) with the integral $\int_0^N STA(\tau)d\tau$. The same NLA parameters were used in this stage.

Figure 4.4 illustrates two spatially averaged observability metrics for varying STA parameters, width and frequency. The results shown in the red box correspond to the experimentally derived STA and outperform other STA functions with the same frequency, $\omega_{\text{STA}} = 1000\,\text{rad}\,\text{s}^{-1}$.

NLA Functions

The resultant distribution of the time-averaged projected stimulus, ξ, on the wing is given in Fig. 4.5a. The spatiotemporal mean value is 1.61×10^{-4}. The values of the tested NLA parameters, c and d, ranged from 1 to 29 and -1 to 1, respectively, while the STA parameters duplicated the ones above. Since we were able to relate determinants of observability matrices in Sec. 4.2, we chose the n-th root of the determinant, $[\det(W_o^\varepsilon)]^{1/n}$ as the observability

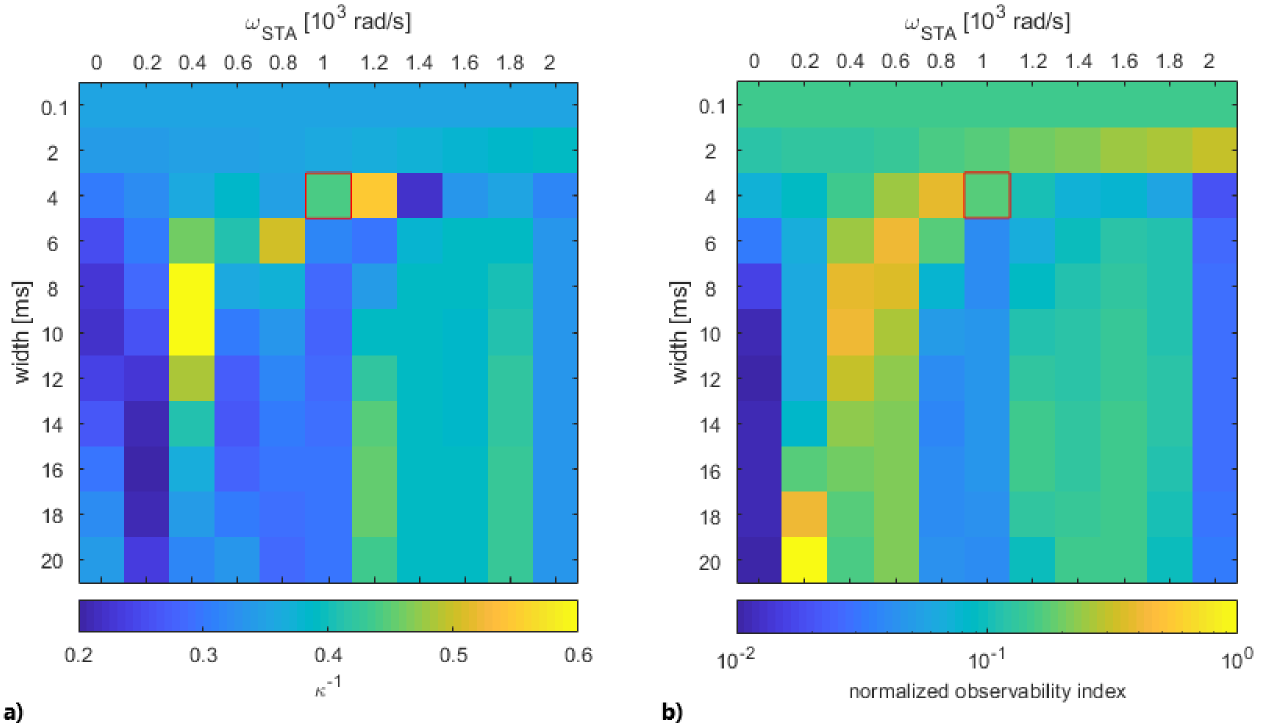

Figure 4.4: The two observability metrics obtained from neural-encoded bending strain data with varying STA parameters and presented as heat maps.

metric.

Figure 4.5b illustrates spatially-averaged value of $[\det(W_o^\varepsilon)]^{1/n}$, for varying slope parameter and half-max values. The rotation rates were most observable when $d = 0$, and the observability decreased as the half-max moved away from zero. The slope parameter, c, also affects the observability: As c increases, the average determinant value decreases except the case when $d = 0$.

Theorem 6 and the relation of the linear observability matrix and the linear observability Gramian [61] also led us to investigate the relation between $[\det(W_o^\varepsilon)]^{1/n}$ and $(\mathrm{d}\,\mathrm{NLA}(\xi)/\mathrm{d}\,\xi)^2$. We observed that they are highly correlated ($\rho = 0.9978$) for the 132 NLA parameter combinations, which supports the anticipated relation of output sensitivity and the derivative of composing function, g. The empirical observability Gramian of a system with a composite output function will be further discussed in the following section.

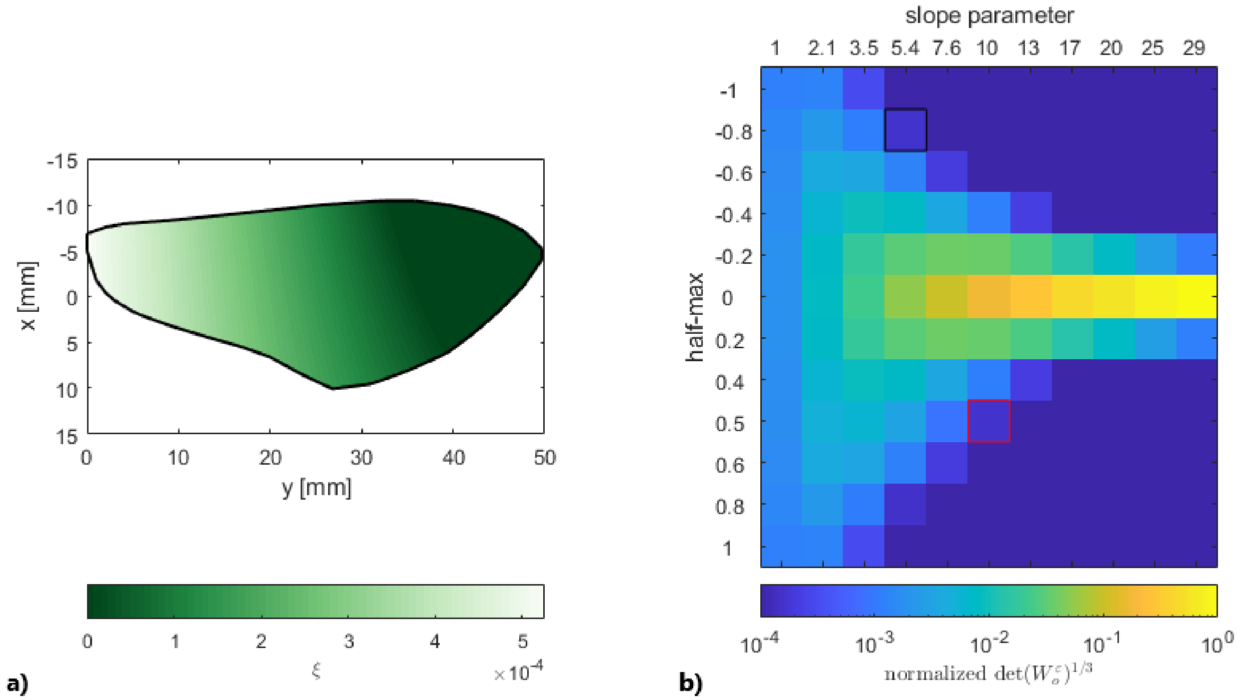

Figure 4.5: a) The time-averaged projected stimulus (ξ) throughout the wing. b) The change of the spatially-averaged value of $[\det(W_o^\varepsilon)]^{1/3}$ by the two NLA parameters. The black and red boxes correspond to the functions given in Fig. 4.1b. The parameters corresponding to the red box are also the ones derived experimentally.

4.4 Discussion on the Empirical Observability Gramian

The relation for discrete-time linear systems given in [61], $W_o = \mathcal{O}_n^\top \mathcal{O}_n$, and the numerical results from the last section motivated us to study the relation of the empirical observability Gramians of systems Σ_h and Σ_{goh}.

Let the empirical observability Gramians corresponding to the systems Σ_h and Σ_{goh} be W_h^ε and W_{goh}^ε, respectively. In [1], using the central definition of the derivative and Lebesgue's dominated convergence theorem, it was shown that

$$\lim_{\varepsilon \to 0} W_h^\varepsilon(t_1, \mathbf{x}_0, \mathbf{u}) = \int_0^{t_1} \frac{\partial y}{\partial \mathbf{x}_0}^\top \frac{\partial y}{\partial \mathbf{x}_0} dt, \tag{4.42}$$

where the explicit dependence of the derivative on t, $\mathbf{x}_0$, and $\mathbf{u}$ is dropped for the sake of brevity. We will also use this result instead of the Fréchet-Taylor expansion of $W_o^\varepsilon(t_1, \mathbf{x}_0, \mathbf{u})$ and write

$$\begin{aligned}\lim_{\varepsilon\to 0} W_{g\circ h}^{\varepsilon}\left(t_1, \mathbf{x}_0, \mathbf{u}\right) &= \int_0^{t_1} \left(\partial_{\mathbf{x}_0}(g\circ h)\right)^\top \partial_{\mathbf{x}_0}(g\circ h)dt \\ &= \int_0^{t_1} \left[(g'\circ h)\partial_{\mathbf{x}_0}h\right]^\top \left[g'\circ h\right]\partial_{\mathbf{x}_0}h dt,\end{aligned} \tag{4.43}$$

where g' denotes the derivative of g with respect to h. Since we have a single output, one can drop the transpose and rearrange the terms as:

$$\lim_{\varepsilon\to 0} W_{g\circ h}^{\varepsilon}\left(t_1, \mathbf{x}_0, \mathbf{u}\right) = \int_0^{t_1} \left(g'\circ h\right)^2 \left(\partial_{\mathbf{x}_0}h\right)^2 dt. \tag{4.44}$$

Integration by parts leads us to

$$\lim_{\varepsilon\to 0} W_{g\circ h}^{\varepsilon}\left(t_1, \mathbf{x}_0, \mathbf{u}\right) = \left|\left(g'\circ h\right)^2 \int \left(\partial_{\mathbf{x}_0}h\right)^2 dt\right|_0^{t_1} - \int_0^{t_1} \partial_t\left(g'\circ h\right)^2 \left(\int \left(\partial_{\mathbf{x}_0}h\right)^2 dt'\right) dt. \tag{4.45}$$

Let us define

$$a\left(\mathbf{x}_0, t\right) = \left(g'\circ h\right)^2, \tag{4.46a}$$

$$b\left(\mathbf{x}_0, t\right) = \int \left(\partial_{\mathbf{x}_0}h\right)^2 dt, \tag{4.46b}$$

and note that

$$\lim_{\varepsilon\to 0} W_h^{\varepsilon}\left(t_1, \mathbf{x}_0, \mathbf{u}\right) = b\left(\mathbf{x}_0, t_1\right) - b\left(\mathbf{x}_0, 0\right). \tag{4.47}$$

Then Eq. (4.45) can be written as:

$$\begin{aligned}\lim_{\varepsilon\to 0} W^{\varepsilon}_{g\circ h}\left(t_1,\mathbf{x}_0,\mathbf{u}\right) =& |ab|_0^{t_1} - \int_0^{t_1} \partial_t(a) b dt \\ =& a\left(\mathbf{x}_0,t_1\right) b\left(\mathbf{x}_0,t_1\right) - a\left(\mathbf{x}_0,0\right) b\left(\mathbf{x}_0,0\right) - \int_0^{t_1} \partial_t(a) b dt \\ =& a\left(\mathbf{x}_0,t_1\right)\left[b\left(\mathbf{x}_0,t_1\right) - b\left(\mathbf{x}_0,0\right)\right] + \left[a\left(\mathbf{x}_0,t_1\right) - a\left(\mathbf{x}_0,0\right)\right] b\left(\mathbf{x}_0,0\right) \\ & - \int_0^{t_1} \partial_t(a) b dt \\ =& a\left(\mathbf{x}_0,t_1\right)\left[b\left(\mathbf{x}_0,t_1\right) - b\left(\mathbf{x}_0,0\right)\right] + b\left(\mathbf{x}_0,0\right)\int_0^{t_1} \partial_t(a) dt - \int_0^{t_1} \partial_t(a) b dt.\end{aligned}$$

Finally, we have the relation

$$\lim_{\varepsilon\to 0} W^{\varepsilon}_{g\circ h}\left(t_1,\mathbf{x}_0,\mathbf{u}\right) = \left(g'\circ h\right)^2 \lim_{\varepsilon\to 0} W^{\varepsilon}_{h}\left(t_1,\mathbf{x}_0,\mathbf{u}\right) + b\left(\mathbf{x}_0,0\right)\int_0^{t_1} \partial_t(a) dt - \int_0^{t_1} \partial_t(a) b dt. \tag{4.48}$$

Two independent conditions guarantee the cancellation of the second and third terms in Eq. (4.48) are $\partial_t a = 0$ and $b(\mathbf{x}_0,t) = b(\mathbf{x}_0,0)$. However, in general, the cancellation cannot be assumed, and it can be concluded that

$$\lim_{\varepsilon\to 0} W^{\varepsilon}_{g\circ h}\left(t_1,\mathbf{x}_0,\mathbf{u}\right) \approx \left(g'\circ h\right)^2 \lim_{\varepsilon\to 0} W^{\varepsilon}_{h}\left(t_1,\mathbf{x}_0,\mathbf{u}\right),$$

if and only if

$$\left(g'\circ h\right)^2 \lim_{\varepsilon\to 0} W^{\varepsilon}_{h}\left(t_1,\mathbf{x}_0,\mathbf{u}\right) \gg b\left(\mathbf{x}_0,0\right)\int_0^{t_1} \partial_t(a) dt - \int_0^{t_1} \partial_t(a) b dt,$$

which can be numerically studied as we did in the previous section while analyzing the correlation of $[\det(W^{\varepsilon}_{o})]^{1/n}$ and $(\mathrm{d}\,\mathrm{NLA}(\xi)/\mathrm{d}\,\xi)^2$.

Chapter 5

OPTIMAL SENSOR PLACEMENT USING STOCHASTIC EMPIRICAL GRAMIAN

In this chapter, we first define the empirical observability Gramian for stochastic observability of nonlinear systems, then pose an optimal sensor placement problem using metrics based on the stochastic empirical Gramian. At the end of the chapter, we will be able to comment on the observability of systems with neural-inspired measurements in the presence of noise.

5.1 Stochastic Empirical Gramian

Consider the nonlinear system with noise,

$$\Sigma_{\text{NLTIw/N}}: \quad \begin{aligned} \dot{\mathbf{x}} &= \mathbf{f}(\mathbf{x},\mathbf{u}) + G\mathbf{w} \\ \mathbf{y} &= \mathbf{h}(\mathbf{x}), \end{aligned} \tag{5.1}$$

where $\mathbf{w}$ is the vector of noise components. In order to address the assessment of observability in the presence of noise, the stochastic empirical Gramian was introduced in [20] with two calculation methods. One method is computing new sample trajectories for each entry of the Gramian; in this case the total number of simulations is $4n^2$ and the Gramian is not guaranteed to be at least positive semi-definite. In this study, we adopted the second method and run $2n$ simulations in total, assuming that $\Phi^{\varepsilon}(t, \mathbf{x}_0, \mathbf{u}, \mathbf{w}^{+1}, \mathbf{w}^{-1}, \ldots, \mathbf{w}^{+n}, \mathbf{w}^{-n})$ and its transpose are obtained from the same simulations. Here, $\mathbf{w}^{\mp i}$ is the noise sequence used to obtain the output $\mathbf{y}^{\mp i}$.

Unlike the empirical Gramian for deterministic systems, the spectrum of the stochastic Gramian would be different each run of the simulation, even though the initial state, the input sequence, and the simulation time remain the same. Additionally, measures such as the condition number and the unobservability index cannot be assumed to have Gaussian distributions when the system is simulated a large number of times, as illustrated in [20] for two different systems. Finally, an expected value of Gramian-based observability metrics cannot usually be obtained analytically due to the complex dynamics.

In [20], it was also illustrated that the unobservability index decreases as the noise variance increases which makes sense as the output energy will be higher although there is more uncertainty. On the other hand, it was shown that the estimation condition number is not a monotonic function of the noise level. Finally, we simulated both systems from [20] and observed that the the reciprocal of the n-th root of the determinant of the empirical Gramian has similar behaviour to the unobservability index.

5.2 Sensor Placement Problem and Methodology

Based on the output energy from different sensor locations of a system, one could expect different levels of observability. In this section, we present a sensor placement methodology based on the spectrum of the stochastic observability Gramian. To obtain the information of interest, we perform Monte Carlo analysis where the number of simulations was chosen based on convergence of the results.

Let $j : \mathbb{R}^{n \times n} \to \mathbb{R}$ be an unobservability metric as a function of the empirical observability Gramian. Then the mean value of this metric obtained from K simulations,

$$\hat{J}(t_1, \mathbf{x}_0, u) := \frac{1}{K} \sum_{i=1}^{K} j((W_o^\varepsilon)_i), \tag{5.2}$$

would be the expected value of the metric for a large K, and it is desired to be minimized for the sensor placement problem. In other words, if p is the finite number of possible sensor locations and we define $(W_o^\varepsilon)_{k_i}$ as the observability Gramian matrix obtained at the k-th sensor location on the i-th run, then

$$(W_o^\varepsilon)_i(\boldsymbol{\gamma}) = \sum_{k=1}^{p} \gamma_k (W_o^\varepsilon)_{ki}, \tag{5.3}$$

where $\boldsymbol{\gamma}$ is the vector of Boolean-valued sensor activation functions, γ_i. The optimal sensor selection problem can be formulated as

$$\begin{aligned} \min_{\gamma} \quad & \hat{J}(\boldsymbol{\gamma}) \\ \text{subject to} \quad & \sum \gamma = r \\ & \gamma_i \in \{0, 1\}, \end{aligned} \tag{5.4}$$

where $r \leq p$ is the desired number of sensors. We are currently unaware of a convex relaxation for j if it is the condition number or the unobservability index when K is greater than one.

To deal with the non-convexity of Prob. (5.4), we applied the *particle swarm optimization (PSO)* algorithm, a metaheuristic approach introduced in [62]. The PSO algorithm is a technique that generates several solution candidates, i.e., particles, and updates their position and velocity according to certain rules until a termination criterion is met [62]. Since this method is not problem-specific and allows abstract level description [63], it is straightforward to implement. It also permits the definition of a search region, which is not the case for some widely-used algorithms such as the downhill simplex method [64].

A pseudo-code for PSO algorithm is given in Alg. 1. Here, $J : \mathbb{R}^d \to \mathbb{R}$ is the objective function of unknown x to minimize, ub and lb are upper and lower bound vectors of the search space respectively, $r = |ub - lb|$, and ω, ϕ_p, and ϕ_g are user-defined parameters which have been discussed in detail in [65].

The pure PSO does not guarantee identification of the absolute local minimum. Hence, its hybridization with other optimization algorithms is studied in the literature to find a better solution. A review of hybridization methods and comparison of three of them are given in [66]. We also follow a hybrid approach, and at the expense of some computation

Algorithm 1 Basic PSO algorithm

```
procedure PSO($s$, $ub$, $lb$, $\omega$, $\phi_p$, $\phi_g$)
    Uniformly distribute random particles, $x$'s, in $[lb, ub]$
    Uniformly distribute random velocities, $v$'s, in $[-r, r]$
    for $i \in [1, s]$ do
        $p_i \leftarrow x_i$
    $J(g) = \min_{i\in[1,s]} J(p_i)$
    while a termination criterion is not met do
        for $i \in [1, s]$ do
            for $j \in [1, d]$ do
                Uniformly distribute random $r_p$, $r_g$ in $[0, 1]$
                $v_{i,j} = \omega v_{i,j} + \phi_p r_p (p_{i,j} - x_{i,j}) \ldots$
                    $+\phi_g r_g (g_d - x_{i,j})$
            $x_i = x_i + v_i$
            if $J(x_i) < J(p_i)$ then
                $p_i \leftarrow x_i$
                if $J(p_i) < J(g)$ then
                    $g \leftarrow p_i$
```

time, use the result from PSO to initiate a second search by the *interior point method (IPM)* discussed in [67].

Note that the PSO algorithm requires a continuous search region, as opposed to be restricted to be able to have sensors at the p potential locations in (14), and if each sensor has two coordinates to be determined, then the search space is $2r$-dimensional and the search would take more time as r increases. To avoid having sensors too close to each other, we also implemented a relatively large positive value, σ, as the penalty for proximity.

The following pseudocode summarizes our approach to optimal sensor placement in a continuous space with upper and lower bounds, ub and lb. Here, $d_{\min}$ is the minimum distance between any two of r sensors, and d_{allowed} is the minimum distance allowed. The PSO and IPM algorithm parameters have been suppressed for brevity.

Algorithm 2 Optimal Sensor Placement

```
procedure (dynamics, $ub$, $lb$, $j$, $K$, $r$, $d_{\text{allowed}}$, $\sigma$)
    define $(W_o^\varepsilon)_i \leftarrow \sum_{k=1}^{r} (W_o^\varepsilon)_{k_i}$
    define $\hat{J} \leftarrow \begin{cases} \frac{1}{K}\sum_{i=1}^{K} j((W_o^\varepsilon)_i) & d_{\min} \geq d_{\text{allowed}} \\ \sigma & d_{\min} < d_{\text{allowed}} \end{cases}$
    sensor loci ← PSO($\hat{J}$,$ub$, $lb$)
    sensor loci ← IPM($\hat{J}$,$ub$, $lb$, sensor loci)
```

5.3 Numerical Applications

We will explore the work here relative to two examples, the first being the low-dimension dynamics of a UAV system and the other a flapping wing system with flexible structure described by infinite dimensional modal dynamics.

5.3.1 UAV Navigation System

Dynamics Model

A simplified planar model of a nonholonomic fixed-wing aircraft in the presence of air currents is given in [49] as:

$$\begin{aligned} \dot{\mathbf{x}} &= \begin{bmatrix} V\cos x_3 + x_4 \\ V\sin x_3 + x_5 \\ u \\ 0 \\ 0 \end{bmatrix} + \begin{bmatrix} 1 & 0 \\ 0 & 1 \\ 0 & 0 \\ 0 & 0 \\ 0 & 0 \end{bmatrix} \mathbf{w} \\ \mathbf{y} &= \begin{bmatrix} x_1 \\ x_2 \end{bmatrix}, \end{aligned} \tag{5.5}$$

where $\mathbf{x} = \begin{bmatrix} x_E & y_N & \theta & W_x & W_y \end{bmatrix}^\top$. The aim is to estimate the wind components in x and y directions, W_x and W_y. Here, x_E and y_N are the vehicle's inertial East and North positions, and θ is its inertial orientation. Finally, V is the vehicle flow-relative velocity, which is assumed to be constant, and the control input, u, is the vehicle's angular velocity. The two components of the process noise vector, $\mathbf{w}$, are zero-mean Gaussian with the covariance matrix Q.

Results

As shown in prior work [49], a Lie algebraic approach for deterministic observability analysis can be used to show that the system (5.5) is unobservable if there is no control input, $u(t) = 0$ and no noise, $\mathbf{w} = \mathbf{0}$. To explore the effects of noise, we simulated the control-free system with five different levels of process noise for $K = 100$ simulations with $\mathbf{x}_0 = \begin{bmatrix} 0 & 0 & \pi/6 & 0.35 & -0.15 \end{bmatrix}^\top$ and $t_1 = 150\,\mathrm{s}$. Since the first two states are directly measured, we select the remaining states as states of interest. By allowing the nonzero process noise on x_1 and x_2, the stochastic empirical observability Gramian results in all nonsingular observability Gramians indicating an observable system, although the system would be considered unobservable using the traditional deterministic observability analysis tools.

Figure 5.1 shows the resultant unobservability metrics $\nu(W_o^\epsilon)$ and $1/[\det(W_o^\epsilon)]^{1/n}$. We observe a monotonic decrease in the unobservability index and its variance as the noise level increases. We also note the significant correlation between the two metrics, $\rho = 0.8716$, although this correlation depends on the system dynamics itself as well as the covariance matrix.

If we define the unobservability metric as a linear combination of the condition number and the unobservability index,

$$j(W_o^\epsilon) = \kappa(W_o^\epsilon) + w_\nu \nu(W_o^\epsilon), \tag{5.6}$$

then the weight of $\nu(W_o^\epsilon)$, w_ν, will be of particular importance since κ does not appear monotonic as a function of the noise; the non-monotonicity of the condition number can be seen in Fig. 5.2 at $w_\nu = 0$. Figure 5.2 also illustrates this inference: as the unobservability index becomes dominant in the objective function, lower process noise on the system becomes

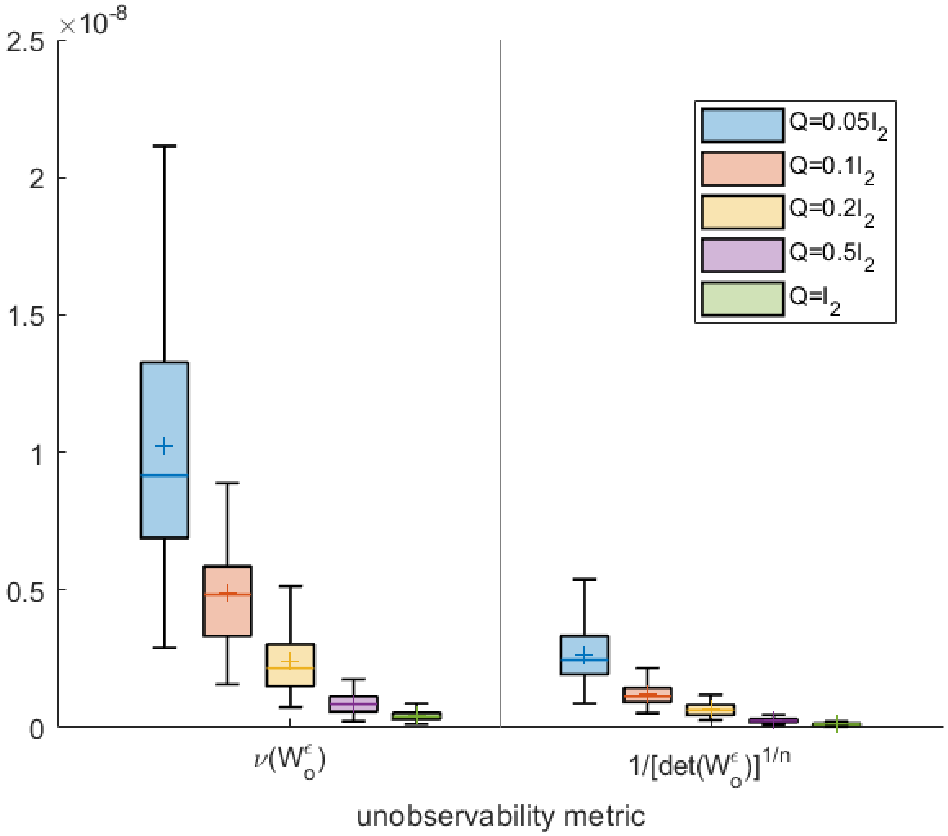

Figure 5.1: The change of two unobservability metrics as the noise level increases. Here, horizontal lines with color indicate the median value, and the plus sign denotes the mean. I_2 is the 2×2 identity matrix.

less preferable.

5.3.2 Flapping Wing System

For this work, we studied optimal neural-inspired sensor placement on the flapping wing using its FEA model and aimed to increase observability. We were particularly inspired/informed by a previous study [10] that showed that the existence of externally induced body rotation as large as $\omega = 10\,\mathrm{rad\,s^{-1}}$ on a flapping wing differs by a twisting mode three orders of magnitude smaller than the dominant flapping mode.

In order to explore the determination of optimal sensor placement in a higher dimension

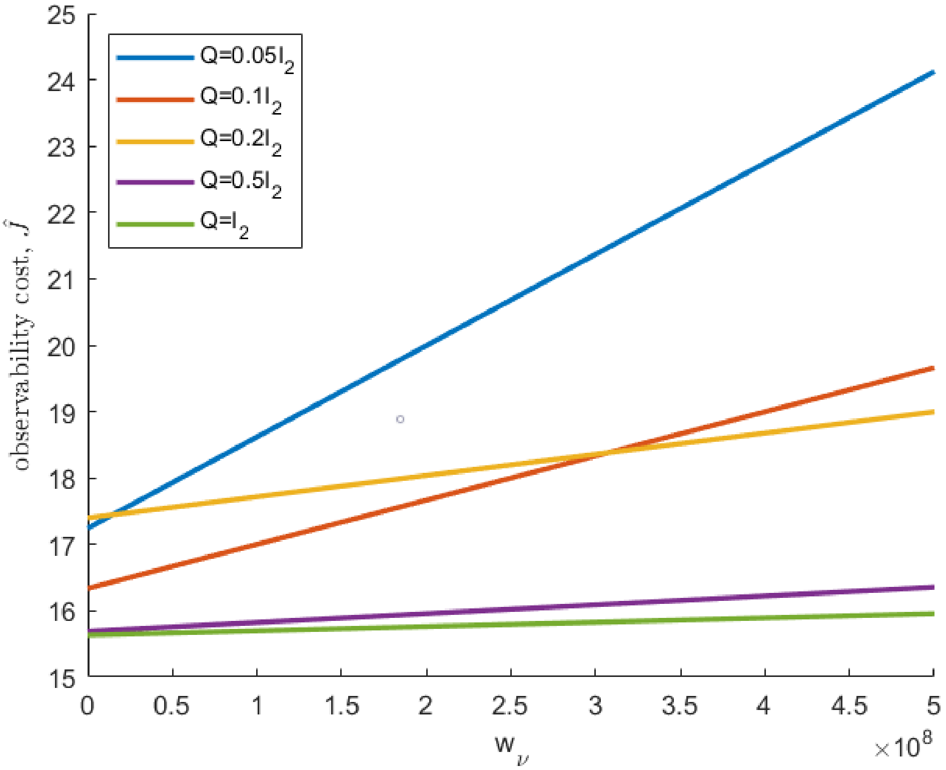

Figure 5.2: The cost of observability, $\hat{J}$, changing with the weight of the unobservability index for the five noise levels on the control-free UAV system.

stochastic framework using empirical Gramian methods, we will frame the work around a biologically inspired flapping flight example. The dynamics of a continuum flexible system represented in modal coordinates, $\boldsymbol{\eta}$, can be expressed as

$$\mathbf{M}\ddot{\boldsymbol{\eta}} + \mathbf{C}\dot{\boldsymbol{\eta}} + \mathbf{K}\boldsymbol{\eta} = \mathbf{u}(t) + \begin{bmatrix} 1 & 0 \\ 0 & 1 \\ 0 & 0 \\ \vdots & \vdots \end{bmatrix} \mathbf{w}, \quad \mathbf{y} = \mathbf{h}(\eta), \tag{5.7}$$

where $\mathbf{M}$ is the mass matrix, $\mathbf{C}$ is the damping matrix, $\mathbf{K}$ is the stiffness matrix, $\mathbf{u}$ is the vector of external forces. We define the augmented system state as the mode shapes, their time derivatives and the flapping rate, $\dot{\phi}$, and rotation rate, ω, of the wing:

$$\mathbf{x} = \begin{bmatrix} \dot{\phi} & \omega & \boldsymbol{\eta}^T & \dot{\boldsymbol{\eta}}^T \end{bmatrix}^T .$$

The overall dynamics can then be expressed as

$$\begin{aligned} \dot{\mathbf{x}} &= \mathbf{f}(\mathbf{x}, \mathbf{u}(t)) + \begin{bmatrix} 1 & 0 \\ 0 & 1 \\ 0 & 0 \\ \vdots & \vdots \end{bmatrix} \mathbf{w} \\ \mathbf{y} &= \mathbf{h}(\mathbf{x}), \end{aligned} \tag{5.8}$$

where $\mathbf{w}$ is the vector of independent and identically distributed (i.i.d.) zero-mean Gaussian process noises with diagonal covariance matrix, $Q \in \mathbb{R}^{n \times n}$. The system measurements are assumed to be provided from the neural encoding model described in Subsec. 2.1.2 with the model parameters given in Subsec. 4.3.1.

FEA Model

To express the system dynamics of the wing via a finite number of mode shapes, we created a finite element analysis (FEA) model in COMSOL Multiphysics® 5.6 software to study the dynamics and the observability of a flapping wing. We generated this simplified model based on the properties of the hawkmoth *Manduca Sexta* wing. As shown in Fig. 5.3a, the structure was modeled as a single rectangular thin plate with a width of 25 mm, length of 50 mm, and thickness of 12.7 µm. We considered the thickness of the structure to be uniform throughout the wing, and the effect of venation was neglected in the simulations. To define the Young's modulus (E) of the wing, we picked a value within the range of stiffness values measured previously for insect wings [68].

The damping has a significant effect on the dynamic response and the strain patterns generated due to flapping. Hence, we adopted a Rayleigh damping model with damping matrix defined as a linear combination of the mass and the stiffness matrices specified using proportionality coefficients α and β:

$$\mathbf{C} = \alpha\mathbf{M} + \beta\mathbf{K}. \tag{5.9}$$

Values for the material properties used in the FEA model are shown in Table 5.1. The wing was modeled as linearly elastic. The system was meshed using 25 by 50 structured quadrilateral elements swept through the thickness of the plate (Fig. 5.3b). The mesh size was selected based on a mesh convergence analysis to ensure the accuracy of the results and minimum computation time.

We applied boundary conditions to mimic the flapping pattern of *Manduca* using the steady flapping model from [10]. The model has an amplitude of $\pi/6$ radians and consists of two harmonic components to match the experimental results. The first component acts at a frequency of f_1 =25 Hz, while the second component with 1/5 of the amplitude has a frequency of f_2 =50 Hz. We introduced flapping in terms of angular velocity by taking the time derivative of the flapping angle model, that is,

$$\dot{\phi}(t) = \frac{\pi}{6}(2\pi f_1 cos(2\pi f_1 t) + \frac{2\pi f_2}{5} cos(2\pi f_2 t)). \tag{5.10}$$

In addition to flapping, we introduced perturbation in the form of inertial rotation as shown in Fig.5.3a. Although the nominal trajectory involves no rotation, we were required to add a rotation of small magnitude ($\omega = 0.02\,\mathrm{rad\,s^{-1}}$) to ensure convergence of the model. This rotation will also impose asymmetry, which naturally comes from the asymmetrical shape and stiffness of the wing.

The random function in COMSOL software allowed us to use a random seed that is guaranteed to generate a new noise sequence while maintaining the same distribution. Proportionally to the nominal trajectory, we picked $Q = \mathrm{diag}(1, 1 \times 10^{-4})(\mathrm{rad\,s^{-1}})^2$ where the

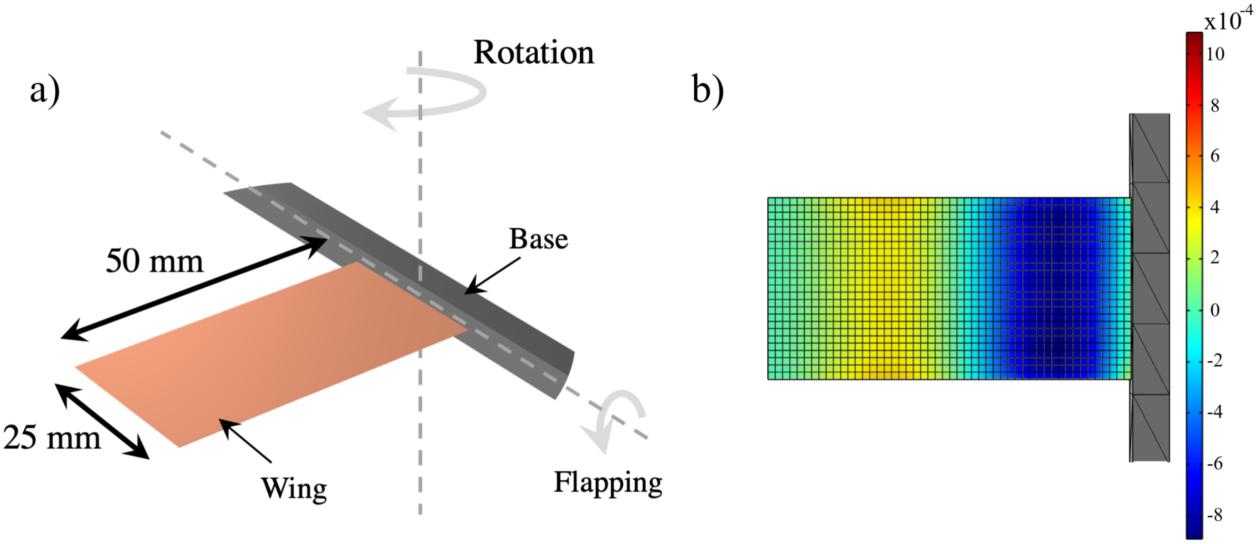

Figure 5.3: (a) Details of structural model and boundary conditions for flapping wing model in COMSOL, (b) meshing of the wing plate and normal strain distribution on the top surface of wing.

Table 5.1: Material properties used in COMSOL simulations

Properties	**Values**
Young's Modulus (E)	0.3 GPa
Poisson's Ratio	0.35
Mass Damping Coefficient (α)	$500\,\mathrm{s}^{-1}$
Stiffness Damping Coefficient (β)	0 s
Density	$1180\,\mathrm{kg/m}^3$

larger variance corresponds to the noise on the flapping rate.

For each simulation, we extracted the normal strain along the length of the wing (Fig. 5.3b) to feed the neural encoding model, which is outlined in the following subsection.

Results

We simulated the FEA model for 0.2 s (5 wingbeats) using time step of 5×10^{-4} s. The motion was prescribed through angular velocities of flapping and rotation. Both velocities were zero through the first wingbeat cycle and linearly increased to their maximum values ($\sim$57 rad s^{-1}

for flapping and $0.02\,\mathrm{rad\,s^{-1}}$ for rotation) over the course of the second cycle. We ran the simulation for two more cycles before introducing the perturbation, $\varepsilon = 0.01\,\mathrm{rad\,s^{-1}}$, to the system. Again, a regular cycle before the perturbation was necessary as the neural-encoded output requires the system to have a memory, unlike the typical systems. The system was simulated one more cycle after the introduction of the perturbation, i.e., $t_1 = 40\,\mathrm{ms}$.

The resultant distributions of the average unobservability index and the condition number stabilized in $K = 40$ sets of simulations. In Fig. 5.4, it can be seen that the unobservability index increases almost monotonically from the wing root ($x = 0$) to the wingtip ($x = -5$). On the other hand, there are two separate regions where the eigenvalues are relatively more balanced. Finally, note that the asymmetric distributions about the x-axis are caused by the nonzero rotation rate.

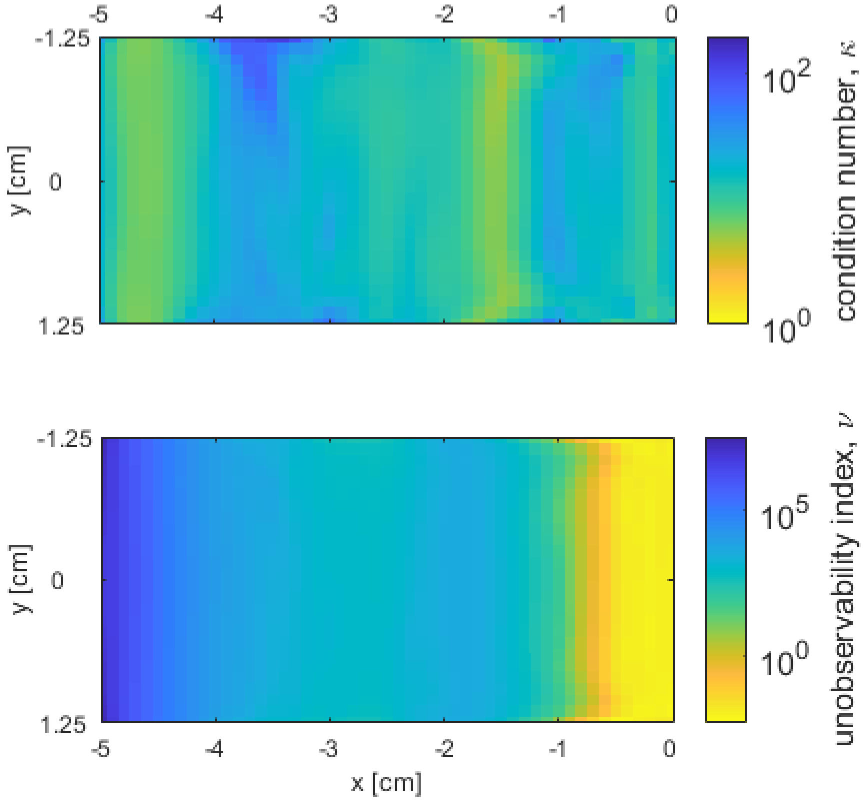

Figure 5.4: The average distribution of two unobservability metrics ($K = 40$). Yellow regions are more observable than the dark blue ones.

We then ran the hybrid PSO algorithm for r from one to 20 to minimize the linear combination of κ and ν with $w_\nu = 0.1$ and to minimize solely the condition number, $w_\nu = 0$. Since the search was performed in a continuous space, the strain value at a point was calculated as a weighted average of the strain values obtained for the neighboring FEA nodes. To avoid having sensors placed closer to each other than 1 mm, we determined the penalty value as $\sigma = 1 \times 10^5$.

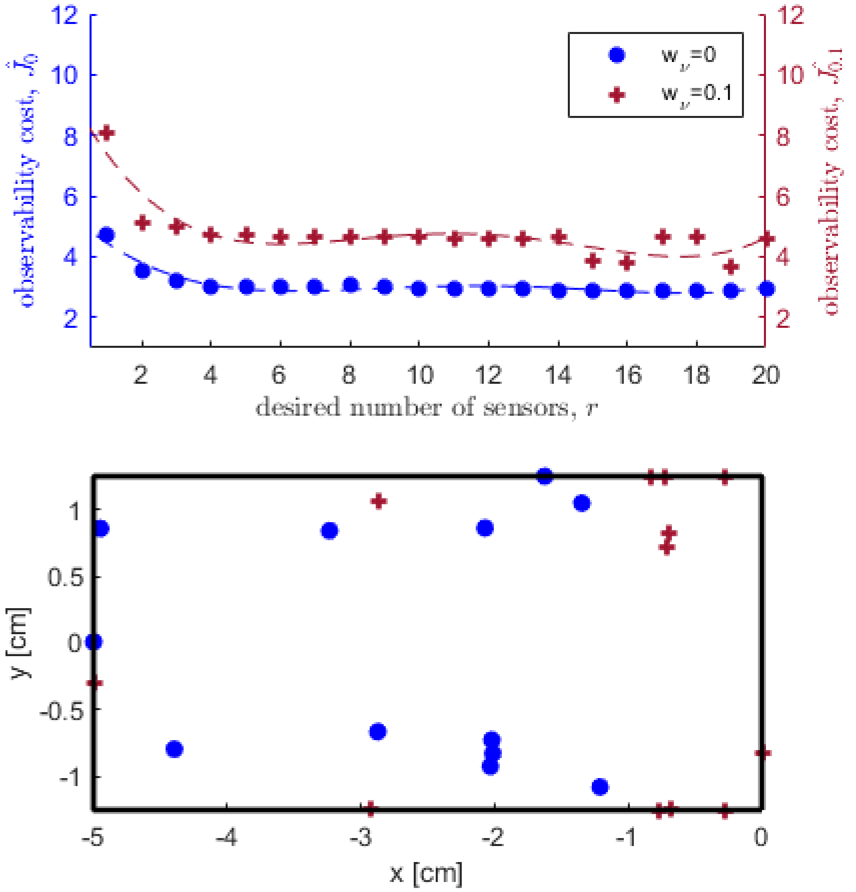

Figure 5.5: (a) The change of the observability costs by the number of sensors with fourth-degree polynomial fitting, (b) The optimal neural-inspired sensor placement for $r = 12$. The figures use the same legend.

The value of the observability cost function for increasing numbers of desired sensors is given in Fig. 5.5a. Both the condition number and its linear combination with the unobservability index converge, and adding a new sensor does not improve the observability significantly for $r \geq 5$, which might be partially caused by the increasing dimension of the search space.

Lastly, the optimal sensor placement for $r = 12$ is shown in Fig. 5.5b. When the linear combination of the two metrics with $w_\nu = 0.1$ was utilized instead of a single observability index, the sensors were slightly shifted to the left, and at least one sensor was placed at each edge. The use of pure condition number ($w_\nu = 0$) resulted in having no sensors in the regions where the output energy is highest.

5.4 Discussion on the Optimization Problem

Although it is a good first step to study the minimization of the average (expected) value of the empirical Gramian-based cost function obtained from K runs, higher moments of the probabilistic distribution (variance, skewness, and so on) might also be considered while posing the optimization problem. For example, trust levels for sensor location candidates can be determined by the variance of the unobservability metrics at those points. Such an approach would be similar to the weighted least squares used in linear batch estimation [23] or to the distributed least squares estimation in sensor networks [69].

Second, we restricted the activation vector, $\boldsymbol{\gamma}$, to get binary values, and introducing such a constraint automatically makes the problem non-convex. However, as in the example of wireless sensor networks [70, 71], we can discuss probabilistic distribution of sensors. In that case, the problem would be relaxed as the activation vector would get values between zero and one.

Finally, we note that the estimation condition number, κ, cannot have even a generalized normal distribution as it is bounded from below, so its truncated distribution should be studied.

Chapter 6

TRAJECTORY DESIGN TO ENSURE AND IMPROVE OBSERVABILITY

In the previous sections, we repeatedly saw that the observability and the metrics of (un)observability of systems with nonlinear dynamics are affected by the input profiles (the trajectory a system follows). In this section, we first give approaches to find control inputs (excitation profiles) to ensure or maximize the observability of nonlinear systems with measurable first p states in the form,

$$\begin{aligned}\dot{\mathbf{x}}(t) &= \mathbf{f}(\mathbf{x}(t), \mathbf{u}(t)) \\ \mathbf{y}(t) &= \mathbf{h}(\mathbf{x}(t)) = \begin{bmatrix} I_p & \mathbf{0}_{p\times(n-p)} \end{bmatrix} \mathbf{x}(t),\end{aligned}$$

for $n/2 \leq p < n$, then study the observability of inertial parameters of a rigid body subjected to some excitation.

6.1 Ensuring Observability via Orthogonality of the Rows of $d\mathcal{G}$

One way to ensure observability of a nonlinear system is to make the corresponding observability matrix orthogonal or nearly orthogonal, as its rank being full indicates observability. In this section, we discuss the design of control policies to guarantee observability. Unlike the previous work by Alaeddini and Morgansen [56], we consider the multiple-output case and aim for (near) orthogonality of the Jacobian of the Lie algebra consisting of the measurement function and its first derivative. The intuition for constructing the observability matrix with $2p$ rows comes from linear control theory: One can design a simpler functional observer if T-step observability matrix, $\mathcal{O}_T$, is full (column) rank for small T [72].

6.1.1 Observability-based Control Policy

Consider a multiple-input-multiple-output nonlinear system in control-affine form where the first p of n states are available and $n/2 \leq p < n$,

$$\begin{aligned} \dot{\mathbf{x}}(t) &= \mathbf{f}(\mathbf{x}(t), \mathbf{u}(t)) = \begin{bmatrix} f_1(\mathbf{x}(t), \mathbf{u}(t)) \\ \vdots \\ f_n(\mathbf{x}(t), \mathbf{u}(t)) \end{bmatrix} \\ \mathbf{y}(t) &= \mathbf{h}(\mathbf{x}(t)) = \begin{bmatrix} I_p & \mathbf{0}_{p\times(n-p)} \end{bmatrix} \mathbf{x}(t), \end{aligned} \tag{6.1}$$

where

$$f_j(\mathbf{x}(t), \mathbf{u}(t)) = f_{0j}(\mathbf{x}(t), \mathbf{u}(t)) + \sum_{i=1}^{n_i} f_{ij}(\mathbf{x}(t)) u_i(t) \quad \text{for } j \in \{1, \dots, n\}. \tag{6.2}$$

Then define a Lie algebra as the span of up to the first Lie derivative of $\mathbf{h}$ with respect to the state vector, $\mathbf{x}$, on the vector field $\mathbf{f}$:

$$\mathcal{G}_2 := \operatorname{span}\{\mathbf{h}, L_{\mathbf{f}}\mathbf{h}\}. \tag{6.3}$$

The Jacobian of $\mathcal{G}_2$ can be written as:

$$d\mathcal{G}_2 = \begin{bmatrix} d\mathbf{h} \\ dL_{\mathbf{f}}\mathbf{h} \end{bmatrix} = \begin{bmatrix} \multicolumn{3}{c}{I_p} & \multicolumn{3}{c}{\mathbf{0}_{p\times(n-p)}} \\ \frac{\partial f_1}{\partial x_1} & \cdots & \frac{\partial f_1}{\partial x_p} & \frac{\partial f_1}{\partial x_{p+1}} & \cdots & \frac{\partial f_1}{\partial x_n} \\ \vdots & \ddots & \vdots & \vdots & \ddots & \vdots \\ \frac{\partial f_p}{\partial x_1} & \cdots & \frac{\partial f_p}{\partial x_p} & \frac{\partial f_p}{\partial x_{p+1}} & \cdots & \frac{\partial f_p}{\partial x_n} \end{bmatrix}, \tag{6.4}$$

where we have dropped dependence of f_i's on $\mathbf{x}(t)$ and $\mathbf{u}(t)$ for brevity.

The system (6.1) is observable if $\operatorname{rank} d\mathcal{G}_2 = n$. Moreover, a sufficient condition for mutual orthogonality of n rows can be stated as given below.

Theorem 7 *The* n *rows of* $d\mathcal{G}_2$ *are mutual orthogonal if*

$$\frac{\partial f_{j_1}}{\partial x_i} = \cdots = \frac{\partial f_{j_{n-p}}}{\partial x_i} = 0, \quad \forall i \in \{1, \ldots, p\},$$

$$\begin{bmatrix} \frac{\partial f_{j_1}}{\partial x_{p+1}} & \ldots & \frac{\partial f_{j_1}}{\partial x_n} \end{bmatrix} \begin{bmatrix} \frac{\partial f_{k_1}}{\partial x_{p+1}} & \ldots & \frac{\partial f_{k_1}}{\partial x_n} \end{bmatrix}^\top = 0$$

$$\vdots$$

$$\begin{bmatrix} \frac{\partial f_{j_{n-p}}}{\partial x_{p+1}} & \ldots & \frac{\partial f_{j_{n-p}}}{\partial x_n} \end{bmatrix} \begin{bmatrix} \frac{\partial f_{k_{n-p}}}{\partial x_{p+1}} & \ldots & \frac{\partial f_{k_{n-p}}}{\partial x_n} \end{bmatrix}^\top = 0,$$

where $j_1, \ldots, j_{n-p}, k_1, \ldots, k_{n-p} \in \{1, \ldots, p\}$, $j_q \neq k_q$, $j_q \neq j_r$ *and* $k_q \neq k_r$ *if* $q \neq r$, *and* $\mathcal{J} = \{j_1, \ldots, j_{n-p}\} = \mathcal{K} = \{k_1, \ldots, k_{n-p}\}$.

Proof The first p rows of $d\mathcal{G}_2$ are already orthogonal to each other. If $n-p$ rows are selected from the set $\{dL_{\mathbf{f}}h_1, \ldots, dL_{\mathbf{f}}h_p\}$, then these rows should have no components in the direction of the first r rows, that is,

$$\frac{\partial f_{j_1}}{\partial x_i} = \cdots = \frac{\partial f_{j_{n-p}}}{\partial x_i} = 0, \quad \forall i \in \{1, \ldots, p\} \tag{6.5}$$

Since the first p entries of each selected rows are zero, the inner product of two rows becomes

$$\begin{bmatrix} \frac{\partial f_{j_q}}{\partial x_{p+1}} & \ldots & \frac{\partial f_{j_q}}{\partial x_n} \end{bmatrix} \begin{bmatrix} \frac{\partial f_{k_q}}{\partial x_{p+1}} & \ldots & \frac{\partial f_{k_q}}{\partial x_n} \end{bmatrix}^\top, \qquad j_q \neq k_q,$$

which should be equal to zero for the mutual orthogonality of selected rows. ■

Although it is hard and usually impossible to find a control input for high-order systems that satisfies the condition given in Theorem 7, this approach can be helpful for low-order systems or systems with small $n-p$ values.

Example Consider the dynamics of a tunnel-diode circuit [73],

$$\begin{aligned}\dot{x}_1 &= \frac{1}{L}[-x_2 - Rx_1 + u]\\ \dot{x}_2 &= \frac{1}{C}[-l(x_2) + x_1]\\ y &= x_1,\end{aligned} \tag{6.6}$$

where $l : \mathbb{R} \to \mathbb{R}$ is a nonlinear function of the voltage on the tunnel diode. Equation (6.5) should be satisfied for the orthogonality of dh and $dL_{\mathbf{f}}h$, that is,

$$\frac{\partial f_1}{\partial x_1} = -\frac{R}{L} + \frac{1}{L}\frac{\partial u}{\partial x_1} = 0 \implies u(\mathbf{x}) = Rx_1 + c_u,$$

for some constant c_u. One should finally make sure that the system is observable, i.e., $\partial f_1/\partial x_2 \neq 0$.

In the example above, the Jacobian of the Lie algebra $\mathcal{G}_2$, $d\mathcal{G}_2$, was a square matrix as $p = n/2$, hence we aimed for the mutual orthogonality of all the rows. The following corollary is given for this special case.

Corollary 3 *Consider the system (6.1) and assume that $p = n/2 \in \mathbb{Z}^+$. Define a Lie algebra as $\mathcal{G}_2 = \operatorname{span}\{\mathbf{h}, L_{\mathbf{f}}\mathbf{h}\}$. The rows of the Jacobian matrix, $d\mathcal{G}_2 = \begin{bmatrix} d\mathbf{h}^\top & dL_{\mathbf{f}}\mathbf{h}^\top \end{bmatrix}^\top$, are orthogonal to each other if and only if $d\mathcal{G}_2 d\mathcal{G}_2^\top$ can be written in the form,*

$$d\mathcal{G}_2 d\mathcal{G}_2^\top = \left[\begin{array}{cccc} I_p & & \mathbf{0}_{p\times(n-p)} & \\ & d_1 = \sum_{i=p+1}^{n}(\frac{\partial f_1}{\partial x_i})^2 & \mathbf{0}_{1\times(n-p-2)} & 0 \\ \mathbf{0}_{p\times p} & \mathbf{0}_{(p-2)\times 1} & \ddots & \mathbf{0}_{(p-2)\times 1} \\ & 0 & \mathbf{0}_{1\times(n-p-2)} & d_p = \sum_{i=p+1}^{n}(\frac{\partial f_p}{\partial x_i})^2 \end{array}\right]. \tag{6.7}$$

Moreover, $d_i \neq 0$ for all i is a required inequality constraint for the invertibility of $d\mathcal{G}_2$.

Proof The first part is an immediate result from Theorem 7 for $p = n/2$. The invertibility of $d\mathcal{G}_2$ requires $d_i \neq 0$ for all i since none of its columns/rows should be all zeros, so the sum of squares that defines d_i cannot be equal to zero. ■

Here, there are $2p^2 - p$ equality constraints on $\mathbf{f}$.

6.1.2 Observability-based Trajectory Tuning

Assume that the control and the corresponding trajectory are given and a small tuning term, $\mathbf{w}(t)$, is added to the nominal control,

$$\mathbf{u}(\mathbf{x}(t), t) = \mathbf{u}^{\text{nom}}(\mathbf{x}(t)) + \mathbf{w}(t). \tag{6.8}$$

For system (6.1), we have

$$\langle dh_i, dL_{\mathbf{f}} h_j \rangle = \frac{\partial f_j}{\partial x_i}, \quad \forall i, j \in \{1, \dots, p\}. \tag{6.9}$$

Also, define polynomials of order ≤ 2 such that

$$\begin{aligned} P^{ij}(\mathbf{w}(t)) :&= \langle dL_{\mathbf{f}} h_i, dL_{\mathbf{f}} h_j \rangle \big|_{\mathbf{x}=\mathbf{x}^{\text{nom}}, \mathbf{u}=\mathbf{u}^{\text{nom}}} \\ &= \sum_{k=1}^{n} \frac{\partial f_i}{\partial x_k} \frac{\partial f_j}{\partial x_k} \bigg|_{\mathbf{x}=\mathbf{x}^{\text{nom}}, \mathbf{u}=\mathbf{u}^{\text{nom}}}, \end{aligned} \tag{6.10}$$

for all $i, j \in \{1, \dots, p\}$ where $\mathbf{x}^{\text{nom}}$ is the nominal trajectory corresponding to $\mathbf{u}^{\text{nom}}$.

Case 1: $p = n/2$

If $p = n/2$, then one should aim for near orthogonality of all the rows of the observability matrix, $d\mathcal{G}_2$, to each other. Then an observability-based trajectory tuning optimization problem can be written as

$$\begin{aligned}\min_{\mathbf{w}(\tau)} \quad & \sum_{i=1}^{p}\sum_{j=1}^{p}\left(\left.\frac{\partial f_j(\mathbf{w}(\tau))}{\partial x_i}\right|_{\substack{\mathbf{x}=\mathbf{x}^{\text{nom}}\\ \mathbf{u}=\mathbf{u}^{\text{nom}}}}\right)^2 + \sum_{i=1}^{p-1}\sum_{j=i+1}^{p}[P^{ij}(\mathbf{w}(\tau))]^2 \\ \text{subject to} \quad & \|\mathbf{w}(\tau)\|^2 < \varepsilon',\end{aligned} \tag{6.11}$$

where ε' is a small value that determines the maximum allowable perturbation size of $\mathbf{u}^{\text{nom}}$. The problem (6.11) can also be written in the form of regularization problem,

$$\min_{\mathbf{w}(\tau)} \sum_{i=1}^{p}\sum_{j=1}^{p}\left(\left.\frac{\partial f_j(\mathbf{w}(\tau))}{\partial x_i}\right|_{\substack{\mathbf{x}=\mathbf{x}^{\text{nom}}\\ \mathbf{u}=\mathbf{u}^{\text{nom}}}}\right)^2 + \sum_{i=1}^{p-1}\sum_{j=i+1}^{p}[P^{ij}(\mathbf{w}(\tau))]^2 + \delta\|\mathbf{w}(\tau)\|^2, \tag{6.12}$$

where δ is a positive scalar.

Finally, as discussed in [56], a quadratic programming (QP) problem can also be posed for $n = 2$.

Case 2: $n/2 < p < n$

As discussed above, if $n/2 < p < n$, then some rows of $d\mathcal{G}_2$ would inevitably be linearly dependent, and we should aim for the mutual orthogonality of n selected rows to each other.

The first p rows are already orthogonal to each other. Let the binary-valued selection vector be $\mathbf{s} = \begin{bmatrix} s_1 & \cdots & s_p \end{bmatrix}^\top$ where $s_i \in \{0, 1\}$ and $\sum_{i=1}^{p} s_i = n - p$. Then the observability-based trajectory tuning problem can be written as a mixed-integer program (MIP),

$$\begin{aligned}\min_{\mathbf{w}(\tau),\ \mathbf{s}} \quad & \sum_{i=1}^{p}\sum_{j=1}^{p} s_j\left(\left.\frac{\partial f_j(\mathbf{w}(\tau))}{\partial x_i}\right|_{\substack{\mathbf{x}=\mathbf{x}^{\text{nom}}\\ \mathbf{u}=\mathbf{u}^{\text{nom}}}}\right)^2 + \sum_{i=1}^{p-1}\sum_{j=i+1}^{p} s_i s_j[P^{ij}(\mathbf{w}(\tau))]^2 \\ \text{subject to} \quad & \|\mathbf{w}(\tau)\|^2 < \varepsilon' \\ & \sum_{i=1}^{p} s_i = n - p,\end{aligned} \tag{6.13}$$

where ε' is a small value that determines the maximum allowable perturbation size of $\mathbf{u}^{\text{nom}}$.

Here, the rows are selected such that n rows are as close to being orthogonal to each other as possible.

6.2 Empirical Gramian-based Trajectory Planning to Improve Observability

In Chapter 1, we mentioned that the FIM is bounded by the empirical observability Gramian as the perturbation amount goes to zero. It was also shown that scalings of the integrand of the empirical observability Gramian set upper and lower bounds for the FIM is bounded above and below by scalings of the integrand of the empirical Gramian, that is, if the estimation condition number of the system is high, then the FIM is also likely to have a high condition number which is not desired due to numerical concerns [20]. Based on the output energy obtained from different input profiles on a system, one could expect different levels of observability. In this section, we first outline our methodology of designing multiple inputs to minimize the condition number of the empirical observability Gramian, $\kappa(W_o^\varepsilon)$, especially for the system identification problem. Then we propose an approach to the scaling of the perturbation amount and the measurements to build a reliable empirical observability Gramian.

6.2.1 Optimized Multisine Inputs

The approach given in the previous section requires to run the optimization algorithm for each time step to obtain the tuning term, $\mathbf{w}(\tau)$, and does not guarantee any smoothness. Here, we instead use parameterized multisine inputs, as suggested by Morelli [2],

$$u_j(t) = \sum_{k \in \{1,\ldots,M\}} \mathscr{A}_{jk} \sin\left(2\pi k f_{\text{base}} t + \phi_{jk}\right), \quad \text{for } j = 1, \ldots, n_i, \tag{6.14}$$

where M is the total number of available harmonic frequencies, i.e., $\omega_M = 2\pi M f_{\text{base}}$ is the frequency band upper limit for excitation, $\mathscr{A}_{jk}$ and ϕ_{jk} are the amplitude and the frequency for the k-th sinusoidal component, respectively. The inputs are mutually orthogonal in both time and frequency domains as the harmonic sinusoids have the same base frequency f_{base}

but unique harmonic frequencies, and the orthogonality is not affected by the values chosen for the phase angles, ϕ_{jk}'s [2].

Morelli also suggests choosing the phase angles such that the relative peak factor (RPF) of each input are kept at the minimum. We instead assume zero phase angle for all harmonic sinusoids and limit the maximum value of each input in the optimization problem. This way, the search space is kept Mn_i-dimensional. Hence, for given M, the problem of minimization of the estimation condition number, $\kappa(W_o^\varepsilon)$, can be written as:

$$\begin{aligned} \min_{\mathscr{A}_{jk}\text{'s}} \quad & \kappa(W_o^\varepsilon(t_1, \mathbf{x}_0, \mathbf{u})) \\ \text{subject to} \quad & u_j(t) \leq (ub)_j, \quad \forall t \in [0, t_1], \end{aligned} \tag{6.15}$$

where $(ub)_j$ is the upper bound on

$$u_j(t) = \sum_{k \in \{1,\ldots,M\}} \mathscr{A}_{jk} \sin\left(2\pi k f_{\text{base}} t\right), \quad \text{for } j = 1, \ldots, n_i. \tag{6.16}$$

The problem is multidimensional and non-convex and can be studied using a simplex algorithm or PSO. Neither of these methods promises for a global solution. If one decreases the base frequency while keeping Mf_{base} constant, then the search space would have a higher dimension which may cause end up with a more costly local optimal solution. On the other hand, if M is a large number, then the signal will look more like a random one, that is, the global solution to the problem will be better than the one to a problem with a smaller M value. We will consider these aspects in the next section while selecting the number of harmonics for a given Mf_{base}.

6.2.2 Perturbation Amount and Output Scaling

The output scaling in the presence of measurements with notably various orders of magnitude is studied for the sensor placement problem in [74], however, this study does not address the question of comparability of Gramian matrices obtained using different input sequences.

To be able to compare the observability of the system on different trajectories and find the optimal one, we suggest scaling the measurements from the same sensors by the same randomly chosen small values for all trajectories.

When the orders of magnitude are significantly different for the system states, another scaling method is needed in addition to the output scaling [50]. Instead of scaling the state vector, we propose to choose varying perturbation amounts for the r states of interest: If the initial state $(\mathbf{x}_0)_i$ is perturbed by ε_i, then the empirical observability Gramian can be obtained as:

$$W_o^{\boldsymbol{\varepsilon}}(t_1, \mathbf{x}_0, \mathbf{u}) = \frac{1}{4} \operatorname{diag}\left(\frac{1}{\varepsilon_1}, \dots, \frac{1}{\varepsilon_r}\right) \int_0^{t_1} \Phi^{\boldsymbol{\varepsilon}}(t, \mathbf{x}_0, \mathbf{u})^\top \Phi^{\boldsymbol{\varepsilon}}(t, \mathbf{x}_0, \mathbf{u}) dt \operatorname{diag}\left(\frac{1}{\varepsilon_1}, \dots, \frac{1}{\varepsilon_r}\right), \tag{6.17}$$

where $\boldsymbol{\varepsilon} = \begin{bmatrix} \varepsilon_1 & \dots & \varepsilon_r \end{bmatrix}^\top$ is the vector of perturbation amounts.

6.3 *Application: Estimation of Rigid Body Inertial Parameters*

6.3.1 Analytical Observability Analysis

In this subsection, we analyze the observability of inertial parameters for the two models introduced in Sec. 2.2 using the Lie algebraic method described for nonlinear systems.

6-DoF Rigid Body Dynamics

We first define an augmented state vector to be able to study the observability of the inertial parameters.

$$\mathbf{x}_{\text{aug}} = \begin{bmatrix} \mathbf{x}^\top & m & \mathbf{c}^\top & I_{xx} & I_{yy} & I_{zz} & I_{yz} & I_{xz} & I_{xy} \end{bmatrix}^\top \in \mathbb{R}^{22}, \tag{6.18}$$

then put the dynamics (2.9) in the control-affine form:

$$\dot{\mathbf{x}}_{\text{aug}} = \underbrace{\begin{bmatrix} \boldsymbol{\nu} \\ -\mathbf{M}^{-1}\mathbf{C}(\boldsymbol{\nu})\boldsymbol{\nu} \\ \mathbf{0}_{10\times 1} \end{bmatrix}}_{\mathbf{f_0}(\mathbf{x}_{\text{aug}})} + \underbrace{\begin{bmatrix} \mathbf{0}_{6\times 6} \\ \mathbf{M}^{-1} \\ \mathbf{0}_{10\times 6} \end{bmatrix}}_{\mathbf{F}(\mathbf{x}_{\text{aug}})} \boldsymbol{\tau}, \tag{6.19}$$

where, $\mathbf{f_0}$ is the drift vector field, and the columns of $\mathbf{F}$ are the control vector fields, $\mathbf{f_i}$ for $i = 1, \ldots, 6$, corresponding to the six inputs (entries of $\boldsymbol{\tau}$). Finally, we assume that all the states in the original state vector are measurable, that is,

$$\mathbf{y} = \mathbf{x} := \mathbf{h}(\mathbf{x}_{\text{aug}}). \tag{6.20}$$

Proposition 1 *The system (6.19) with the output function (6.20) is weakly observable if there exists an appropriate, nonzero force input.*

Proof The span of selected Lie derivatives, $\mathcal{G} = \text{span}\{\mathbf{h}, L_{\mathbf{f_0}}\mathbf{h}, L_{\mathbf{f_i}}L_{\mathbf{f_0}}\mathbf{h}\}$ where $i \in \{1, 2, 3\}$ has the same dimension as the (augmented) state vector,

$$\text{rank}\, d\mathcal{G} = 22, \tag{6.21}$$

hence by the rank condition (3.6), all the states (including the augmented ones) are observable with a forcing profile that activates the necessary Lie brackets. ■

Rigid Body Dynamics in 2D

There are four inertial parameters of interest for the rigid body dynamics in the vertical plane: m, c_x, c_z, and I_{yy}, therefore we can define an augmented state vector as:

$$\bar{\mathbf{x}}_{\text{aug}} = \begin{bmatrix} p_x & p_z & \theta & U & W & Q & m & c_x & c_z & I_{yy} \end{bmatrix}^\top \in \mathbb{R}^{10}, \tag{6.22}$$

which allows us to write the dynamics (2.15) in the control-affine form,

$$\dot{\bar{\mathbf{x}}}_{\text{aug}} = \underbrace{\begin{bmatrix} \bar{\boldsymbol{\nu}} \\ -\bar{\mathbf{M}}^{-1}\bar{\mathbf{C}}(\bar{\boldsymbol{\nu}})\bar{\boldsymbol{\nu}} \\ \mathbf{0}_{4\times 1} \end{bmatrix}}_{\bar{\mathbf{f}}_{\mathbf{0}}(\bar{\mathbf{x}}_{\text{aug}})} + \underbrace{\begin{bmatrix} \mathbf{0}_{3\times 3} \\ \bar{\mathbf{M}}^{-1} \\ \mathbf{0}_{4\times 3} \end{bmatrix}}_{\bar{\mathbf{F}}(\bar{\mathbf{x}}_{\text{aug}})} \bar{\boldsymbol{\tau}}, \tag{6.23}$$

where, $\bar{\mathbf{f}}_{\mathbf{0}}$ is the 2D drift vector field, and the columns of $\bar{\mathbf{F}}$ are the control vector fields, $\bar{\mathbf{f}}_{\mathbf{i}}$ for $i = 1, 2, 3$, corresponding to the three inputs (entries of $\bar{\boldsymbol{\tau}}$). Also, we assume that all the states in the original state vector are measurable, that is,

$$\bar{\mathbf{y}} = \bar{\mathbf{x}} := \bar{\mathbf{h}}(\bar{\mathbf{x}}_{\text{aug}}). \tag{6.24}$$

To analyze the observabilitiy, we first build a Lie algebra considering just the drift term:

$$\bar{\mathcal{G}}_{\text{little}} = \text{span}\{\bar{\mathbf{h}}, L_{\bar{\mathbf{f}}_{\mathbf{0}}}\bar{\mathbf{h}}, \ldots, L_{\bar{\mathbf{f}}_{\mathbf{0}}}^{n-1}\bar{\mathbf{h}}\}, \tag{6.25}$$

which is sometimes called the little observability Lie algebra [75]. Note that this Lie algebra does not span the (augmented) state space since

$$\operatorname{rank} d\bar{\mathcal{G}}_{\text{little}} = 8 \tag{6.26}$$

is less than the dimension of the state space, that is, the system (6.23) is not observable if only the drift is active but no control, e.g., when a vertical take-off and landing (VTOL) aircraft is hovering or an airliner is in cruise flight. Additionally, although it is not always possible to determine unobservable states when the Jacobian of a Lie algebra is rank deficient, in this case, we are able to see that m and I_{yy} are the unobservable parameters as they do not appear in

$$\bar{\mathbf{M}}^{-1}\bar{\mathbf{C}}(\bar{\boldsymbol{\nu}})\bar{\boldsymbol{\nu}} = \begin{bmatrix} -Q(W - Qc_x) \\ Q(U + Qc_z) \\ 0 \end{bmatrix}. \tag{6.27}$$

Proposition 2 *The system (6.23) with the output function (6.24) is weakly observable if there exists an appropriate, nonzero force input.*

Proof Define a Lie algebra consisting of selected Lie derivatives as

$$\bar{\mathcal{G}} = \operatorname{span}\{\bar{\mathbf{h}}, L_{\bar{\mathbf{f}}_\mathbf{i}}\bar{\mathbf{h}}, L_{\bar{\mathbf{f}}_\mathbf{i}}L_{\bar{\mathbf{f}}_\mathbf{0}}\bar{\mathbf{h}}\}, \quad i \in \{1, 2\}. \tag{6.28}$$

The Jacobian of $\bar{\mathcal{G}}$ is full rank,

$$\operatorname{rank} d\bar{\mathcal{G}} = 10, \tag{6.29}$$

that is, all the states (including the inertial parameters) are observable in the presence of an appropriate, nonzero force input that activates the necessary Lie brackets. ■

We were also able to see that the observability of one of m and I_{yy} in the presence of a torques input requires the other one to be already observable by repeating the observability analysis without them and with one of them in the augmented state vector.

Finally, we note that the inertial parameters are observable even if the only available outputs are the translational and rotational velocities.

In terms of structure for the forcing profiles in order to generate the necessary Lie brackets, work in [76, 77] for controllability indicates that appropriate forcing functions include classes of cyclic functions. Note that a constant control vector field will yield an identically zero Lie bracket, so constant forcing will not immediately meet the required forcing for observability.

Table 6.1: Inertial Parameters of a Narrow-body Commercial Aircraft [78]

Properties	Values
mass, m	$49.895\,\mathrm{kg}$
I_{xx}	$761.970\,\mathrm{kg\,m^2}$
I_{yy}	$1.997 \times 10^6\,\mathrm{kg\,m^2}$
I_{zz}	$2.568 \times 10^6\,\mathrm{kg\,m^2}$
I_{xz}	$10.847\,\mathrm{kg\,m^2}$
I_{yz}, I_{xy}	$0\,\mathrm{kg\,m^2}$

6.3.2 Numerical Application

In the previous subsection, we saw that a force input is sufficient to have an observable system. In this subsection, we will find an optimal input for the rigid body in 2D using the methodology described in Sec. 6.2 and compare corresponding empirical Gramian-based observability metrics and filter performances with the ones obtained from suboptimal trajectories.

We first set up the system simulations to obtain the empirical observability Gramian. As a reference, the inertial parameters of a narrow-body aircraft are taken from FlightGear, an open-source flight simulator [78], and given in Table 5.1. We represent the rigid body by its inertia ellipsoid, a graphical representation of the principal moments of inertia (I_{xx}, I_{yy} and I_{zz}), and select the center of mass as $\mathbf{c} = \begin{bmatrix} 2 & 0 & 1 \end{bmatrix}^\top$ in meters since we assume (vertical) planar motion and a random point on the xz-plane would have nonzero x- and z-axes components (Fig. 6.1).

In the previous section, we showed that having an appropriate, nonzero F_x or F_z makes the system observable which was unobservable in the drift-only case, hence we assume that the generalized vector of external forces and moments is $\bar{\boldsymbol{\tau}}(t) = \begin{bmatrix} F_x(t) & 0 & 0 \end{bmatrix}^\top$, and test three input profiles (trajectories): a constant input, a single periodic command signal similar to the ones in [24], and an optimized multisine input,

$$\textbf{input A (constant):} \qquad F_x^{\mathbf{A}}(t) = \mathscr{A} \tag{6.30a}$$

$$\textbf{input B (sine):} \qquad F_x^{\mathbf{B}}(t) = \mathscr{A} \sin(2\pi f_{\text{base}} t) \tag{6.30b}$$

$$\textbf{input C (multisine):} \qquad F_x^{\mathbf{C}}(t) = \sum_{n \in \{1,\ldots,M\}} \mathscr{A}_k \sin(2\pi k f_{\text{base}} t), \tag{6.30c}$$

where we select the signal amplitude and frequency as $\mathscr{A} = 1 \times 10^8\,\text{N}$ and $f_{\text{base}} = 0.1\,\text{Hz}$ and obtain $\mathscr{A}_k$'s for $M = 5$ as $\boldsymbol{\mathscr{A}} = \begin{bmatrix} 6.7 & 5.1 & 0.017 & 2.0 & 0.25 \end{bmatrix}^\top \times 10^7\text{N}$ from the formulation (6.15) using a hybrid PSO approach with a logarithmic search space $[10^4, 10^{8.25}]$N and $ub = 1 \times 10^8\,\text{N}$. We assumed zero phase differences to keep the search space dimension smaller. We note that F_x also creates the effect of a torque about the y-axis since the center of mass has a nonzero z-axis component.

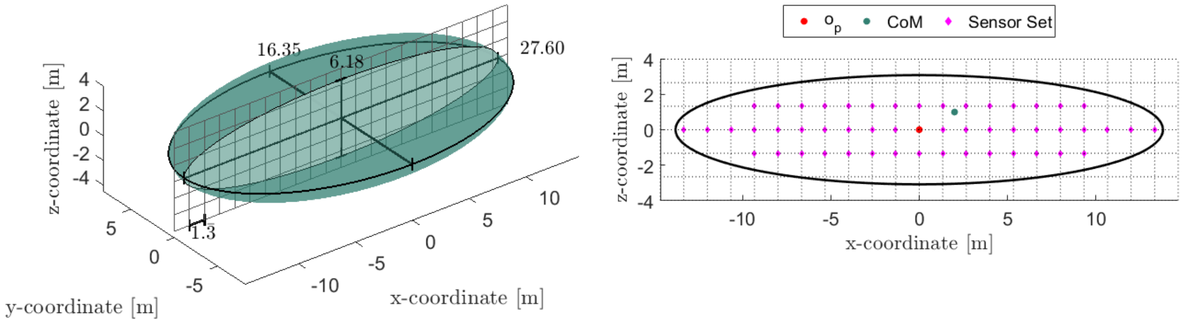

(a) **(b)**

Figure 6.1: (a) Rigid body in 3D represented by its principal moments of inertia. (b) Center of mass (CoM), geometric center, o_p, and 51 sensor locations shown in the cross-section of the inertia ellipsoid. The force is applied at o_p.

The plots of three excitation profiles and their derivatives are given in Fig. 6.2.

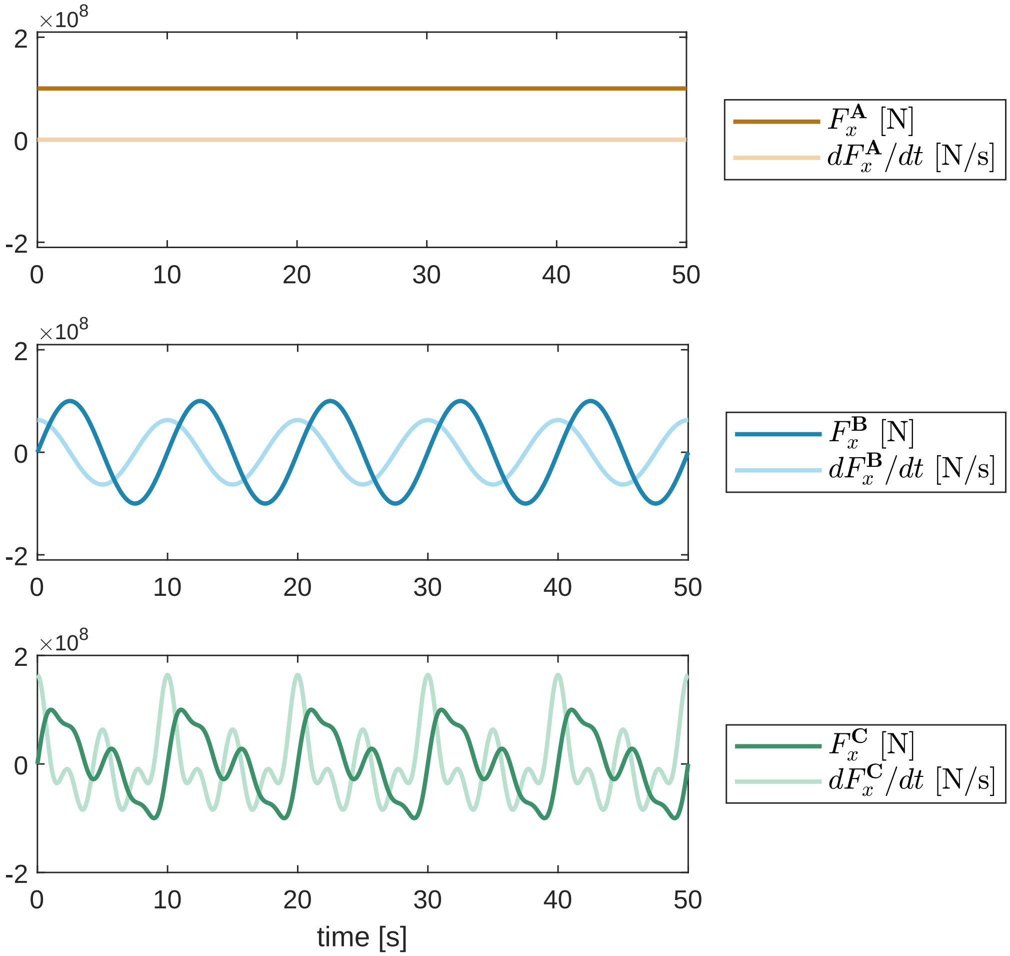

Figure 6.2: Three input (excitation) profiles and their derivatives with respect to time. The multisine signal has the highest derivative in magnitude with the value 1.6×10^8**.**

Although the angular rate, Q, remains the same across the vertical plane, $y = 0$, the translational velocities, U and W, depend on where we measure them. In order to account for variations in observability due to the location of measurement, we consider 51 equally-spaced sensor locations in the inertia ellipsoid for the empirical observability Gramian computations.

We chose the states of interest as m, c_x, c_z, and I_{yy} and the simulation time as $t_1 =$

50 s. Both the perturbation amounts and the outputs need scaling. Following the approach described in Subsec. 6.2.2, the vector of perturbation amounts is chosen as

$$\boldsymbol{\varepsilon} = \begin{bmatrix} 498.95 & 0.01 & 0.01 & 1.997 \times 10^{6} \end{bmatrix}^{\top},$$

and we scale translational velocities by 1/1000 and angular rates by $1/2\pi$, reciprocals of some relatively large values.

Empirical Observability Gramian

The spatially averaged empirical observability Gramian eigenvalues corresponding to the four inertial parameters of the rigid body in 2D and the three input profiles are given in Fig. 6.3. The orders of magnitude of the eigenvalues vary significantly, that is, the condition number of the empirical observability Gramian, $\kappa(W_o^{\boldsymbol{\varepsilon}})$, is undesirably high. In particular, $\kappa(W_o^{\boldsymbol{\varepsilon}})$ takes on its highest value, 2.2×10^{15}, when we applied constant force. These results demonstrate a key feature of the functionality of Lie brackets in observability as noted in Subsec. 6.3.1 where cyclic motions of particular types are needed to generate the vector fields. Compared to the mass and the inertia matrix entry I_{yy}, the center of mass components c_x and c_z are more observable regardless of the excitation profile.

The observability metrics do not vary significantly based on the sensor locations (Fig. 6.4). One of the reasons for this behaviour is that the contribution of the angular rate measurement to the empirical observability Gramian is independent from the sensor location. In non-constant input cases, as the distance between the center of mass and the sensor location increases, the observability metrics achieved higher values, that is, the inertial parameters were more observable at locations far from the CoM. Both observability metrics had their best value when the applied force is the optimal multisine signal, $F_x^{\mathbf{C}}$.

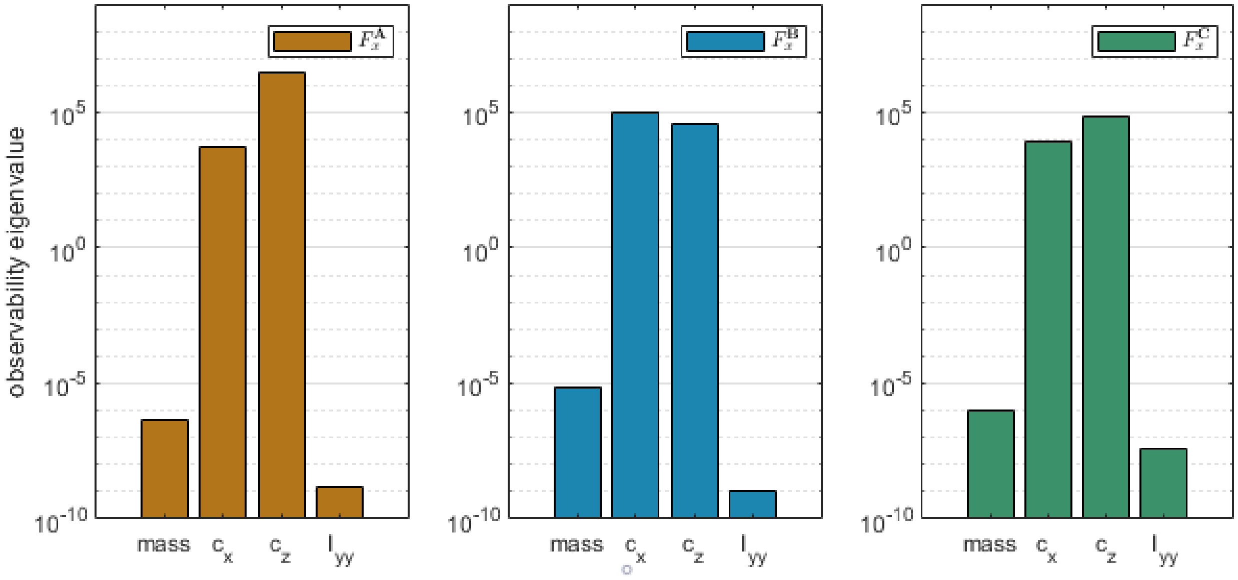

Figure 6.3: Spatially averaged empirical observability Gramian eigenvalues for the four inertial parameters of the rigid body (airliner) in the vertical plane.

Estimation (EKF)

We designed an extended Kalman filter (EKF) to estimate the inertial parameters from the simulation of the system dynamics with augmented states (6.23). We selected the initial estimation values of m, c_x, c_z, and I_{yy} as 59 874 kg, 3 m, 1.5 m, and 2 695 770 kg m^2, respectively. The measurements were taken at o_p, the geometric center of the inertia ellipsoid where F_x was applied.

The estimation of the four inertial parameters for three input profiles throughout the simulation are given in Fig. 6.5. In all the three cases, the estimated values of the center of mass components, c_x and c_z, converge to their true values in less than five seconds. On the other hand, the estimation of the mass and the moment of inertia about the y-axis, I_{yy}, require more time, and the EKF indeed fails to estimate the mass in 50 seconds. when the constant force (input A) is introduced. These results are consistent with the empirical observability Gramian simulations where the eigenvalues corresponding to c_x and c_z were greater than the others and the empirical Gramian matrix was ill-conditioned in the constant-

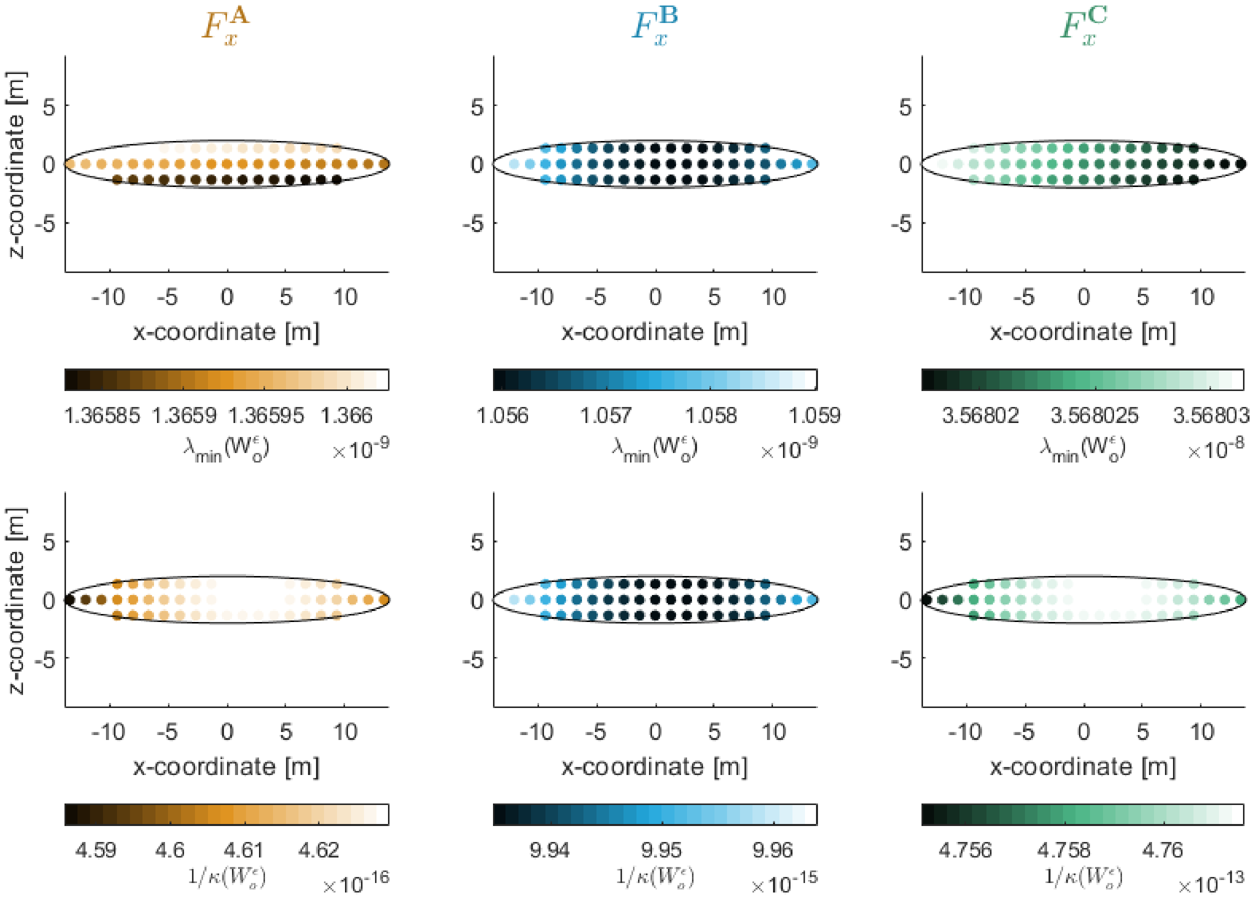

Figure 6.4: The change of the two empirical observability Gramian-based metrics across the cross-section of the inertia ellipsoid and by the forcing function.

force case. As for non-constant-input cases, the estimator with the optimized multisine input performed relatively better than the one with a single periodic command signal.

Varying Parameters

One of the main advantages of using a filter to obtain the inertial parameters is being able to perform the task in real-time. This ability also allows us to deal with varying parameters as the filters have already been studied to estimate time-varying states. In this last part of the application, we will use the parameters of a spacecraft modeled as a rigid body with one difference: the mass of the system, m, and the inertia matrix entry I_{yy} change at rates

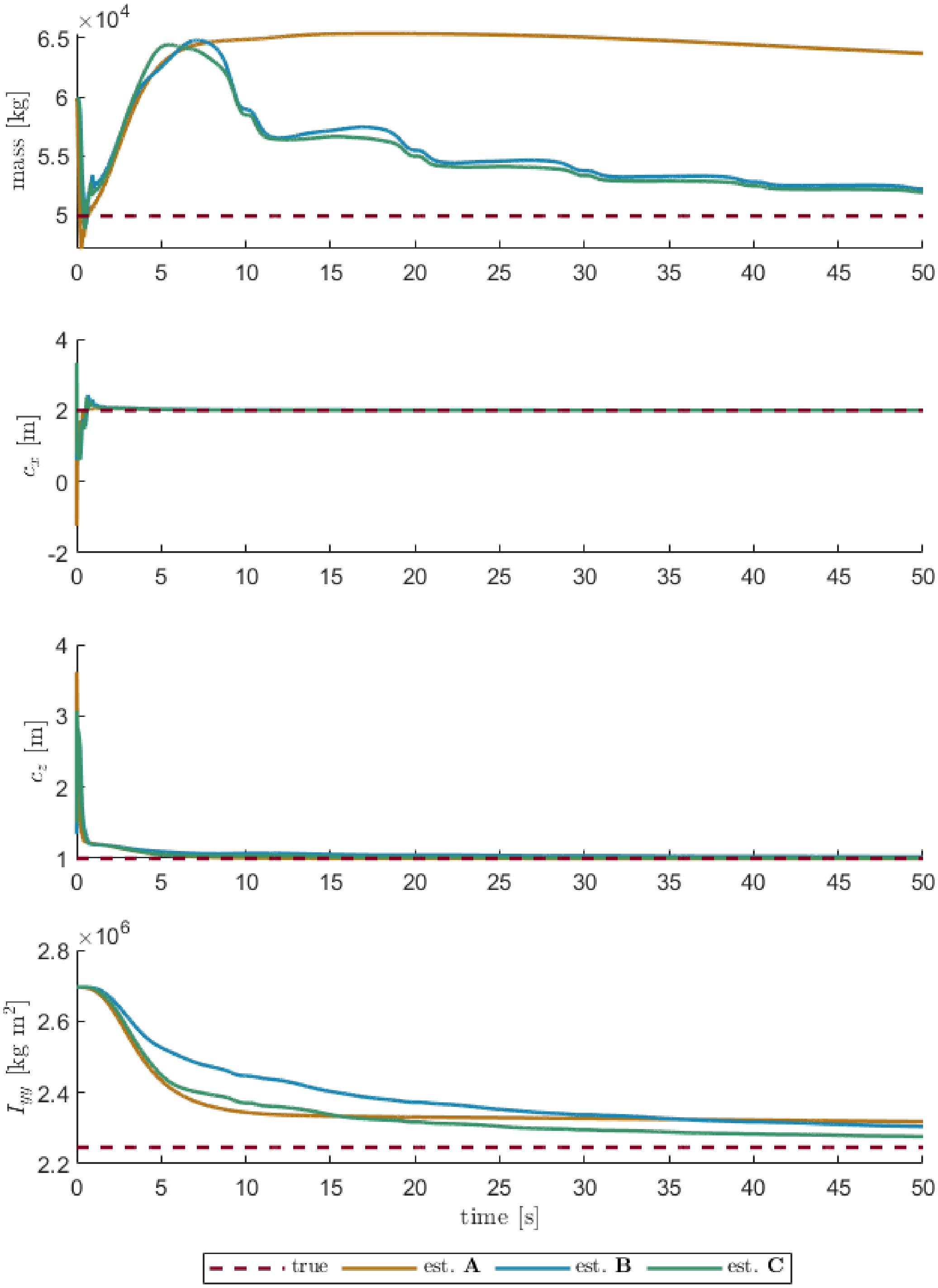

Figure 6.5: Estimation of the four inertial parameters of the rigid body in 2D.

Table 6.2: **Inertial Parameters of the Cassini spacecraft [79]**

Properties	initial mass [kg]	initial I_{yy} [kg m^2]	final mass [kg]	final I_{yy} [kg m^2]
Values	4,522	8,155	848.3	$6,174$

$\dot{m} = dm/dt$ and $\dot{I_{yy}} = dI_{yy}/dt$, respectively, where dm and dI_{yy} are negative numbers.

Since we have already shown that constant input is not desirable for observability and the sensor location does not dramatically affect the (un)observability metrics, here, we perform the observability analysis and estimation at o_p, where the optimized multisine signal is applied. The parameters for this part belong to the Cassini spacecraft [79] and are given in Table 6.2. We assume that the change rate of m and I_{yy} are constant, that is, $dm = -3673/t_1$ and $dI_{yy} = -1981/t_1$ where the total simulation time is $t_1 = 50$ unit time. The center of mass, again, is selected as being off both x- and z-axes: $c_x = 0.5\,\mathrm{m}$ and $c_z = 0.25\,\mathrm{m}$.

We selected the signal frequency as $f_{\text{base}} = 0.05\,\mathrm{Hz}$ in Eq. (6.30c) and obtained $\mathscr{A}_k$'s for $M = 3$ as $\boldsymbol{\mathscr{A}} = \begin{bmatrix}1.1 & 0.0010 & 0.067\end{bmatrix}^\top \times 10^5\mathrm{N}$ from the formulation (6.15) again using a hybrid PSO approach with a logarithmic search space $[10, 10^{5.25}]\mathrm{N}$ and $ub = 1 \times 10^5\,\mathrm{N}$. The plot of the input function and its derivative is given in Fig. 6.6a, and the empirical observability Gramian eigenvalues can be seen in Fig 6.6b. Similar to the results obtained for the airliner parameters, the center of mass components are more observable than the mass and the inertia matrix entry ($\kappa(W_o^\varepsilon) = 1.6 \times 10^9$).

The initial estimation values of the inertial parameters m, c_x, c_z, and I_{yy} for the EKF were selected as 5426 kg, 0.6 m, 0.275 m, and 11 482 kg m^2, respectively. The percentage estimation error for the mass and I_{yy} is given in Figure 6.7. Although the estimator needed more time, $2t_1$ in total, to identify the parameters, we were able to obtain the time-varying values with 5.1% error for the mass and 0.9% error for I_{yy}.

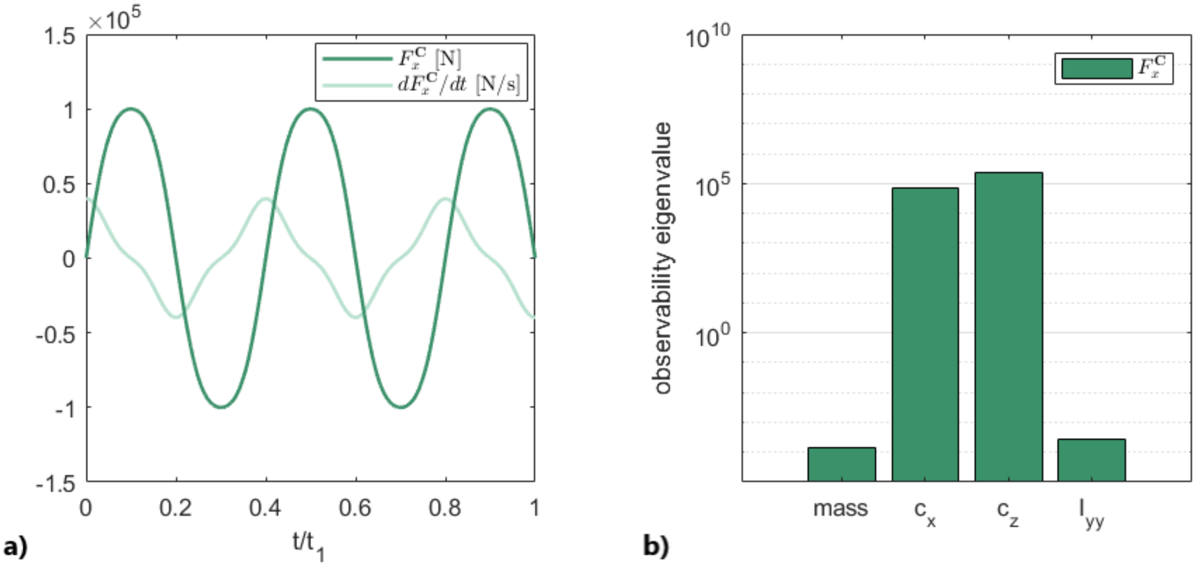

Figure 6.6: a) The optimized multisine signal for the estimation of the Cassini spacecraft inertial parameters. b) Empirical observability Gramian eigenvalues for the four inertial parameters of the rigid body (Cassini) in the vertical plane.

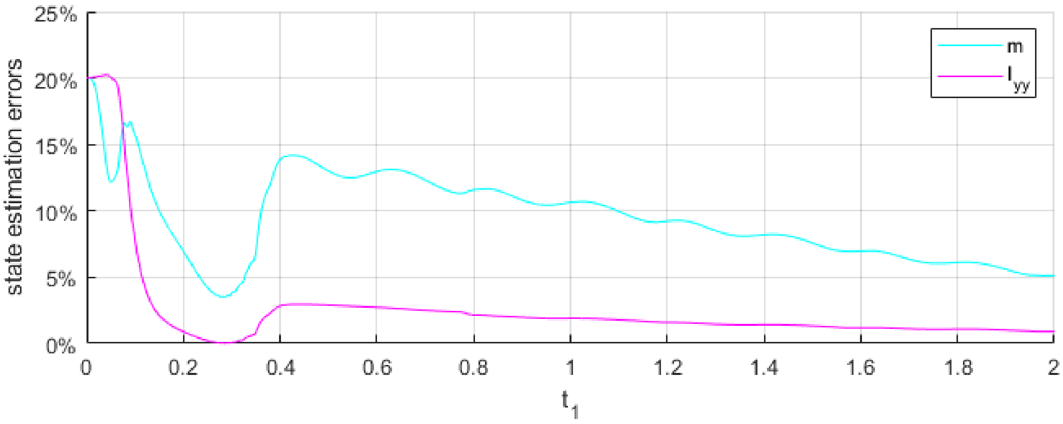

Figure 6.7: The percentage estimation error given for the two time-varying inertial parameters of the rigid body (Cassini) in the vertical plane.

Chapter 7

CONCLUSION

7.1 Summary of Results

In this dissertation, we first presented observability analysis approaches for two kinds of systems: systems with output delay and systems with an output function in the form of function composition. Although we were inspired by the neural encoding mechanism in animal sensing, the results are also useful for existing engineered systems as in the example of the double integrator with a saturated output. We also studied optimal neural-inspired sensor placement and the effect of neural encoding parameters on system observability. We note that there are some combinations of STA and NLA parameters providing higher observability, which might be insightful in both computational neuroscience and engineering applications.

Second, we formulated an optimal sensor placement methodology based on the stochastic empirical observability Gramian and illustrated it for a UAV system and flapping wing dynamics. Since the problems are stochastic and non-convex, we performed Monte Carlo runs and used a metaheuristic optimization algorithm called PSO. When a linear combination of two unobservability metrics was used as the objective function, the algorithm placed at least one sensor on each edge of the flapping wing. We also saw that adding a new sensor does not improve the observability significantly after a certain point.

Trajectory optimization to ensure and improve observability was studied using two concepts in observability analysis: orthogonality of the observability matrix, and the invertibility of the empirical observability Gramian. The estimation of rigid body inertial parameters was dealt with in Chapter 6 using analytical and numerical observability analysis tools. It was shown that the parameters are observable if the net force at the point of measurement is nonzero. The estimation condition number obtained from the computation of the empirical observability Gramian was undesirably higher when the applied net force was constant and the necessary Lie brackets were not immediately generated. This result was supported by the performance of the estimator; one of the inertial parameters (the mass) did not converge to its true value in the given simulation time. The estimator was most successful when the input consisted of multisine waves with a high function derivative value. Finally, we successfully used the same approach for time-varying parameters.

7.2 Future Work

We expect that the observability analysis of systems with output delay and systems with composite output functions will be revisited and extended as needed by researchers based on the application. The brief discussion given in Sec. 4.4 would be a good starting point to relate the empirical observability Gramians of systems with and without composite output functions.

We used the empirical observability Gramian-based methods to improve the performance of estimators based on the fact that the Gramian matrix (at the limit $\varepsilon \to 0$) bounds the Fisher information matrix. How better observability metrics result in better estimation performances is still an intriguing research question. For an accurate analysis, one should also consider the structure of the observer they use, e.g., the neural-encoded data are then similarly decoded by a neural mechanism to extract the stimulus information.

A more realistic wing model has already been studied by our collaborators [80] taking into account the actual wing profiles, nonuniform stiffness of the wing, and the structure of the strain-sensitive biological sensors. Campaniform sensilla-like mechanosensors were also designed by other researchers [81]. Additionally, the neural spikes can be considered as the system output instead of the probability of firing, P_{fire}. In that case, the system would be stochastic even if no process or measurement noise is introduced.

The optimal sensor placement for stochastic systems is, as discussed in Sec. 5.4, a problem with several interesting avenues for future work. The existence of a global optimal solution for a given set of simulation data makes the problem more appealing. One should start with relaxing the integer constraint to deal with the sensor placement task.

The numerical results on the optimal trajectory planning to insure and improve observability are encouraging to study the input design further analytically. Similar to the approaches to the controllability question in the 1990s, first, systems with particular state-space representations can be studied to analytically show how the necessary level of Lie brackets depends on the input profile.

Finally, we used a 3-DoF rigid body model for the numerical simulations. It would be wise to use an unscented Kalman filter (UKF) or a particle filter instead of the EKF if one would like to study the full body dynamics. Since these methods do not require linearization of the system dynamics, their performance would also be better or equal to the performance of the EKF we implemented in this dissertation.

BIBLIOGRAPHY

[1] Nathan D. Powel and Kristi. A. Morgansen. Empirical observability gramian rank condition for weak observability of nonlinear systems with control. In *Proceedings of the 54th Conference on Decision and Control*, pages 6342–6348, Osaka, Japan, 2015. IEEE.

[2] Eugene A. Morelli. Determining aircraft moments of inertia from flight test data. *Journal of Guidance, Control, and Dynamics*, 45(1):4–14, 2022.

[3] Allan Y. Lee and Julie A. Wertz. In-flight estimation of the cassini spacecraft's inertia tensor. *Journal of Spacecraft and Rockets*, 39(1):153–155, 2002.

[4] Peter Dayan and Laurence F. Abbott. *Theoretical Neuroscience: Computational and Mathematical Modeling of Neural Systems.* MIT Press, Cambridge, MA, 2001.

[5] Tim Gollisch and Markus Meister. Eye smarter than scientists believed: Neural computations in circuits of the retina. *Neuron*, 65(2):150–164, 2010.

[6] Jessica L. Fox, Adrienne L. Fairhall, and Thomas L. Daniel. Encoding properties of haltere neurons enable motion feature detection in a biological gyroscope. *Proceedings of the National Academy of Sciences*, 107(8):3840–3845, 2010.

[7] Bradley H. Dickerson, Zane N. Aldworth, and Thomas L. Daniel. Control of moth flight posture is mediated by wing mechanosensory feedback. *Journal of Experimental Biology*, 217(13):2301–2308, 2014.

[8] A. L. Eberle, B. H. Dickerson, P. G. Reinhall, and T. L. Daniel. A new twist on gyroscopic sensing: body rotations lead to torsion in flapping, flexing insect wings. *J. R. Soc. Interface*, 12(104):20141088, 2015.

[9] Brandon Pratt, Tanvi Deora, Thomas Mohren, and Thomas Daniel. Neural evidence supports a dual sensory-motor role for insect wings. *Proceedings of the Royal Society B: Biological Sciences*, 284(1862):20170969, 2017.

[10] Thomas L. Mohren, Thomas L. Daniel, Steven L. Brunton, and Bingni W. Brunton. Neural-inspired sensors enable sparse, efficient classification of spatiotemporal data. *Proceedings of the National Academy of Sciences*, 115(42), 2018.

[11] Brett R. Aiello, Kathryn E. Stanchak, Alison I. Weber, Tanvi Deora, Simon Sponberg, and Bingni W. Brunton. Spatial distribution of campaniform sensilla mechanosensors on wings: form, function, and phylogeny. *Current Opinion in Insect Science*, 48:8–17, 2021.

[12] R. E. Kalman. On the general theory of control systems. *IFAC Proceedings Volumes*, 1(1):491–502, 1960. 1st International IFAC Congress on Automatic and Remote Control, Moscow, USSR, 1960.

[13] Robert Hermann and Arthur J. Krener. Nonlinear controllability and observability. *IEEE Transactions on Automatic Control*, 22(5):728–740, 1977.

[14] Andrzej W. Olbrot. Observability and observers for a class of linear systems with delays. *IEEE Transactions on Automatic Control*, 26(2):513–517, 1981.

[15] Luis A. Aguirre, Leonardo L. Portes, and Christophe Letellier. Observability and synchronization of neuron models. *Chaos: An Interdisciplinary Journal of Nonlinear Science*, 27(10):103103, 2017.

[16] Claudia Califano and Claude H. Moog. Observability of nonlinear time–delay systems and its application to their state realization. *IEEE Control Systems Letters*, 4(4):803–808, 2020.

[17] Claudia Califano and Claude H. Moog. *Nonlinear Time-Delay Systems: A Geometric Approach*. Springer Int. Publishing, 1 edition, 2021.

[18] Bruce C. Moore. Principal component analysis in linear systems: Controllability, observability, and model reduction. *IEEE Transactions on Automatic Control*, 26(1):17–32, 1981.

[19] Sanjay Lall, Jerrold E. Marsden, and Sonja Glavaški. Empirical model reduction of controlled nonlinear systems. *IFAC Proceedings Volumes*, 32(2):2598 – 2603, 1999. 14th IFAC World Congress, Beijing, China, 1999.

[20] Nathan Powel and Kristi A. Morgansen. Empirical observability gramian for stochastic observability of nonlinear systems. `https://arxiv.org/abs/2006.07451`, 2020.

[21] Christian Himpe. emgr—the empirical gramian framework. *Algorithms*, 11(7):91, 2018.

[22] Vasile Dragan and Toader Morozan. Stochastic observability and applications. *IMA Journal of Mathematical Control and Information*, 21(3):323–344, 2004.

[23] John L. Crassidis and John L. Junkins. *Optimal Estimation of Dynamic Systems*. Chapman & Hall/CRC, 2nd edition, 2011.

[24] Jasim Ahmed, Vincent T. Coppola, and Dennis S. Bernstein. Adaptive asymptotic tracking of spacecraft attitude motion with inertia matrix identification. *Journal of Guidance, Control, and Dynamics*, 21(5):684–691, 1998.

[25] Jason A. Keim, A. Behcet Acikmese, and Joel F. Shields. Spacecraft inertia estimation via constrained least squares. In *2006 IEEE Aerospace Conference*, pages 6–pp. IEEE, 2006.

[26] Thai Chau Nguyen-Huynh and Inna Sharf. Adaptive reactionless motion and parameter identification in postcapture of space debris. *Journal of Guidance, Control, and Dynamics*, 36(2):404–414, 2013.

[27] Qingliang Meng, Jianxun Liang, and Ou Ma. Identification of all the inertial parameters of a non-cooperative object in orbit. *Aerospace Science and Technology*, 91:571–582, 2019.

[28] Christopher G. Atkeson, Chae H. An, and John M. Hollerbach. Estimation of inertial parameters of manipulator loads and links. *The International Journal of Robotics Research*, 5(3):101–119, 1986.

[29] Jan Swevers, Walter Verdonck, and Joris De Schutter. Dynamic model identification for industrial robots. *IEEE Control Systems Magazine*, 27(5):58–71, 2007.

[30] Wenxiang Wu, Shiqiang Zhu, Xuanyin Wang, and Huashan Liu. Closed-loop dynamic parameter identification of robot manipulators using modified fourier series. *International Journal of Advanced Robotic Systems*, 9(1):29, 2012.

[31] Wei He, Weiliang Ge, Yunchuan Li, Yan-Jun Liu, Chenguang Yang, and Changyin Sun. Model identification and control design for a humanoid robot. *IEEE Transactions on Systems, Man, and Cybernetics: Systems*, 47(1):45–57, 2016.

[32] Julian Förster. System identification of the crazyflie 2.0 nano quadrocopter. Bachelor's thesis, ETH Zurich, 2015.

[33] Rik Bähnemann, Michael Burri, Enric Galceran, Roland Siegwart, and Juan Nieto. Sampling-based motion planning for active multirotor system identification. In *2017 IEEE International Conference on Robotics and Automation (ICRA)*, pages 3931–3938, 2017.

[34] Valentin Wüest, Vijay Kumar, and Giuseppe Loianno. Online estimation of geometric and inertia parameters for multirotor aerial vehicles. In *2019 International Conference on Robotics and Automation (ICRA)*, pages 1884–1890, 2019.

[35] Michael Burri, Michael Bloesch, Zachary Taylor, Roland Siegwart, and Juan Nieto. A framework for maximum likelihood parameter identification applied on mavs. *Journal of Field Robotics*, 35(1):5–22, 2018.

[36] Christoph Böhm, Martin Scheiber, and Stephan Weiss. Filter-based online system-parameter estimation for multicopter uavs. In *Robotics: Science and Systems*, 2021.

[37] Brian T. Hinson and Kristi A Morgansen. Gyroscopic sensing in the wings of the hawkmoth *Manduca sexta*: the role of sensor location and directional sensitivity. *Bioinspiration & Biomimetics*, 10(5):056013, 2015.

[38] S. A. Combes and T. L. Daniel. Into thin air: contributions of aerodynamic and inertial-elastic forces to wing bending in the hawkmoth *Manduca sexta*. *Journal of Experimental Biology*, 206:2999–3006, 2003.

[39] Kenji Doya, Shin Ishii, Alexandre Pouget, and Rajesh P. N. Rao. *Bayesian Brain: Probabilistic Approaches to Neural Coding*. MIT Press, Cambridge, MA, 1st edition, 2006.

[40] Alison I. Weber and Adrienne L. Fairhall. The role of adaptation in neural coding. *Current Opinion in Neurobiology*, 58:135–140, 2019.

[41] J. L. Fox and T. L. Daniel. A neural basis for gyroscopic force measurement in the halteres of *Holorusia*. *Journal of Comparative Physiology A*, 194:887–897, 2008.

[42] T. L. Mohren, T. L. Daniel, A. L. Eberle, P. G. Reinhall, and J. L. Fox. Coriolis and centrifugal forces drive haltere deformations and influence spike timing. *Journal of the Royal Society Interface*, 16(153):728–740, 2019.

[43] Thor I. Fossen. *Handbook of Marine Craft Hydrodynamics and Motion Control*. John Wiley & Sons, Ltd, 1st edition, 2011.

[44] Eric N. Johnson Brian L. Stevens, Frank L. Lewis. *Aircraft Control and Simulation: Dynamics, Controls Design, and Autonomous Systems*. John Wiley & Sons, Ltd, 3rd edition, 2016.

[45] Chi-Tsong Chen. *Linear System Theory and Design*. Oxford University Press, Inc., NY, 3rd edition, 1998.

[46] Eduardo D. Sontag. *Mathematical Control Theory: Deterministic Finite Dimensional Systems*. Springer-Verlag, NY, 1st edition, 1998.

[47] Sergey K Korovin and Vasily V Fomichev. *State Observers for Linear Systems with Uncertainty*. Walter de Gruyter GmbH Co.KG, 1st edition, 2009.

[48] Milena Anguelova. *Nonlinear Obserservability and Identifiability: General Theory and a Case Study of a Kinetic Model for S. cerevisiae*. PhD thesis, Chalmers University of Technology and Göteborg University, 2004.

[49] Brian T. Hinson, Michael K. Binder, and Kristi A. Morgansen. Path planning to optimize observability in a planar uniform flow field. In *Proceedings of American Control Conference (ACC)*, pages 1392–1399, Washington, DC, 2013.

[50] Aurthur J. Krener and Kayo Ide. Measures of unobservability. In *Proceedings of the 48th Conference on Decision and Control*, pages 6401–6406, Shanghai, 2009. IEEE.

[51] Didier Georges. Towards optimal architectures for hazard monitoring based on sensor networks and crowdsensing. *Journal of Integrated Disaster Risk Management*, 10(1), 2020.

[52] P. C. Müller and H. I. Weber. Analysis and optimization of certain qualities of controllability and observability for linear dynamical systems. *Automatica*, 8(3):237–246, 1972.

[53] Junjian Qi, Kai Sun, and Wei Kang. Optimal pmu placement for power system dynamic state estimation by using empirical observability gramian. *IEEE Transactions on Power Systems*, 30(4):2041–2054, 2015.

[54] Mitch Serpas, Gabriel Hackebeil, Carl Laird, and Juergen Hahn. Sensor location for nonlinear dynamic systems via observability analysis and max-det optimization. *Computers & Chemical Engineering*, 48:105–112, 2013.

[55] Abhay K. Singh and Juergen Hahn. Determining optimal sensor locations for state and parameter estimation for stable nonlinear systems. *Industrial & Engineering Chemistry Research*, 44(15):5645–5659, 2005.

[56] Atiye Alaeddini and Kristi A. Morgansen. Trajectory design for a nonlinear system to insure observability. In *2014 European Control Conference (ECC)*, pages 2520–2525, 2014.

[57] Stephen Boyd, Laurent El Ghaoui, Eric Feron, and Venkataramanan Balakrishnan. *Linear Matrix Inequalities in System and Control Theory.* SIAM, 1994.

[58] Brian T. Hinson and Kristi A. Morgansen. Observability-based optimal sensor placement for flapping airfoil wake estimation. *Journal of Guidance, Control, and Dynamics*, 37(5):1477–1486, 2014.

[59] Michael Grant and Stephen Boyd. CVX: Matlab software for disciplined convex programming, v2.1. `http://cvxr.com/cvx`, 2014.

[60] Michael C. Grant and Stephen P. Boyd. Graph implementations for nonsmooth convex programs. In Vincent D. Blondel, Stephen P. Boyd, and Hidenori Kimura, editors, *Recent Advances in Learning and Control*, Lecture Notes in Control and Information Sciences, pages 95–110. Springer-Verlag Ltd, 2008. `http://stanford.edu/~boyd/graph_dcp.html`.

[61] Steven L. Brunton and J. Nathan Kutz. *Data-driven Science and Engineering: Machine Learning, Dynamical Systems, and Control.* Cambridge University Press, 2019.

[62] James Kennedy and Russell Eberhart. Particle swarm optimization. In *Proceedings of International Conference on Neural Networks*, pages 1942–1948, Perth, WA, Australia, 1995.

[63] Christian Blum and Andrea Roli. Metaheuristics in combinatorial optimization. *ACM Computing Surveys*, 35(3):268–308, 2003.

[64] J. A. Nelder and R. Mead. A simplex method for function minimization. *The Computer Journal*, 7(4):308–313, 1965.

[65] Yuhui Shi and Russell C. Eberhart. Parameter selection in particle swarm optimization. In *Proceedings of 7th International Conference on Evolutionary Programming*, pages 591–600, 1998.

[66] Radha Thangaraj, Millie Pant, Ajith Abraham, and Pascal Bouvry. Particle swarm optimization: Hybridization perspectives and experimental illustrations. *Applied Mathematics and Computation*, 217(12):5208–5226, 2011.

[67] Richard H. Byrd, Mary E. Hribar, and Jorge Nocedal. An interior-point algorithm for large-scale nonlinear programming. *SIAM Journal on Optimization*, 9(4):877–900, 1999.

[68] S. A. Combes and T. L. Daniel. Flexural stiffness in insect wings i. scaling and the influence of wing venation. *Journal of Experimental Biology*, 206(17):2979–2987, 2003.

[69] Mehran Mesbahi and Magnus Egerstedt. *Graph Theoretic Methods in Multiagent Networks*. Princeton University Press, 2010.

[70] Mohamed Hefeeda and Hossein Ahmadi. A probabilistic coverage protocol for wireless sensor networks. In *2007 IEEE International Conference on Network Protocols*, pages 41–50, Beijing, China, 2007.

[71] Qianqian Yang, Shibo He, Junkun Li, Jiming Chen, and Youxian Sun. Energy-efficient probabilistic area coverage in wireless sensor networks. *IEEE Transactions on Vehicular Technology*, 64(1):367–377, 2015.

[72] D. G. Luenberger. Observers for multivariable systems. *IEEE Transactions on Automatic Control*, 11(2):190–197, 1966.

[73] Hassan K. Khalil. *Nonlinear Systems*. Patience Hall, NJ, 3rd edition, 2002.

[74] Ena Hodzic and Kristi A. Morgansen. Simulation-based observability analysis tools for experimental aerospace applications. In *2021 American Control Conference (ACC)*, pages 3010–3017, 2021.

[75] Roger W. Brockett. Nonlinear systems and nonlinear estimation theory. In *Stochastic Systems: The Mathematics of Filtering and Identification and Applications*, pages 441–477. Springer, 1981.

[76] Richard M. Murray and S. Shankara Sastry. Nonholonomic motion planning: Steering using sinusoids. *IEEE Transactions on Automatic Control*, 38(5):700–716, 1993.

[77] Robert T. M'Closkey and Richard M. Murray. Exponential stabilization of driftless nonlinear control systems using homogeneous feedback. *IEEE Transactions on Automatic Control*, 42(5):614–628, 1997.

[78] Flightgear. `https://www.flightgear.org/`, March 2020.

[79] Antonette Feldman and Allan Y. Lee. In-flight estimations of cassini spacecraft inertia tensor and thruster magnitude. In *16th AAS/AIAA Space Flight Mechanics Conference*, Tampa, FL, 2006.

[80] A. H. Mamo, A. I. Weber, T. L. Mohren, M. Babaei, and T. L. Daniel. Finite element analyses of flapping wings meets inertial sensing. In *Integrative and Comparative Biology*, volume 61, pages E564–E565. Oxford University Press Inc., 2021.

[81] Carlo Menon, Rebecca Brodie, Sally Clift, and Julian F. V. Vincent. Concept design of strain sensors inspired by campaniform sensilla. *Acta Astronautica*, 64(2):176–182, 2009.

Appendix A

THIRD AND FOURTH COLUMNS OF $dG_{\mathbf{aux}}$

This appendix includes the elements of dG_{aux} given in Eq. (4.20). $\cos(\sqrt{p}\bar{\tau})$ and $\sin(\sqrt{p}\bar{\tau})$ are denoted by $c\zeta$ and $s\zeta$, respectively.

$$\begin{aligned}
G_{(1,3)} =&K^{-3/2}s\zeta P(\dot{\eta}-R\bar{\tau}q)-K^{-1}[(c\zeta-I_{n_m})R\hat{\mathbf{M}}+P\bar{\tau}c\zeta\dot{\eta}]+K^{-1/2}s\zeta P\bar{\tau}\eta\\
&-K^{-2}(c\zeta-I_{n_m})2PRq\\
G_{(2,3)} =&K^{-1/2}s\zeta(2P\eta+R\hat{\mathbf{M}}+P\bar{\tau}\dot{\eta})+K^{-3/2}s\zeta P(Rq-K\eta)-K^{-1}c\zeta P\bar{\tau}(Rq-K\eta)\\
G_{(3,3)} =&c\zeta(2P\eta+R\hat{\mathbf{M}}+P\bar{\tau}\dot{\eta})+K^{-1/2}s\zeta P[\dot{\eta}+\bar{\tau}(Rq-K\eta)]\\
G_{(4,3)} =&c\zeta P[2\dot{\eta}+\bar{\tau}(Rq-K\eta)]-K^{1/2}s\zeta(2P\eta+R\hat{\mathbf{M}}+P\bar{\tau}\dot{\eta})+K^{-1/2}s\zeta P(Rq-K\eta)\\
G_{(5,3)} =&2c\zeta P(Rq-K\eta)-Kc\zeta(2P\eta+R\hat{\mathbf{M}}+P\bar{\tau}\dot{\eta})-K^{1/2}s\zeta P[3\dot{\eta}+\bar{\tau}(Rq-K\eta)]\\
G_{(1,4)} =&K^{-3/2}s\zeta Q(\dot{\eta}-R\bar{\tau}q)+K^{-1}[(c\zeta-I_{n_m})R\mathbf{M_2}-Q\bar{\tau}c\zeta\dot{\eta}]+K^{-1/2}s\zeta Q\bar{\tau}\eta\\
&-K^{-2}(c\zeta-I_{n_m})2QRq\\
G_{(2,4)} =&K^{-1/2}s\zeta(2Q\eta-R\mathbf{M_2}+Q\bar{\tau}\dot{\eta})+K^{-3/2}s\zeta Q(Rq-K\eta)-K^{-1}c\zeta Q\bar{\tau}(Rq-K\eta)\\
G_{(3,4)} =&c\zeta(2Q\eta-R\mathbf{M_2}+Q\bar{\tau}\dot{\eta})+K^{-1/2}s\zeta Q[\dot{\eta}+\bar{\tau}(Rq-K\eta)]\\
G_{(4,4)} =&c\zeta Q[2\dot{\eta}+\bar{\tau}(Rq-K\eta)]-K^{1/2}s\zeta(2Q\eta-R\mathbf{M_2}+Q\bar{\tau}\dot{\eta})+K^{-1/2}s\zeta Q(Rq-K\eta)\\
G_{(5,4)} =&2c\zeta Q(Rq-K\eta)-Kc\zeta(2Q\eta-R\mathbf{M_2}+Q\bar{\tau}\dot{\eta})-K^{1/2}s\zeta Q[3\dot{\eta}+\bar{\tau}(Rq-K\eta)]
\end{aligned} \tag{A.1}$$

Appendix B

PROOF OF THEOREM 5

We prove by induction. Our base case is $k = 1$. The multiset $M_{1,1} = \{\{1\}\}$ has only one element, which is itself a multiset with a single element that is 1. For $k = 1$, one can thus simplify Eq. (4.28) to obtain

$$L_{\mathbf{f}}(g \circ h) = (g^{(1)} \circ h) L_{\mathbf{f}} h\,. \tag{B.1}$$

Equation (B.1) is equivalent to

$$L_{\mathbf{f}}(g \circ h) = (g' \circ h) L_{\mathbf{f}} h\,, \tag{B.2}$$

which is true and can be straightforwardly derived from the vector identity,

$$\nabla(g \circ h) = (g' \circ h) \nabla h\,. \tag{B.3}$$

For the induction step, we show that if Eq. (4.28) holds for k, it also holds for $k+1$. We have

$$\begin{aligned} L_{\mathbf{f}}^{k+1}(g \circ h) &= \nabla \left\{ \sum_{j=1}^{k} \left[(g^{(j)} \circ h) \sum_{s \in M_{k,j}} \left(\prod_{s_i \in s} L_{\mathbf{f}}^{s_i} h \right) \right] \right\} f \\ &= \sum_{j=1}^{k} \left[\nabla (g^{(j)} \circ h) \sum_{s \in M_{k,j}} \left(\prod_{s_i \in s} L_{\mathbf{f}}^{s_i} h \right) f + (g^{(j)} \circ h) \sum_{s \in M_{k,j}} \nabla \left(\prod_{s_i \in s} L_{\mathbf{f}}^{s_i} h \right) f \right], \end{aligned} \tag{B.4}$$

where we have used the product rule for derivatives. We substitute

$$\nabla(g^{(j)} \circ h) = (g^{(j+1)} \circ h)\nabla h\,, \tag{B.5}$$

in Eq. (B.4). Applying the product rule to the gradient of $\prod L_{\mathbf{f}}^{s_i} h$, we obtain

$$\begin{aligned} L_{\mathbf{f}}^{k+1}(g \circ h) = \sum_{j=1}^{k} \Bigg[&(g^{(j+1)} \circ h)\, \nabla h \sum_{s \in M_{k,j}} \left(\prod_{s_i \in s} L_{\mathbf{f}}^{s_i} h \right) f \\ &+ (g^{(j)} \circ h) \sum_{s \in M_{k,j}} \sum_{s_\ell \in s} \nabla \left(L_{\mathbf{f}}^{s_\ell} h \right) \left(\prod_{\substack{s_i \in s \\ i \neq \ell}} L_{\mathbf{f}}^{s_i} h \right) f \Bigg]\,, \end{aligned} \tag{B.6}$$

The Lie derivatives of h with respect to $\mathbf{x}$ on the vector field $\mathbf{f}$ are scalar-valued, so we reorder Eq. (B.6) to obtain

$$\begin{aligned} L_{\mathbf{f}}^{k+1}(g \circ h) = \sum_{j=1}^{k} \Bigg[&(g^{(j+1)} \circ h) \sum_{s \in M_{k,j}} \left(\prod_{s_i \in s} L_{\mathbf{f}}^{s_i} h \right) L_{\mathbf{f}} h \\ &+ (g^{(j)} \circ h) \sum_{s \in M_{k,j}} \sum_{s_\ell \in s} L_{\mathbf{f}}^{s_\ell + 1} h \left(\prod_{\substack{s_i \in s \\ i \neq \ell}} L_{\mathbf{f}}^{s_i} h \right) \Bigg]\,. \end{aligned} \tag{B.7}$$

We shift the index j in the first part of the right-hand side of Eq. (B.7), so that

$$\begin{aligned} L_{\mathbf{f}}^{k+1}(g \circ h) = &\sum_{j=2}^{k+1} \left[(g^{(j)} \circ h) \sum_{s \in M_{k,j-1}} \left(\prod_{s_i \in s} L_{\mathbf{f}}^{s_i} h \right) L_{\mathbf{f}} h \right] \\ &+ \sum_{j=1}^{k} \left[(g^{(j)} \circ h) \sum_{s \in M_{k,j}} \sum_{s_\ell \in s} L_{\mathbf{f}}^{s_\ell + 1} h \left(\prod_{\substack{s_i \in s \\ i \neq \ell}} L_{\mathbf{f}}^{s_i} h \right) \right]\,. \end{aligned} \tag{B.8}$$

Now let us introduce two multisets A and B with

$$A = \Big\{ \{s_1, s_2, \dots, s_p, 1\} \mid \{s_1, s_2, \dots, s_p\} \in M_{k,j-1} \Big\}$$

and

$$B = \Big\{ \{s_1, s_2, \dots, s_q + 1, \dots, s_p\} \mid q \in \{1, 2, \dots, p\}, \{s_1, s_2, \dots, s_q, \dots, s_p\} \in M_{k,j} \Big\} .$$

Then we can rewrite Eq. (B.8) as

$$\begin{aligned} L_{\mathbf{f}}^{k+1}(g \circ h) =& \sum_{j=1}^{k+1} \left[(g^{(j)} \circ h) \sum_{s \in A \cup B} \left(\prod_{s_i \in s} L_{\mathbf{f}}^{s_i} h \right) \right] \\ & - (g^{(1)} \circ h) \sum_{M_{k,0}} \left(\prod_{s_i \in s} L_{\mathbf{f}}^{s_i} h \right) - (g^{(k+1)} \circ h) \sum_{M_{k,k+1}} \left(\prod_{s_i \in s} L_{\mathbf{f}}^{s_i} h \right) . \end{aligned} \tag{B.9}$$

By definition of $M_{k,j}$ (see Eq. (4.29)), $M_{k,0} = M_{k,k+1} = \emptyset$ and the union $A \cup B$ is equal to $M_{k+1,j}$. We can thus write

$$L_{\mathbf{f}}^{k+1}(g \circ h) = \sum_{j=1}^{k+1} \left[(g^{(j)} \circ h) \sum_{s \in M_{k+1,j}} \left(\prod_{s_i \in s} L_{\mathbf{f}}^{s_i} h \right) \right] ,$$

which completes the proof of Eq. (4.28).

Appendix C

CONJECTURE ON THE GRADIENT OF HIGHER-ORDER LIE DERIVATIVES OF A COMPOSITE FUNCTION

Conjecture 1 *The gradient of the k-th Lie derivative of the composite function $g \circ h$ with respect to the vector $\mathbf{x}$ on the vector field $\mathbf{f}$ is*

$$\nabla L_{\mathbf{f}}^{k}(g \circ h) = \sum_{i=0}^{k} \binom{k}{i} L_{\mathbf{f}}^{k-i}(g' \circ h) \nabla L_{\mathbf{f}}^{i} h, \tag{C.1}$$

where $h : \mathbb{R}^n \to \mathbb{R}$ and $g : \mathbb{R} \to \mathbb{R}$.

For $1 \leq k \leq 3$, the conjecture can be verified directly. An induction step is necessary for the validity for any positive integer k. Notice that, if it is proven, Conj. 1 can also be used to prove Theorem 4.32.

VITA

Burak has pursued his doctorate at the University of Washington (UW), where he served as a teaching assistant, a research assistant and a predoctoral instructor, as a scholar of the Scientific and Technological Research Council of Turkey (TÜBİTAK). He earned a B.S. in aeronautical engineering with a minor in mechatronics and an M.S. in system dynamics and control from Istanbul Technical University (İTÜ), where he was a teaching and research assistant between 2014 and 2017. His research interests include optimal sensor placement and trajectory planning and measurement function forms for highly sensed systems with applications in biological flight and engineered flight and space systems. His hobbies include cinema and archery.